Detection of faint broad emission lines in type 2 AGN – I. Near-infrared observations and spectral fitting

F. Onori,[1,2,3]★ F. La Franca,[3] F. Ricci,[3] M. Brusa,[4,5] E. Sani,[6] R. Maiolino,[7] S. Bianchi,[3] A. Bongiorno,[8] F. Fiore,[8] A. Marconi[9,10] and C. Vignali[4,5]

[1] *SRON Netherlands Institute for Space Research, Sorbonnelaan 2, NL-3584 CA Utrecht, Netherlands*
[2] *Department of Astrophysics/IMAPP, Radboud University, PO Box 9010, NL-6500 GL Nijmegen, the Netherlands*
[3] *Dipartimento di Matematica e Fisica, Università Roma Tre, via della Vasca Navale 84, I-00146 Roma, Italy*
[4] *Dipartimento di Fisica e Astronomia, Università di Bologna, viale Berti Pichat 6/2, I-40127 Bologna, Italy*
[5] *INAF - Osservatorio Astronomico di Bologna, via Ranzani 1, I-40127 Bologna, Italy*
[6] *European Southern Observatory, Alonso de Cordova 3107, Casilla 19, Santiago 19001, Chile*
[7] *Cavendish Laboratory, University of Cambridge, 19 J. J. Thomson Ave, Cambridge CB3 0HE, UK*
[8] *INAF - Osservatorio Astronomico di Roma, via Frascati 33, I-00044 Monte Porzio Catone, Italy*
[9] *Dipartimento di Fisica e Astronomia, Università degli Studi di Firenze, Via G. Sansone 1, I-50019 Sesto Fiorentino, Italy*
[10] *INAF - Osservatorio Astronomico di Arcetri, Largo E. Fermi 5, I-50125 Firenze, Italy*

ABSTRACT

We present medium resolution near-infrared spectroscopic observations of 41 obscured and intermediate class active galactic nuclei (AGN; type 2, 1.9 and 1.8; AGN2) with redshift $z \lesssim 0.1$, selected from the *Swift*/Burst Alert Telescope 70-month catalogue. The observations have been carried out in the framework of a systematic study of the AGN2 near-infrared spectral properties and have been executed using Infrared Spectrometer And Array Camera/VLT, X-shooter/VLT and LUCI/LBT, reaching an average S/N ratio of ∼30 per resolution element. For those objects observed with X-shooter, we also obtained simultaneous optical and UV spectroscopy. We have identified a component from the broad line region in 13 out of 41 AGN2, with full width at half-maximum (FWHM) > 800 km s^{-1}. We have verified that the detection of the broad line region components does not significantly depend on selection effects due to the quality of the spectra, the X-ray or near-infrared fluxes, the orientation angle of the host galaxy or the hydrogen column density measured in the X-ray band. The average broad line region components found in AGN2 has a significantly (a factor 2) smaller FWHM if compared with a control sample of type 1 AGN.

Key words: galaxies: active – quasars: emission lines – galaxies: Seyfert – infrared: galaxies.

1 INTRODUCTION

According to the original ('zeroth order') standard unified model (Antonucci 1993), the main different observational classes of active galactic nuclei (AGN; AGN1 and AGN2) are believed to be the same kind of objects observed under different viewpoints (i.e. different orientations to the observer of an absorbing optically thick, probably clumpy, dusty torus). In particular, the broad lines (>1000 km s^{-1}) observed in AGN1 are thought to be produced in the broad line region (BLR), a dense gas region near the central source (within a few thousands gravitational radii) and thus under the gravitational influence of the central supermassive black hole (BH). On parsec scales, the entire system is enshrouded in a dusty torus that is opaque

to most of the electromagnetic radiation. The torus plays a key role in the framework of the unified model, since it enables the direct observation of the central region (including the BLR) only along particular directions. Narrow lines are generated in distant (on torus scale), rarefied gas regions, where the gravitational influence from the BH is less intense, the Narrow Line Region (NLR). Therefore, an AGN2 is observed in the torus plane (i.e. edge-on) and then the view of the innermost regions of the BLR is obstructed by the intercepting material of the torus. Only narrow emission lines are directly visible in this case. AGN1, instead, are believed to be observed with the torus nearly face-on and then they show in their rest-frame optical spectra both the BLR and the NLR emission lines.

The 'zeroth order' AGN unified model implies that AGN with the same intrinsic (i.e. corrected for absorption) luminosity have the same properties (e.g. same BH masses, same accretion rates). Nevertheless, nowadays there is growing evidence that AGN1 and AGN2

★ E-mail: f.onori@sron.nl.

Table 1. General properties of the observed sample.

Object name (1)	RA (2)	Dec. (3)	Redshift (4)	$\log L_X$ (5)	$\log N_H$ (6)	Cl (7)	Instrument (8)
2MASX J06411806+3249313	06:41:18.0	+32:49:32	0.0470	44.26	23.09 (P12)	2	LUCI
2MASX J09112999+4528060	09:11:30.0	+45:28:06	0.0268	43.42	23.42 (T08)	2	LUCI
2MASX J11271632+1909198	11:27:16.3	+19:09:20	0.1059	44.65	21.79	1.8	LUCI
3C 403	19:52:15.8	+02:30:24	0.059	44.46	23.60 (T08)	2	LUCI
Mrk 417	10:49:30.9	+22:57:52	0.0327	43.90	23.60 (T08)	2	LUCI
NGC 3079	10:01:57.8	+55:40:47	0.00372	42.00	24.73 (A12)	2	LUCI
NGC 4138	12:09:29.8	+43:41:07	0.0029	41.76	22.90 (T08)	1.9	LUCI
NGC 4388	12:25:46.7	+12:39:44	0.0084	43.64	23.63 (T08)	2	LUCI
NGC 4395	12:25:48.8	+33:32:49	0.0013	40.79	22.30 (T08)	1.9^a	LUCI
NGC 4686	12:46:39.9	+54:32:03	0.0167	43.24	21.37 (V13)	$XBONG^b$	LUCI
2MASX J05054575−2351139	05:05:46.5	−23:51:22	0.0350	44.24	23.50 (E09)	2	ISAAC
3C 105	04:07:16.4	+03:42:26	0.089	44.74	23.43 (T08)	2	ISAAC
CGCG 420−015	04:53:25.7	+04:03:42	0.0294	43.75	24.16 (A12)	2	ISAAC
ESO 005−G004	06:05:44.0	−86:37:57	0.0062	42.46	23.88 (T08)	2	ISAAC
ESO 157−G023	04:22:24.2	−56:13:33	0.0435	43.97	22.80	2	ISAAC
ESO 297−G018	01:38:39.3	−40:00:40	0.0252	44.00	23.84 (T08)	2	ISAAC
ESO 374−G044	10:13:20.4	−35:59:07	0.0284	43.57	23.71	2	ISAAC
ESO 416−G002	02:35:14.1	−29:36:26	0.0592	44.29	<19.60 (T08)	1.9	ISAAC
ESO 417−G006	02:56:21.6	−32:11:26	0.0163	43.26	22.70-22.85 (HG15)	2	ISAAC
Fairall 272	08:23:01.1	−04:56:05	0.0218	43.70	23.50 (B11)	2	ISAAC
LEDA 093974	10:40:22.3	−46:25:26	0.0239	43.35	22.96 (T08)	2	ISAAC
MCG−01−24−012	09:20:46.2	−08:03:22	0.0196	43.55	22.80 (T08)	2	ISAAC
MCG−05−23−016	09:47:40.3	−30:57:10	0.0085	43.51	22.47 (T08)	2	ISAAC
Mrk 1210	08:04:06.2	+05:06:31	0.0135	43.35	23.34 (M12)	2	ISAAC
NGC 612	01:33:59.3	−36:29:41	0.0298	44.05	23.70 (T08)	2	ISAAC
NGC 788	02:01:06.4	−06:48:57	0.0136	43.52	23.48 (T08)	2	ISAAC
NGC 1052	02:41:04.8	−08:15:21	0.005	42.22	23.30 (G00)	2	ISAAC
NGC 1142	02:55:12.3	−00:11:02	0.0289	44.23	23.38 (T08)	2	ISAAC
NGC 1365	03:33:38.0	−36:08:31	0.0055	42.63	23.60 (T08)	1.8	ISAAC
NGC 2992	09:45:42.1	−14:19:35	0.0077	42.55	22.00 (T08)	2	ISAAC
NGC 3081	09:59:29.1	−22:49:23	0.0080	43.07	23.52 (T08)	2	ISAAC
NGC 3281	10:31:52.1	−34:51:13	0.0107	43.34	24.30 (T08)	2	ISAAC
PKS 0326−288	03:28:36.8	−28:41:57	0.108	44.60	20.49 (I12)	1.9	ISAAC
ESO 263−G013	10:09:48.2	−42:48:40	0.0333	43.96	23.43 (M13)	2	X-shooter
LEDA 093974	10:40:22.3	−46:25:26	0.0239	43.35	22.96 (T08)	2	X-shooter
MCG−05−23−016	09:47:40.3	−30:57:10	0.0085	43.51	22.47 (T08)	2	X-shooter
2MASX J18305065+0928414	18:30:50.6	+09:28:41	0.0190	42.40	23.26	2	X-shooter
ESO 234−G050	20:35:57.8	−50:11:32	0.0088	42.29	23.95	2	X-shooter
NGC 4941	13:04:13.1	−05:33:06	0.0037	41.79	21.38 (V13)	2	X-shooter
NGC 4945	13:05:27.3	−49:28:04	0.0019	42.35	24.60 (T08)	2	X-shooter
NGC 5643	14:32:40.8	−44:10:29	0.0040	41.80	23.85 (G04)	2	X-shooter
NGC 6221	16:52:46.3	−59:13:01	0.0050	42.05	22.00 (B06)	2	X-shooter
NGC 7314	22:35:46.2	−26:03:01	0.0048	42.42	21.79 (T08)	1.9	X-shooter
NGC 3783	11:39:01.7	−37:44:18	0.0097	43.58	22.47 (T08)	1	X-shooter

Notes. (1) Source name; (2) and (3) RA and Dec. (J2000); (4) Redshift (Baumgartner et al. 2013); (5) 14–195 keV luminosity (erg s^{-1}); (6) Intrinsic hydrogen column density (cm^{-2}; A12 = Ajello et al. 2012; B06 = Beckmann et al. 2006; B11 = Burlon et al. 2011; E09 = Eguchi et al. 2009; G00 = Guainazzi et al. 2000; G04 = Guainazzi et al. 2004; HG15 = Hernández-García et al. 2015; I12 = Ichikawa et al. 2012; M12 = Marinucci et al. 2012; M13 = Molina et al. 2013; P12 = Parisi et al. 2012 T08 = Tueller et al. 2008; V13 = Vasudevan et al. 2013b); (7) SWIFT/BAT AGN classification; (8) Instrument used.
^{a}Sy1.8 from Véron-Cetty & Véron (2006).
^{b}X-Ray Bright Optically Normal Galaxy.

are intrinsically different populations (see e.g. Elitzur 2012), having, on average, different luminosities (smaller for AGN2; Lawrence & Elvis 1982; Ueda et al. 2003; La Franca et al. 2005; Ueda et al. 2014), different accretion rates (smaller for AGN2; Winter et al. 2010), different Eddington ratios (Lusso et al. 2012), different clustering, environment and halo mass properties (Allevato et al. 2014; Jiang et al. 2016; DiPompeo, Hickox & Myers 2016).

One of the fundamental quantity describing an AGN is its BH mass, as it is of paramount importance in order to investigate all

AGN-related science, such as the evolution and phenomenology of AGN, the accretion physics and also the relations and interplay between supermassive BHs and their host galaxies through feedback processes.

In the last decade, using virial based techniques in the optical band (Blandford & McKee 1982; Peterson 1993), it has been possible to measure the BH mass on large AGN1 samples and therefore derive the supermassive BH mass function (Greene & Ho 2007; Kelly, Vestergaard & Fan 2009; Kelly et al. 2010; Merloni et al.
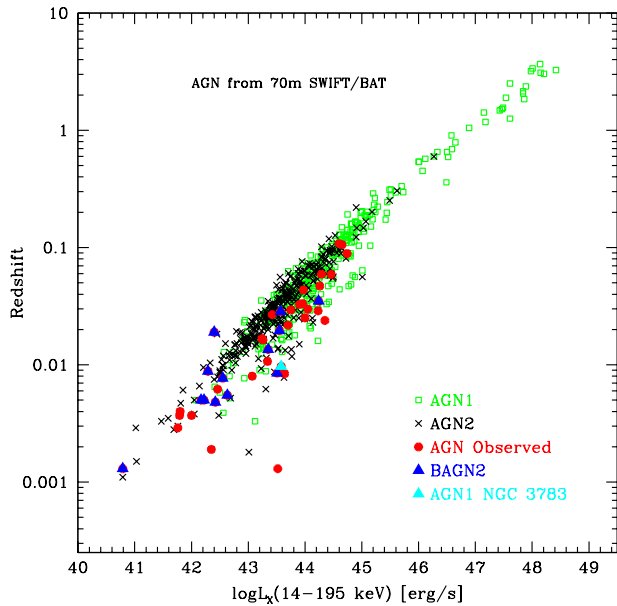
Figure 1. Hubble diagram of the *Swift*/BAT 70-month sample: AGN1 (green open squares), AGN2 (black crosses), AGN2 observed in the framework of our campaign (red filled dots) and those observed 'Broad AGN2', showing BLR components (BAGN2; blue filled triangles). The AGN1 NGC 3783, which has also been observed, is shown by a cyan filled triangle.
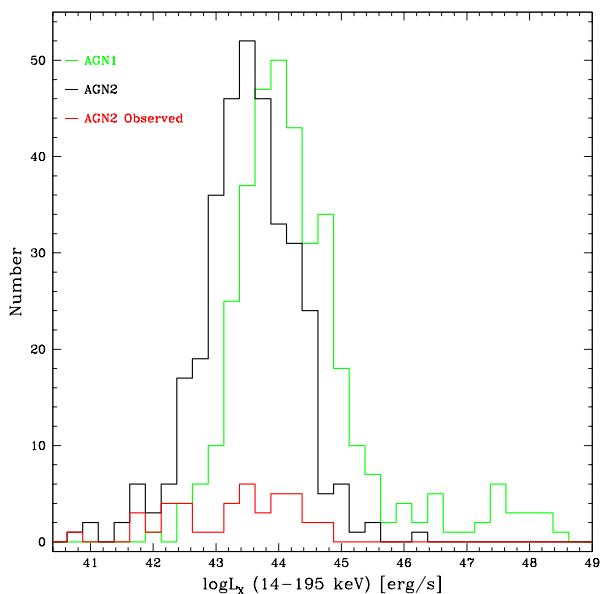

Figure 2. Histogram of the 14–195 keV luminosity of the *Swift*/BAT AGN1 (green line), *Swift*/BAT AGN2 (black line) and our subsample of NIR spectroscopically observed AGN2 (red line).

2010; Bongiorno et al. 2014; Schulze et al. 2015). Many of these measurements are based on the Single Epoch (SE) BH mass virial estimates. By combining the velocity of the BLR clouds (assuming Keplerian orbits) along with their distance R (which is proportional to the square root of the luminosity), it is possible to determine the total mass contained within the BLR (which is dominated by the BH mass; e.g. McLure & Dunlop 2001; Vestergaard 2002; Ho & Kim 2015). However these measurements cannot be applied to AGN2 as the broad line component is not visible in the optical spectra. In those few studies where AGN2 BH masses have been derived (e.g.

Heckman et al. 2004, from SDSS), the authors used the BH–bulge scale relations which, however, were not verified to be valid also for AGN2 (see Graham 2008; Kormendy, Bender & Cornell 2011).

Since their discovery, there have been many attempts, using several methods (e.g. polarimetric and/or high S/N spectroscopy, both in the optical and near-infrared – NIR – bands) to find evidence of the presence of the BLR also in AGN2. Several studies have shown that some AGN2 exhibit faint components of broad lines if observed with high S/N in the NIR, where the dust absorption is less severe than in the optical (Veilleux, Goodrich & Hill 1997; Riffel, Rodríguez-Ardila & Pastoriza 2006; Cai et al. 2010). These studies have found evidence of faint BLR components only in few cases. However these works have not been carried out systematically on statistically well-defined samples.

This is the first in a series of papers dedicated to the study of the AGN2 population using NIR and optical spectra, together with multiwavelength photometric observations, of a subsample of AGN2 extracted from the *Swift*/Burst Alert Telescope (BAT) 70-month AGN X-ray catalogue (Baumgartner et al. 2013). In this paper, we describe the NIR observations and, through a detailed spectral analysis we investigate the presence of BLR components in the near-infrared and (if data are available) optical bands. In the framework of this analysis, as nowadays used in many statistical studies on X-ray selected AGN samples, AGN2 refers to those X-ray selected AGN where no evident BLR emission component (or even no line at all, as in the case of the X-ray Bright Optically Normal Galaxies: XBONG) was identified in their optical spectra (see e.g. Comastri et al. 2002; Civano et al. 2007).

The method and the results for NGC 4395, NCG 6221 and MCG−01−24−012 have already been partially presented in La Franca et al. (2015, 2016). In Sections 2 and 3 the sample and the observations are described, while in Section 4 the line fitting method and the results are shown. Section 5 is dedicated to a study of possible selection effects and in Section 6 the conclusions are presented. We adopt a $\Omega_m = 0.3$, $\Omega_\Lambda = 0.7$ and $H_0 = 70 \, \mathrm{km \, s^{-1} Mpc^{-1}}$ cosmology.

2 THE SAMPLE

The *Swift* Gamma-ray burst observatory was launched in 2004 November, and has been continually observing the hard X-ray sky in the 14–195 keV band with the BAT, a large coded-mask telescope optimized to detect transient Gamma-ray bursts. The wide field of view, the broad sky coverage and the improved sensitivity with respect to the previous *Swift*/BAT surveys, allowed the construction of the 70-month catalogue, one of the most uniform and complete hard X-ray surveys, almost unbiased against Compton-thin ($N_H \sim 10^{22}$–$10^{24} \, \mathrm{cm^{-2}}$) X-ray absorbed AGN (Baumgartner et al. 2013). The 70-month catalogue contains 1210 hard X-ray sources in the 14–195 keV band down to a significance level of 4.8σ and among these 711 are classified as AGN.

In order to look for the faint BLR components in the NIR, we selected a sample of 41 obscured and intermediate class AGN (type 2, 1.9 and 1.8 as classified in Baumgartner et al. (2013); in the following AGN2) with redshift ≲0.1 from the 312 AGN2 of the *Swift*/BAT 70-month catalogue. The first 33 objects were observed with LUCI/LBT (10) and Infrared Spectrometer And Array Camera (ISAAC)/VLT (23) and were randomly extracted from the parent sample according to the observability conditions at the telescopes, while 10 objects were observed with X-shooter/VLT and chosen in order to better cover the X-ray luminosity range of the sample ($40.79 < \log L_{14-195} < 44.60 \, \mathrm{erg \, s^{-1}}$). Two sources (LEDA 093974

Table 2. Journal of observations.

Object name	Obs. date	UT (hh:mm)	Exposure (s)	Seeing (arcsec)	Airmass	Extraction (arcsec)	Scale (pc)
(1)	(2)	(3)	(4)	(5)	(6)	(7)	(8)
LUCI observations							
1 arcsec × 2.8 arcmin slit width; Filter: *zJ*spec; Grating: 200 *H+K*							
2MASX J06411806+3249313	20 Oct 2012	08:15	8 × 350	1.47	1.52	1.5	1402
2MASX J09112999+4528060	20 Oct 2012	10:57	8 × 350	0.75	1.39	1.5	801
2MASX J11271632+1909198	06 Dec 2012	11:06	8 × 350	0.53	1.10	1.5	3146
3C 403	25 Oct 2012	02:14	2 × 350	1.33	1.21	1.5	1778
NGC 3079	24 Oct 2012	12:24	8 × 350	1.08	1.26	1.5	117
NGC 4138	06 Dec 2012	10:55	8 × 350	0.54	1.37	1.5	93
NGC 4388	19 Feb 2013	09:36	8 × 350	0.74	1.07	0.5	82
NGC 4395	05 Dec 2012	12:09	8 × 350	0.54	1.21	1.5	33
NGC 4686	07 Dec 2012	11:16	8 × 350	1.05	1.42	1.5	509
Mrk 417	05 Dec 2012	10:03	8 × 350	0.73	1.38	1.5	972
ISAAC observations							
0.8 arcsec × 120 arcsec slit width; Filter: *J*; Grating: LR and MR							
2MASX J05054575−2351139	03 Nov 2011	03:41	6 × 180	0.90	1.41	0.6	413
3C 105	21 Oct 2011	07:22	6 × 180	0.76	1.15	0.9	1593
CGCG 420−015	19 Dec 2011	06:04	6 × 180	0.71	1.45	0.6	349
ESO 005−G004	04 Nov 2011	03:04	6 × 180	1.36	2.30	0.9	100
ESO 157−G023	19 Oct 2011	07:41	6 × 180	1.03	1.17	0.9	159
ESO 297−G018	13 Oct 2011	04:34	6 × 180	1.22	1.04	0.6	62
ESO 374−G044	22 Jan 2012	01:59	6 × 180	0.98	1.82	0.9	102
ESO 416−G002	08 Oct 2011	02:37	6 × 180	1.05	1.48	0.6	703
ESO 417−G006	11 Oct 2011	06:37	6 × 180	1.00	1.01	0.9	286
Fairall 272	22 Dec 2011	04:49	6 × 180	0.96	1.26	0.6	253
LEDA 093974	08 Jan 2012	04:51	6 × 180	0.85	1.38	0.6	277
MCG−01−24−012	07 Jan 2012	03:06	6 × 180	1.19	1.67	0.9	341
MCG−05−23−016	01 Jan 2012	04:39	6 × 180	0.82	1.29	0.6	92
Mrk 1210	19 Dec 2011	07:56	6 × 180	0.69	1.24	0.6	156
NGC 612	13 Oct 2011	02:43	6 × 180	1.12	1.15	0.9	353
NGC 788	07 Oct 2011	02:09	6 × 180	1.06	1.69	0.9	245
NGC 1052	04 Nov 2011	01:14	6 × 180	0.90	1.54	0.9	90
NGC 1142	09 Oct 2011	04:53	6 × 180	0.90	1.20	0.9	517
NGC 1365	13 Oct 2011	05:56	6 × 180	0.87	1.03	0.6	60
NGC 2992	07 Jan 2012	04:32	6 × 180	1.14	1.28	0.9	127
NGC 3081	06 Jan 2012	03:55	6 × 180	1.16	1.59	0.4	58
NGC 3281	14 Nov 2011	07:26	6 × 180	1.09	1.64	0.9	178
PKS 0326−288	07 Oct 2011	03:01	6 × 180	0.88	1.55	0.9	1943

Object name	Obs. date	UT (hh:mm)	Exposure			Seeing (arcsec)	Airmass	Extraction (arcsec)	Scale (pc)
			UVB (s)	VIS (s)	NIR (s)				
(1)	(2)	(3)		(4)		(5)	(6)	(7)	(8)
X-shooter observations									
slit width: 1.0 arcsec × 11 arcsec for UVB and a 0.9 arcsec × 11 arcsec for VIS and NIR									
ESO 263−G013	11 Feb 2013	00:47	2 × 50	2 × 50	2 × 150	1.2	1.93	1.5	980
LEDA 093974	11 Feb 2013	08:03	2 × 225	2 × 250	2 × 300	0.92	1.28	1.5	693
MCG−05−23−016	11 Feb 2013	01:10	2 × 130	2 × 163	2 × 200	0.85	1.56	1.5	231
2MASX J18305065+0928414	05 Jun 2014	04:15	10 × 225	10 × 259	10 × 291	0.70	1.42	1.0	397
ESO 234−G050	25 Jun 2014	06:38	10 × 225	10 × 259	10 × 291	0.78	1.11	1.0	172
NGC 3783	11 Feb 2013	08:21	2 × 230	2 × 263	2 × 300	0.94	1.09	1.5	181
NGC 4941	21 Jul 2014	22:54	10 × 225	10 × 259	10 × 291	0.84	1.29	1.0	68
NGC 4945	23 Apr 2014	04:47	10 × 225	10 × 259	10 × 291	1.07	1.14	1.0	26
NGC 5643	20 Jun 2014	03:50	10 × 225	10 × 259	10 × 291	1.14	1.24	1.0	71
NGC 6221	24 Apr 2014	06:07	10 × 225	10 × 259	10 × 291	1.01	1.25	1.0	92
NGC 7314	25 Jun 2014	07:50	10 × 225	10 × 259	10 × 291	0.67	1.01	1.0	98

Notes. (1) Source name; (2) Date of observation; (3) Starting UT of acquisition; (4) Number of acquisitions and exposure time for each acquisition; (5) Seeing; (6) Airmass; (7) Width of the 1d spectra extraction; (8) Size of the nuclear region corresponding to the extraction width. The slit width, filter and grating of the instruments are also listed.
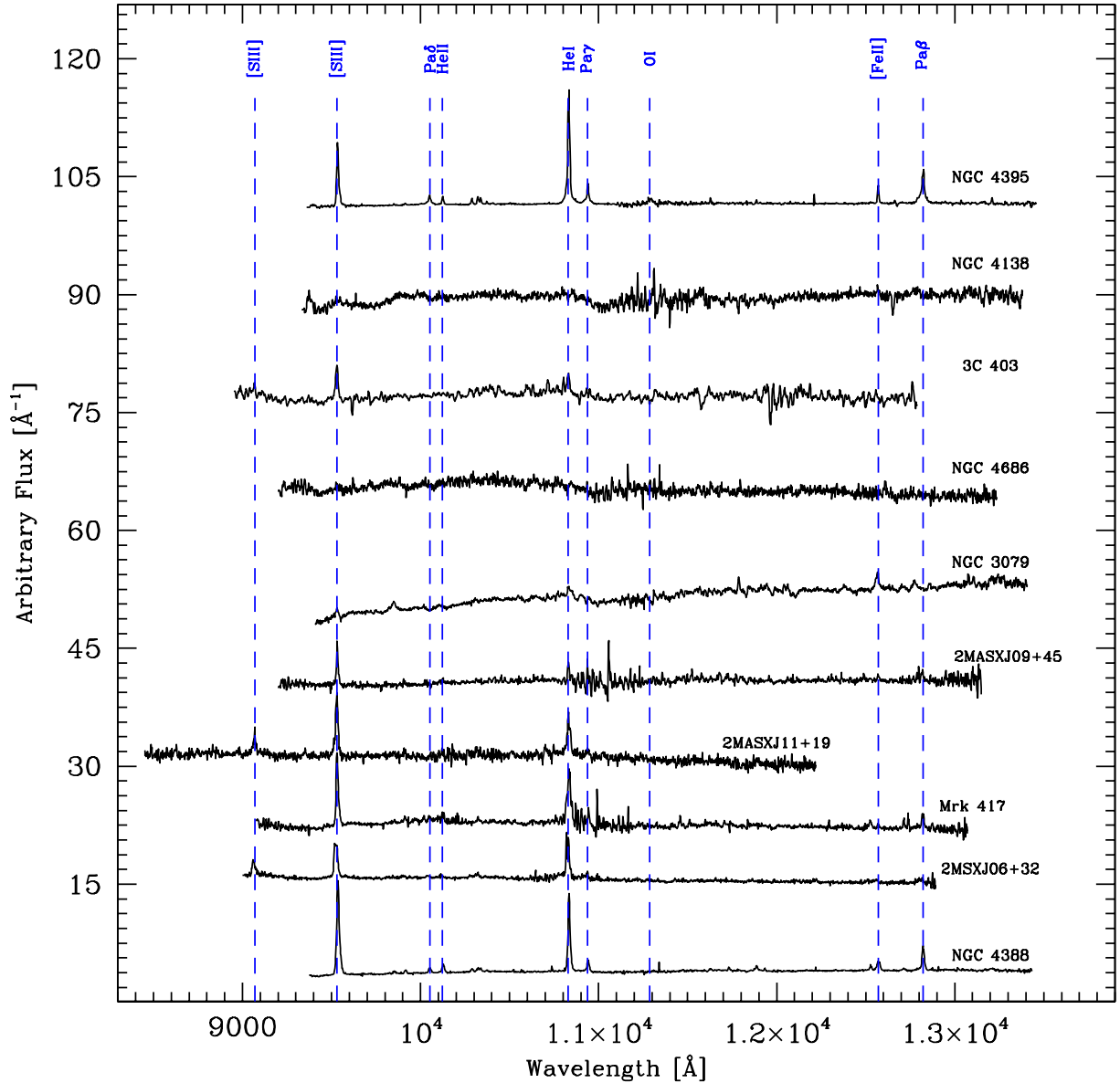
Figure 3. Near infrared spectra, obtained with LUCI/LBT, corrected for redshift. The rest-frame wavelength position of some of the most relevant emission lines are shown by dashed vertical lines. The spectra are flux calibrated, but are shown with arbitrary normalization.

and MCG−05−23−016) were observed by both ISAAC/VLT and X-shooter/VLT. We have also observed one well-known AGN1 with X-shooter (NGC 3783) in order to test our method.

Our sample of 41 AGN2 and 1 AGN1 is listed in Table 1 along with the 14–195 keV luminosity (in the following hard X luminosity), the column density (N_H), the optical classification and the spectrograph used. As shown in Table 1, for most of the sources the N_H values have been retrieved from the literature, while for five sources publicly available X-ray data were analysed. For 3XMM J112716.3+190920, the *–Newton* EPIC-pn data (exposure time of ≈6.2 ks) plus *Swift*/BAT were used, while for ESO 157−G023, ESO 374−G44, 2MASX1830+0928 and ESO 234−G50 the X-ray coverage was provided by multiple *Swift*/XRT and BAT observations; the final exposure time in XRT was ≈10.8, 18.5, 26.5 and 10.7 ks, respectively. To derive the N_H and intrinsic (i.e. absorption-corrected) AGN luminosity of all of these sources, we adopted as a baseline model an absorbed power-law plus a scattering component

(for the soft X-ray emission); only for 3XMM J112716.3+190920 an iron K α emission line (with equivalent width – EW – of ≈80 eV) was detected. In Fig. 1, the redshifts of the 41 observed AGN2 and the total 70-month *Swift*/BAT AGN1 and AGN2 samples, as a function of the hard X-ray luminosity, are shown, while in Fig. 2 we show the hard X-ray luminosity distribution.

3 OBSERVATIONS AND DATA REDUCTION

The observations have been carried out at ESO/VLT and at LBT in the period between 2011 October and 2014 June. All the spectra were taken under a clear sky but with different seeing and airmass conditions (see Table 2). Targets acquisition was carried out paying attention to the centring of the galaxy's nucleus at the best and, when possible, the slit has been rotated in order to include also a star for better OH telluric absorption correction. For each target, the individual spectra were obtained using the nodding technique in

the standard ABBA sequence, in order to obtain a good quality sky correction during the data reduction phase. We have also observed a bright star (O, B, A or solar spectral type) within 30 min to the target observations, which was used for the flux calibration and for correction of the OH absorptions every time the telluric star was not available. Flats and arcs were taken within one day of the observations.

In the following three sections, we describe the spectrographs and the observational setup used for the acquisition.

3.1 LUCI/LBT observations

The LBT NIR Spectrograph Utility with Camera and Integral-Field Unit for Extragalactic Research (LUCI; Seifert et al. 2003) is an NIR spectrograph and imager, mounted on the bent Gregorian focus of the SX mirror of the telescope at LBT observatory (LBTO) in Arizona. The instrument is equipped with Rockwell HAWAII-2

HdCdTe 2048 × 2048 px^2 array and it works in the wavelength range from 0.85 to 2.5 μm, corresponding to the photometric z, J, H and K bands.

We observed a total of 10 AGN2 of our sample in the period 2012 October–2013 February, having $0^h < \alpha < 22^h$ and $\delta > -10°$. All the objects have been acquired in the zJ (0.92–1.5 μm) band using the grating 200 $H+K$ in combination with the zJspec filter. For each object eight images were taken, with exposures of 350 s each. A 1 arcsec × 2.8 arcmin slit was used, corresponding to a resolution $R = \lambda/\Delta\lambda = 1360$ and to a velocity uncertainty of $\sigma_v = 220 \text{ km s}^{-1}$ for the J band ($\lambda_c \sim 11750$ Å) at redshift 0.

3.2 ISAAC/VLT observations

The VLT ISAAC (Moorwood et al. 1998) is an IR (1–5 μm) imager and spectrograph mounted at the Nasmyth A focus of the UT3 of the VLT in Chile. It has two arms, one equipped with the
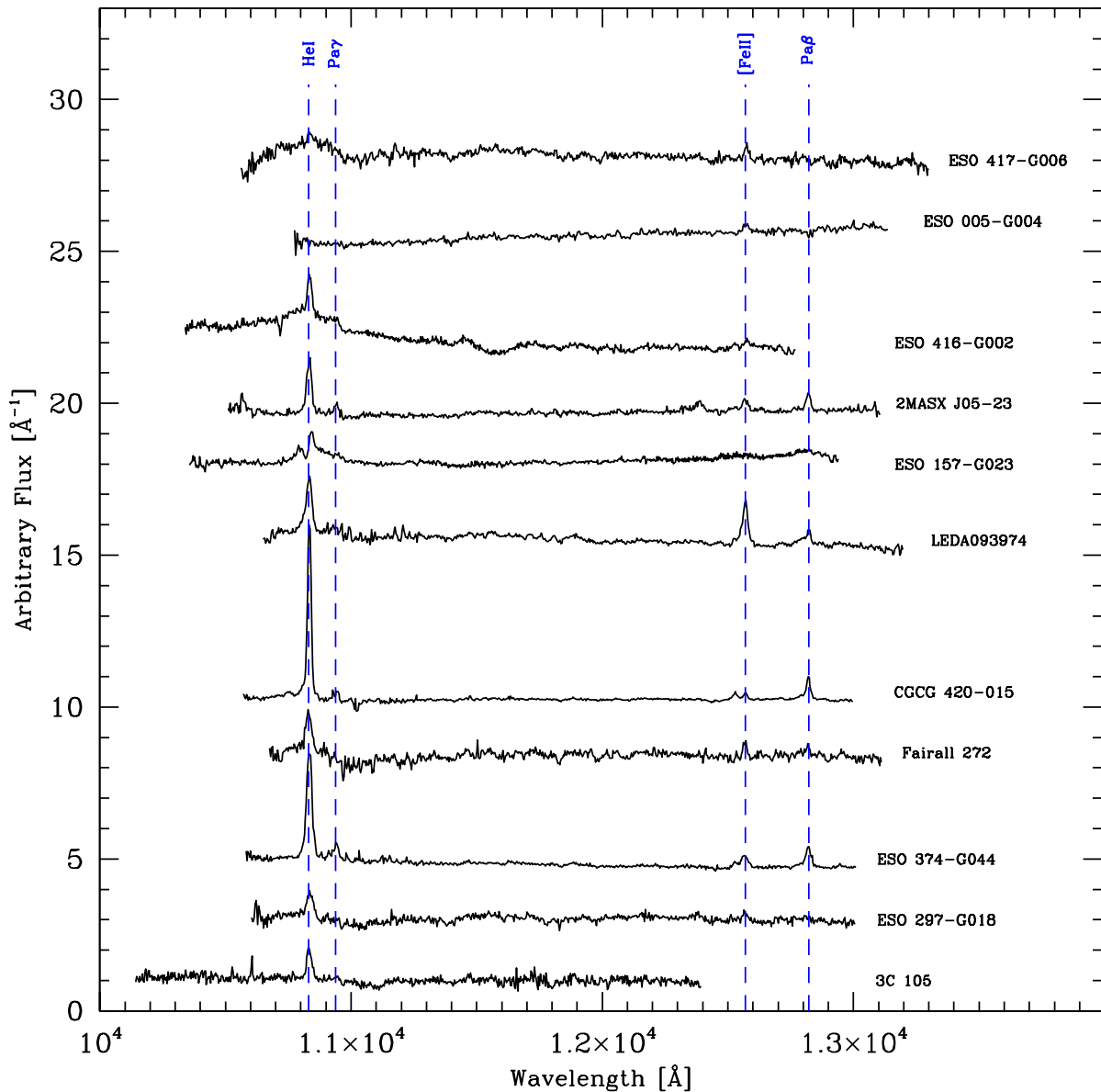
Figure 4. LR NIR spectra, obtained with ISAAC/VLT, corrected for redshift. The rest-frame wavelength position of some of the most relevant emission lines are shown by dashed vertical lines. The spectra are flux calibrated, but are shown with arbitrary normalization.
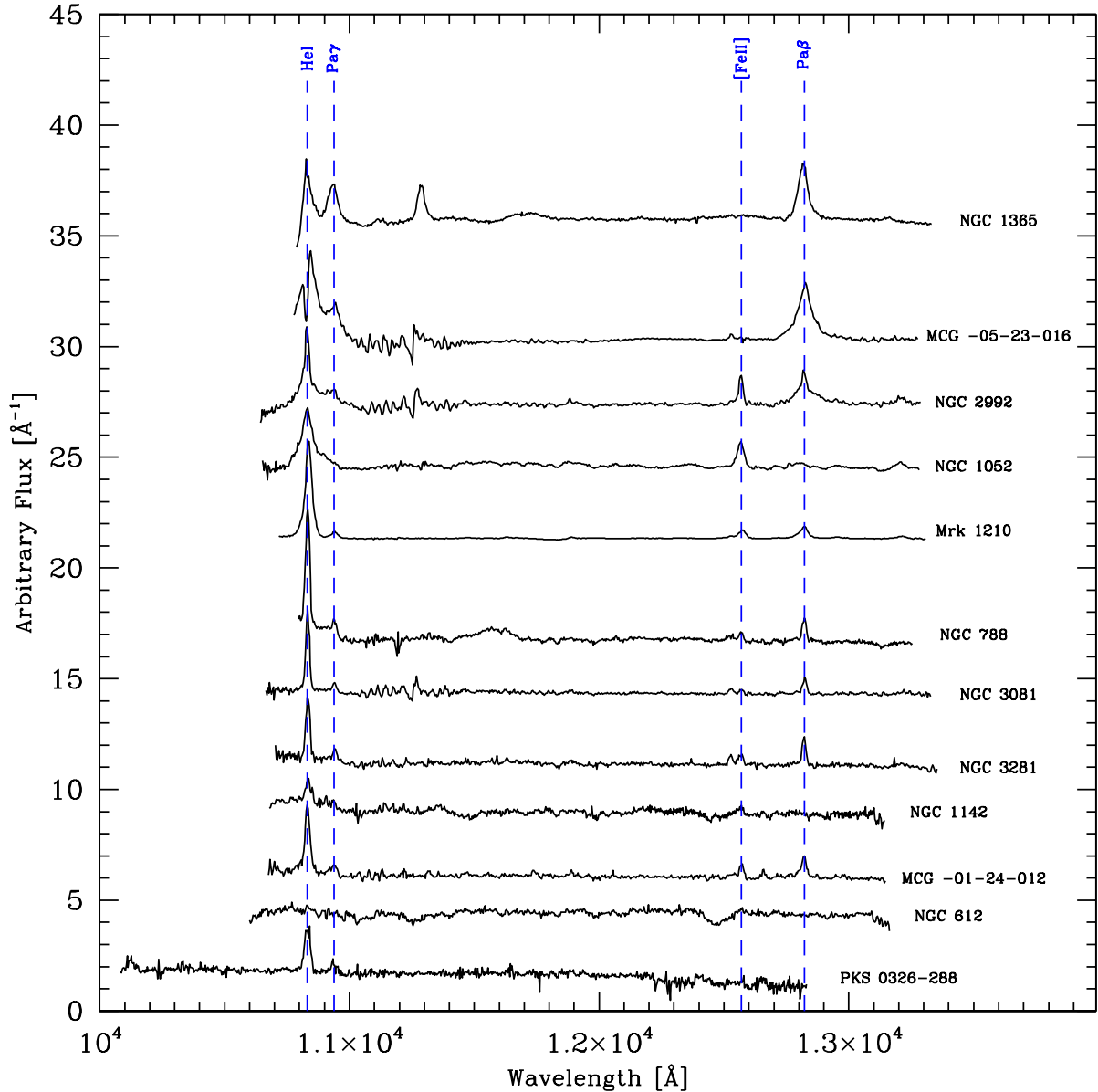
Figure 4 *– continued*

1024 × 1024 Hawaii Rockwell array, used for short wavelength mode (SW; 1–1.5 μm), and the other with a 1024 × 1024 InSb Aladdin array, used for long wavelength mode (LW; 3–5 μm). In spectroscopic mode ISAAC is equipped with two gratings, for Low and Medium resolution spectroscopy (LR and MR, respectively).

23 AGN2 of our sample, having $0^h < \alpha < 12^h$ and $\delta < 10°$, were observed in SW mode in the period 2011 October–2012 January. All the targets have been observed in the *J* band (1.1–1.4 μm), using both LR and MR modes. In particular, in the MR mode the wavelength range was centred where either the Pa β or the He I 10830 Å emission lines were expected, according to the redshift of the source. For each object, we acquired six LR images with exposures of 180 s each and four MR images with exposures of 340 s each. A 0.8 arcsec × 2 arcmin slit was used, corresponding to a spectral resolution $R = 730$ and 4700 (at $\lambda_c \sim 1.2$ μm) and to a velocity uncertainty of $\sigma_v = 430$ km s^{-1} and $\sigma_v = 60$ km s^{-1} (at zero redshift) for LR and MR, respectively.

3.3 X-shooter/VLT observations

X-shooter (Vernet et al. 2011) is a single slit spectrograph mounted to the Cassegrain focus of the VLT UT3, covering in a single exposure the spectral range from the UV to the *K* band (300–2500 nm). The instrument is designed to maximize the sensitivity in the spectral range by splitting the incident light in three arms with optimized optics, coatings, dispersive elements and detectors. It operates at intermediate resolutions, $R = 4000$–18 000, depending on wavelength and slit width. The three arms are fixed format cross-dispersed échelle spectrographs and they operate in parallel.

We have observed 10 AGN2 and one AGN1 from our sample, with $10^h < \alpha < 22^h$ and $\delta < 10°$. The first set of observations (four sources) has been carried out in visitor mode on 2013 February and for each object we acquired two images with exposures, in the NIR band, in the range of 150–300 s each. The second set of X-shooter observations, including seven sources, has been performed in service mode between 2014 April and 2014 June. For
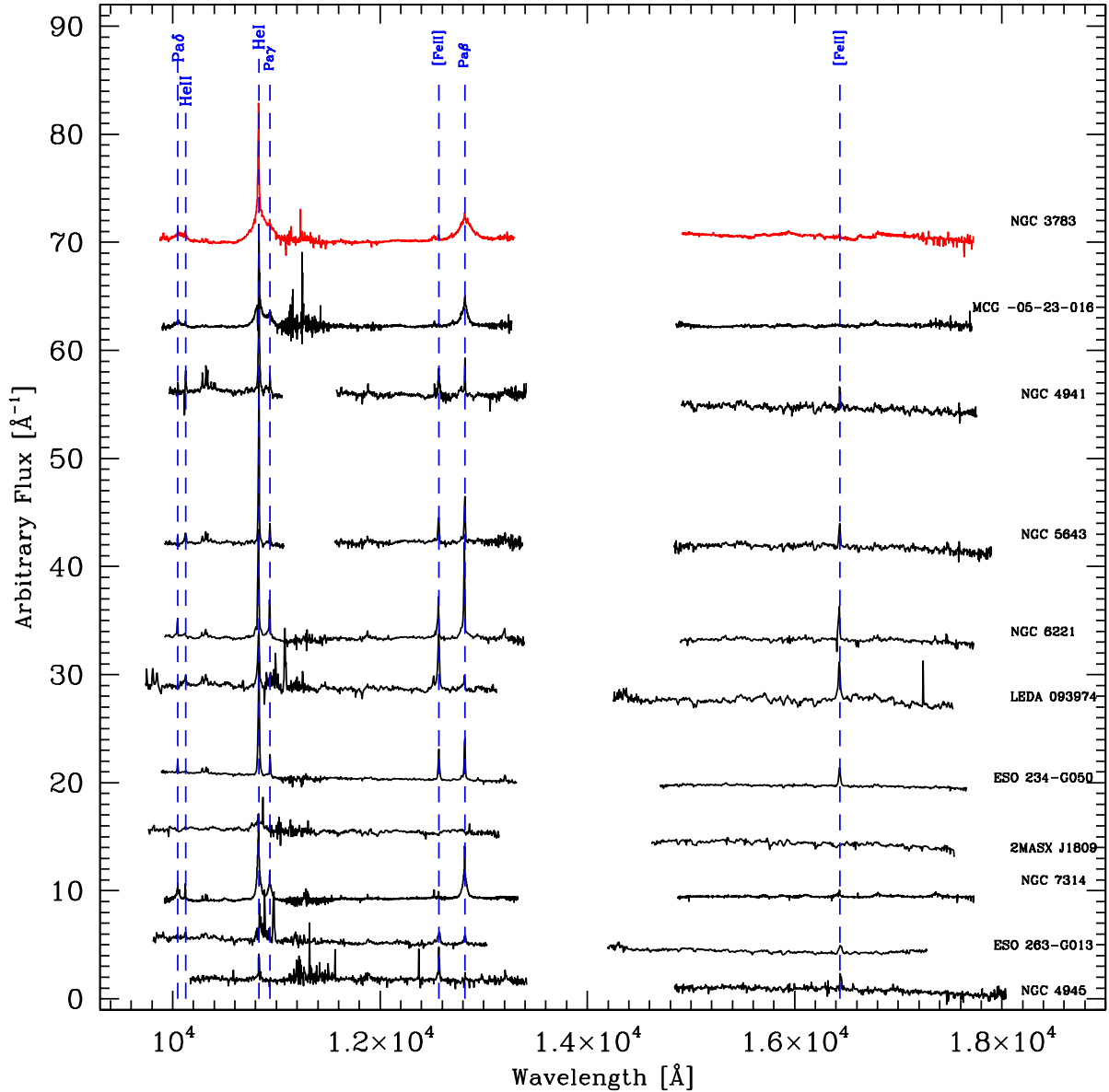
Figure 5. Near infrared spectra obtained with X-shooter/VLT, corrected for redshift. The spectrum of the AGN1 NGC 3783 is shown in red on the top. The rest-frame wavelength position of some of the most relevant emission lines are shown by dashed vertical lines. Wavelength regions of bad atmospheric transmission have been masked out. The spectra are flux calibrated, but are shown with arbitrary normalization.

each object, we acquired 10 images with exposures, in the NIR band, of ∼290 s each.

For both set of observations, a 1.0 arcsec × 11 arcsec slit for the UVB arm and a 0.9 arcsec × 11 arcsec slit for the VIS and NIR arms were used, corresponding to a spectral resolution $R = 4350$ for the UVB arm, $R = 7450$ for the VIS arm and $R = 5300$ for NIR arm, and to a velocity uncertainty of $\sigma_v \sim 70/40/60 \text{ km s}^{-1}$ at zero redshift, in the UVB/VIS/NIR arms, respectively.

3.4 Data reduction

The data reduction was carried out using standard IRAF (Tody 1986) tasks and included flat-field correction, cosmic ray cleaning, wavelength calibration, extraction of spectra from science frames using the optimized method by Horne (1986), telluric absorption correction and flux calibration. The wavelength calibrations made use of

Xe and Ar arc lamps as a reference, and were eventually compared to the OH sky lines in order to apply, when necessary, small offsets due to instrument flexures during the observations. The telluric correction and flux calibration have been carried out by observing bright O, B, A or solar spectral class type stars, just after or before the science observations (Maiolino, Rieke & Rieke 1996; Vacca, Cushing & Rayner 2003). In some cases, when possible, the calibration star has been put in the slit of the science observations, for a better telluric correction. As far as the X-shooter data are concerned, the above data reduction steps were carried out using REFLEX X-shooter pipeline (Freudling et al. 2013).

4 THE EMISSION LINE MEASUREMENTS

In Figs 3–6, all the 42 spectra (41 AGN2 and 1 AGN1), divided according to the instrument used, are shown. We have identified and
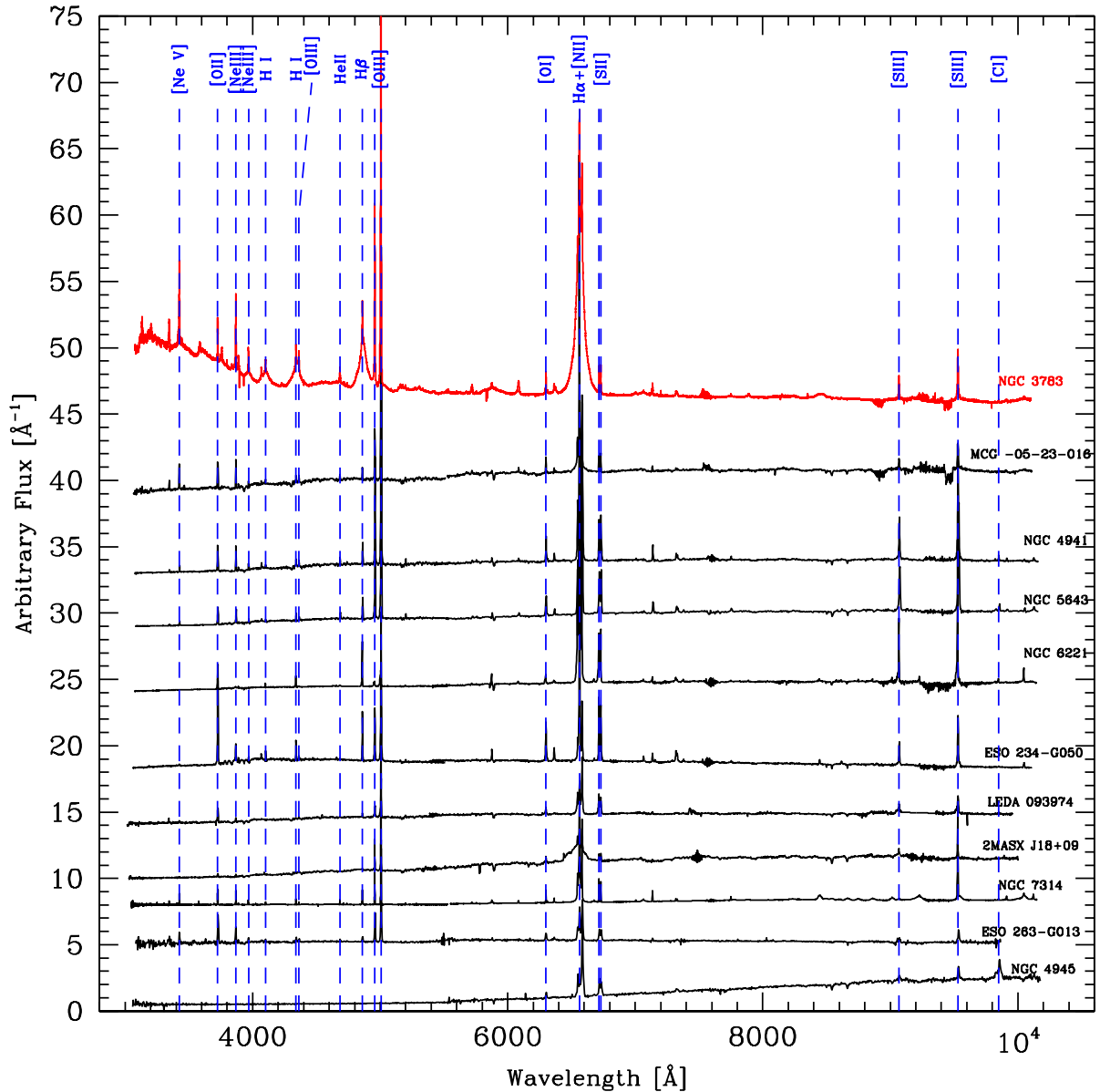
Figure 6. UVB+VIS spectra obtained with X-shooter/VLT, corrected for redshift. The spectrum of the AGN1 NGC 3783 is shown in red on the top. The rest-frame wavelength position of some of the most relevant emission lines are shown by dashed vertical lines. The spectra are flux calibrated, but are shown with arbitrary normalization.

analysed in our spectra the most important NIR and optical emission lines, as listed in Table 3. The vacuum rest-frame wavelengths were used. We have looked for faint broad components both in the Pa β and the He I 10 830 Å emission lines as they are the most prominent permitted emission lines visible in the NIR *J* band. For those objects observed with X-shooter the Hα and Hβ spectral regions were also analysed. Moreover for those objects observed with either LUCI or ISAAC, where a BLR component was detected in the NIR, optical data taken from the literature were also studied.

The 1σ uncertainties provided by the data reduction pipelines, or estimated from featureless regions of the spectra, were used to carry out the fitting using XSPEC 12.7.1 (Arnaud 1996). The local continuum was always modelled with a power law and subtracted, then all significant (using the F-test) components were modelled with Gaussian profiles. All measurements were performed in the redshift corrected spectrum (i.e. in the object rest frame). All the redshifts

were taken from the *Swift*/BAT 70-month catalogue (Baumgartner et al. 2013). We have identified as narrow (N) all the components having widths less than $\sim$500 km s^{-1}, well centred with the wavelength expected from the systemic redshift, and compatible with the forbidden lines widths. At variance, the largest components of the permitted H I and He I lines, significantly larger than the narrow components, have been classified as broad (B). In some cases other intermediate (I) width components, blueshifted with respect to the narrow components, were also identified. When possible, the narrow component of the permitted lines (H I and He I) has been modelled by imposing the same full width at half-maximum (FWHM) found for the narrow component of the forbidden lines in the same spectral band. In the optical, we have imposed that the intensity ratios between the [O III]4959 Å and [O III]5007 Å and between [N II]6548 Å and [N II]6583 Å satisfied the 1:2.99 relation (Osterbrock & Ferland 2006). When intermediate components were found, we have fixed

Table 3. Observed optical and NIR emission lines.

	Optical		NIR	
Element	Vacuum wavelength [Å]		Element	Vacuum wavelength [Å]
(1)	(2)		(3)	(4)
[Ne v]	3346.79		[S iii]	9069.0
[Ne v]	3426.85		[S iii]	9531.0
[O ii]	3728.38		Paε	9548.6
[O ii]	3729.86		[C i]	9853.0
[Fe viii]	3759.69		[S viii]	9911.1
[Ne iii]	3869.86		Paδ	100 52.1
[[Fe v]	3896.33		He ii	101 22.0
[Ne iii]	3968.59		He i	108 30.0
Hγ	4341.69		Pa γ	109 38.0
He ii	4687.02		O i	112 87.0
Hβ	4862.68		[P ii]	118 86.0
[O iii]	4960.30		[S ix]	125 23.0
[O iii]	5008.24		[Fe ii]	125 70.0
[Fe vii]	5722.30		Pa β	128 21.6
He i	5877.25		[Fe ii]	164 36.0
[Fe vii]	6087.98			
[O i]	6302.05			
[O i]	6365.54			
[N ii]	6549.84			
Hα	6564.61			
[N ii]	6585.23			
[S ii]	6718.32			
[S ii]	6732.71			
[O ii]	7322.01			
[Fe xi]	7894.0			

their FWHM and their blueshift Δv to be equal to that measured in the corresponding intermediate components of the most intense forbidden line, observed in the same spectral region. We have found significant broad line components in 13 out of 41 observed AGN2. In Figs 7–19, the fitting models of the spectral regions including the Pa β, He i, Hα and Hβ lines of these 13 AGN2 are shown. The corresponding fitting parameters (FWHM, not yet corrected for the instrumental resolution, EW and Δv) are listed in Tables 4 and 5, while the FWHM values, corrected for instrumental broadening, are listed in Table 7. In Appendix A, more detailed descriptions of the line fittings are discussed, while in Appendix B the spectral fitting of those objects without (secure) evidence of a broad component in the region of the Pa β or He i lines (when the Pa β region was not observed) are shown. In Appendix C, we report the main fitting parameters for all the analysed emission lines of all the 42 spectra: FWHM (not corrected for the instrumental resolution), EW and line flux are listed (Tables C1–C15).

4.1 AGN2 classification

As the activity classification of our AGN sample has been taken from the inhomogeneous compilation of Baumgartner et al. (2013), we decided to use our line measures to independently re-determine the AGN classes through the line ratio diagnostic diagrams (e.g. BPT diagrams; Baldwin, Phillips & Terlevich 1981). The narrow line ratios [O iii]5007/Hβ, [O i]6003/Hα, [O iii]5007/[O ii]3728, [N ii]6583/Hα and [S ii]6716,6731/Hα (in the optical) and [Fe ii]/Pa β (in the NIR; see Veilleux et al. 1997) were used. The line ratios were computed using the fluxes reported in Tables C12 and C15, for the X-shooter AGNs, while we used the EW reported in Table 4 and 5, for the non-X-shooter broad AGN2

(for which optical spectra were taken from the literature). The diagnostic diagrams are shown in Fig. 20. The pure star formation (blue dashed line) and extreme starburst (red dashed line) regions were defined according to Kauffmann et al. (2003) and Kewley et al. (2001), respectively. The separation between AGN2 and low-ionization nuclear emission-line regions (LINERS) was carried out according to Kewley et al. (2006, purple solid line). Moreover, in the diagram showing the [O iii]5007/[O ii]3728 ratio, the starburst region as defined by Kewley et al. (2006, dot–dashed red line) was used. The line ratio diagnostic analysis confirms in general the AGN activity nature of the sources. However, it results that both NGC 1365 and NGC 6221 fall in the high excitation part of the H ii-AGN composite galaxy region, confirming the presence of a strong starburst component in their spectra, as already suggested by other authors (for NGC 6221 see La Franca et al. (2016), and references therein, and for NGC 1365 see Trippe et al. 2010). Interestingly, also ESO 234−G050 is placed in a intermediate zone between the Seyfert and the H ii region. The activity classification results, in addition to our new spectroscopic redshift estimates (which agree, within the uncertainties, with the values listed by Baumgartner et al. 2013), are summarized in Table 6.

4.2 The intrinsic FWHM of the BLR components

In summary, we have found significant evidence of the presence of BLR components in 13 out of 41 AGN2 spectra (in the following called broad AGN2). However, in order to derive the real width of the lines it is necessary to deconvolve the FWHM measurements with the broadening due to the spectral resolution of the instruments used. In Table 7, we list the intrinsic FWHM of the broad components of the Hα, He i and Pa β lines, once corrected for the instrumental broadening. The measured FWHM of the Pa β ranges from ∼800 km s^{-1}(NGC 4395) to ∼2250 km s^{-1}(NGC 6221).

According to Baumgartner et al. (2013), 3 out of our 13 classified broad AGN2 had been previously classified as intermediate (NGC 1365, NGC 4395 and NGC 7314) in the optical, and indeed we detected a faint BLR Hα component in all of them. Moreover, four other optically intermediate class AGN have not shown a significant BLR component in their NIR spectra (2MASX J11271632+1909198, NGC 4138, ESO 416−G002 and PKS 0326−288). It should also be noted that a BLR component of the Hα was detected in 10 out of the 13 broad AGN2. For eight (7) sources, we found a BLR detection on both the Pa β and the He i (Hα) lines. In Fig. 21, we show the comparison between the FWHM of the Hα, He i and Pa β lines when measured on the same object. As already found in other studies (see the data by Landt et al. 2008, in Fig. 21) a fair agreement is found (if the ∼10 per cent uncertainties are taken into account) among all these measurements.

5 ANALYSIS OF POSSIBLE SELECTION EFFECTS

As we have found evidence of BLR components in 13 out of 41 AGN2, it is relevant to investigate whether some selection effect could affect the sample of AGN2 where the BLR was found, or if there are some physical differences between the samples of AGN2 showing (or not) faint BLR components. We have therefore analysed the distributions of the spectral S/N ratio, *J*-band magnitude,

Figure 7. Near infrared and optical spectra of NGC 4395, corrected for redshift (see also La Franca et al. 2015). Top-left: Pa β+[Fe II] region. Top-right: He I+Pa γ region. Bottom-left: Hα+[N II] region. Bottom-right: Hβ+[O III] region. The narrow, intermediate and broad components are shown with green-dashed, blue and red lines, respectively. The magenta-dashed line shows the total fitting model.
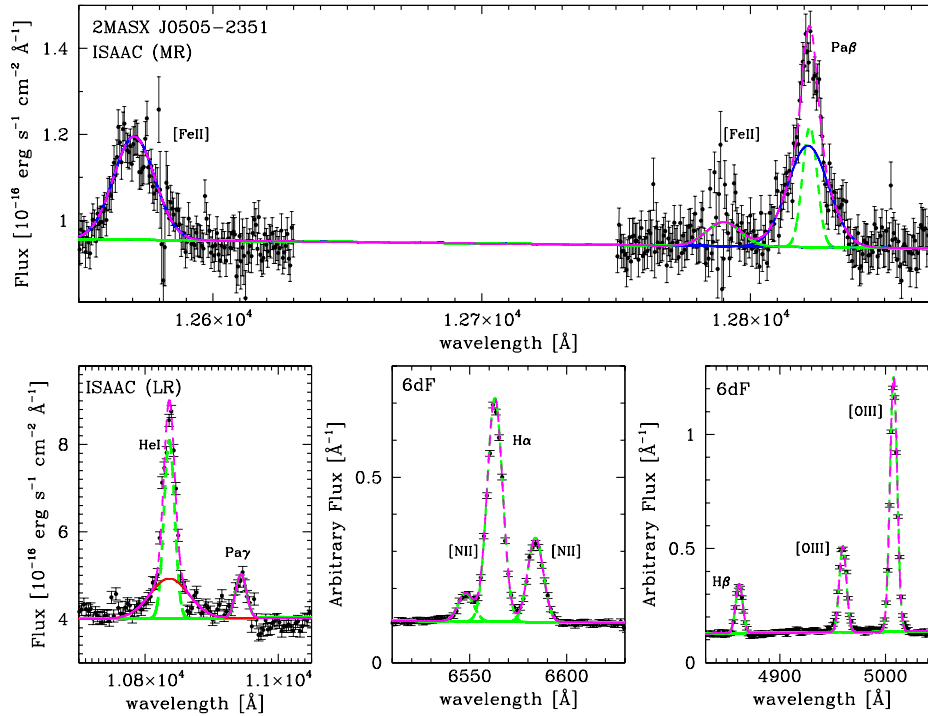
Figure 8. Near infrared and optical spectra of 2MASX J05054575−2351139, corrected for redshift. Top: Pa β+[Fe II] region. Bottom-left: He I+Pa γ region. Bottom-middle: Hα+[N II] region. Bottom-right: Hβ+[O III] region. The narrow, intermediate and broad components are shown with green-dashed, blue and red lines, respectively. The magenta-dashed line shows the total fitting model.
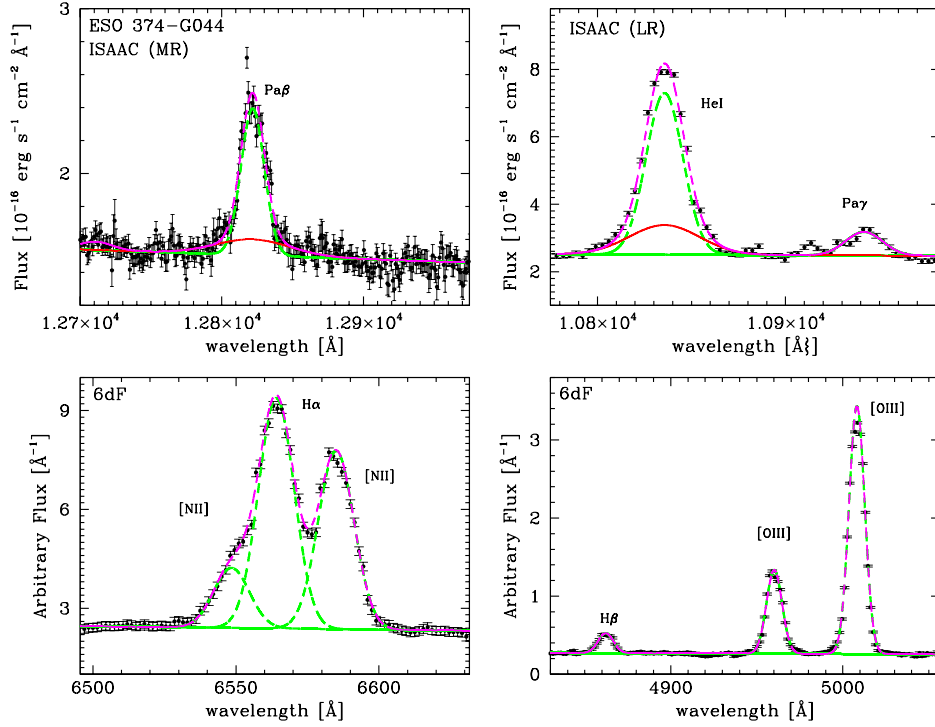
Figure 9. Near infrared and optical spectra of ESO 374−G044, corrected for redshift. Top-left: Pa β+[Fe II] region. Top-right: He I+Pa γ region. Bottom-left: Hα+[N II] region. Bottom-right: Hβ+[O III] region. The narrow, intermediate and broad components are shown with green-dashed, blue and red lines, respectively. The magenta-dashed line shows the total fitting model.
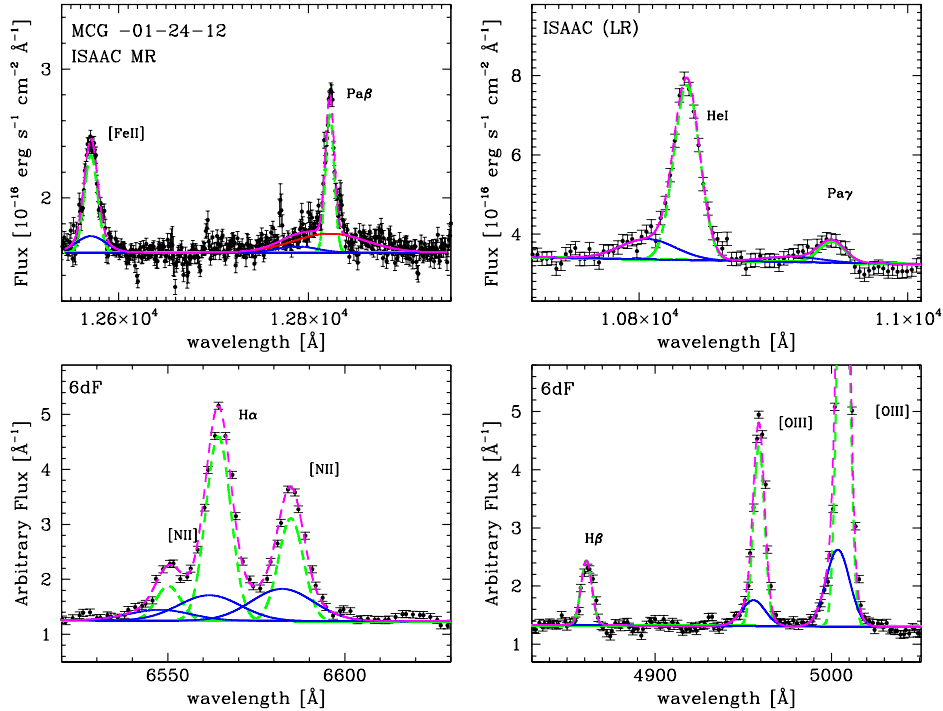
Figure 10. Near infrared and optical spectra of MCG−01−24−012, corrected for redshift (see also La Franca et al. 2015). Top-left: Pa β+[Fe II] region. Top-right: He I+Pa γ region. Bottom-left: Hα+[N II] region. Bottom-right: Hβ+[O III] region. The narrow, intermediate and broad components are shown with green-dashed, blue and red lines, respectively. The magenta-dashed line shows the total fitting model.
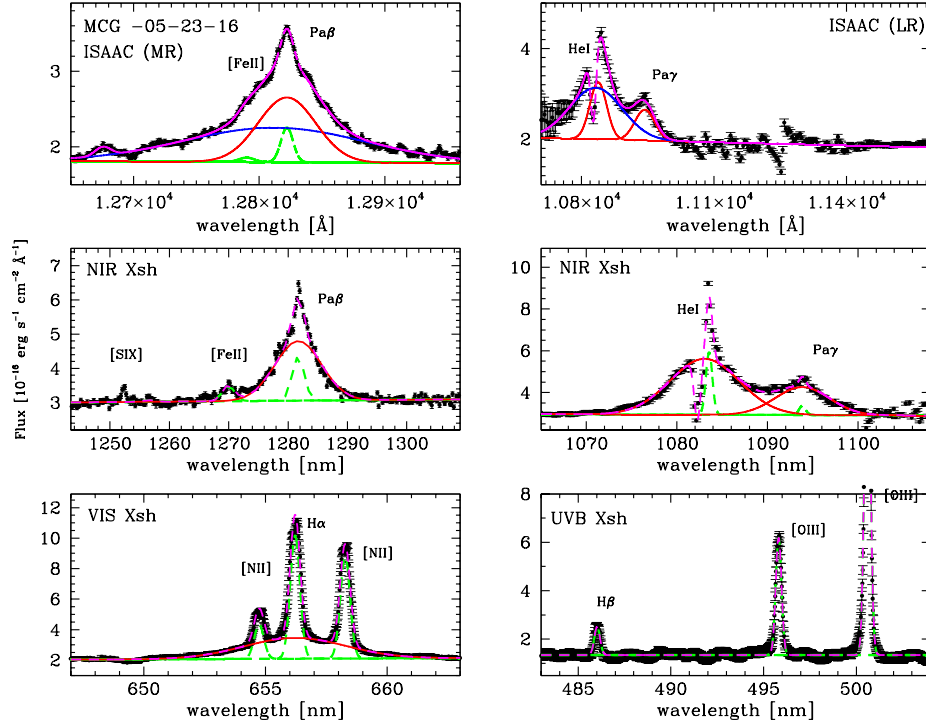
Figure 11. Near infrared and optical spectra of MCG−05−23−016, corrected for redshift. Top-left: ISAAC MR Pa β+[Fe II] region. Top-right: ISAAC LR He I+Pa γ region. Center-left: X-shooter Pa β+[Fe II] region. Center-right: X-shooter He I+Pa γ region. Bottom-left: X-shooter Hα+[N II] region. Bottom-right: X-shooter Hβ+[O III] region. The narrow, intermediate and broad components are shown with green-dashed, blue and red lines, respectively. The magenta-dashed line shows the total fitting model.
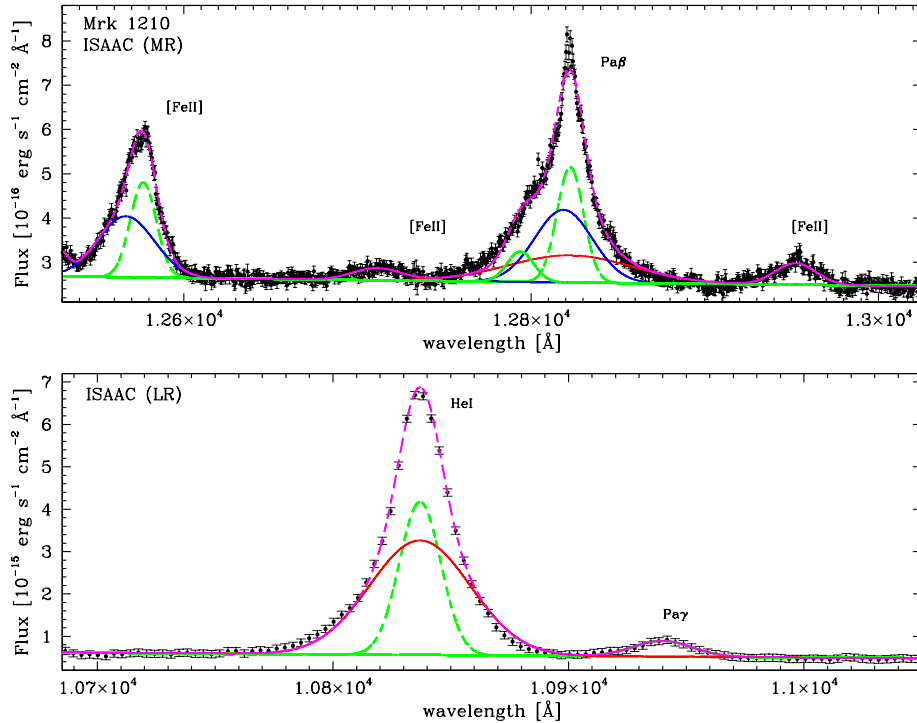
Figure 12. Near infrared spectrum of Mrk 1210, corrected for redshift. Top: Pa β+[Fe II] region. Bottom: He I+Pa γ region. The narrow, intermediate and broad components are shown with green-dashed, blue and red lines, respectively. The magenta-dashed line shows the total fitting model.
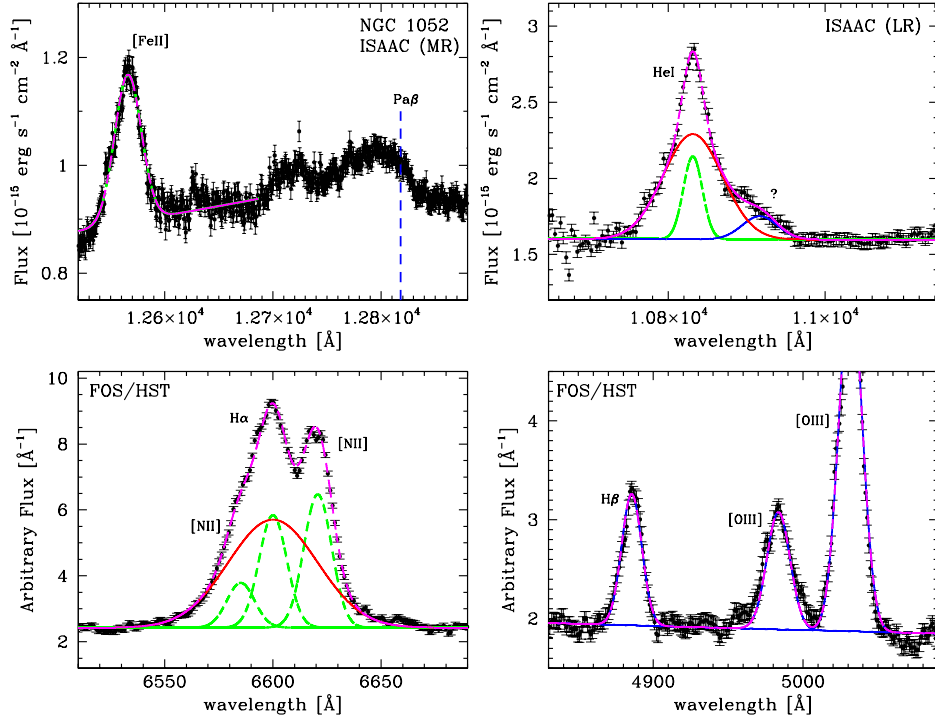
Figure 13. Near infrared and optical spectra of NGC 1052, corrected for redshift. Top-left: Pa β+[Fe II] region. Top-right: He I+Pa γ region. Bottom-left: Hα+[N II] region. Bottom-right: Hβ+[O III] region. The narrow, intermediate and broad components are shown with green-dashed, blue and red lines, respectively. The magenta-dashed line shows the total fitting model. The blue-dashed vertical line indicate the Pa β position.
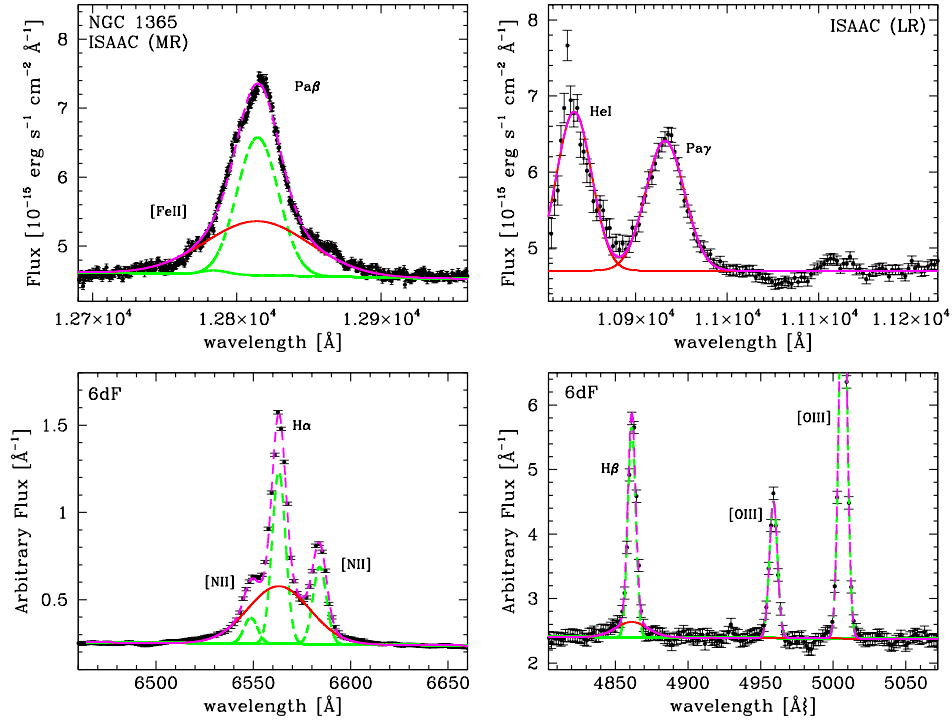
Figure 14. Near infrared and optical spectra of NGC 1365, corrected for redshift. Top-left: Pa β region. Top-right: He I+Pa γ region. Bottom-left: Hα+[N II] region. Bottom-right: Hβ+[O III] region. The narrow, intermediate and broad components are shown with green-dashed, blue and red lines, respectively. The magenta-dashed line shows the total fitting model.
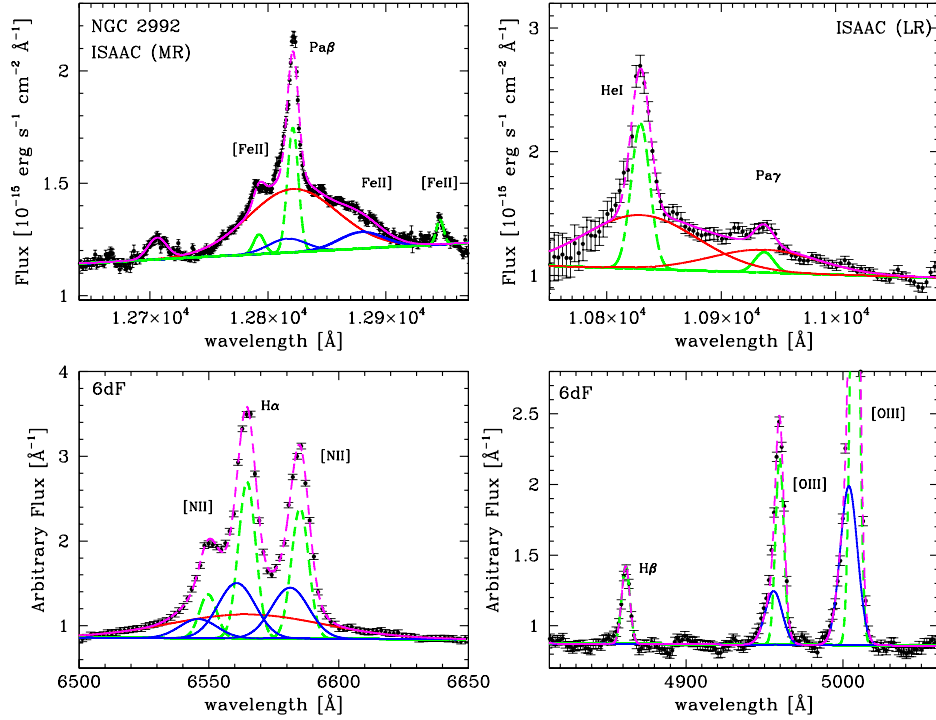
Figure 15. Near infrared and optical spectra of NGC 2992, corrected for redshift. Top-left: Pa β+[Fe II] region. Top-right: He I+Pa γ region. Bottom-left: Hα+[N II] region. Bottom-right: Hβ+[O III] region. The narrow, intermediate and broad components are shown with green-dashed, blue and red lines, respectively. The magenta-dashed line shows the total fitting model.
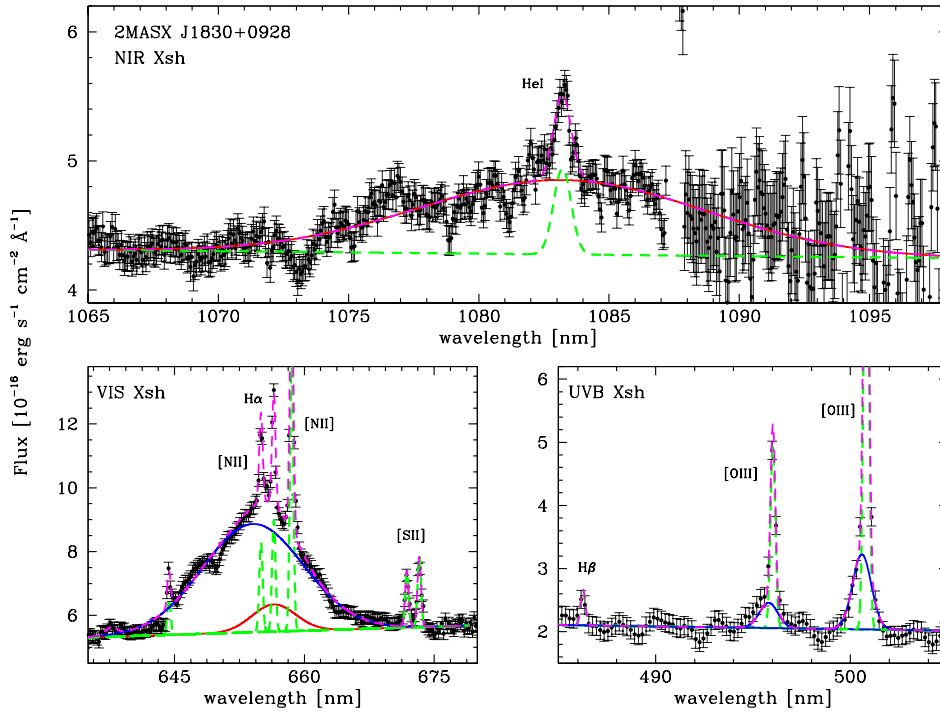
Figure 16. Near infrared and optical spectra of 2MASX J18305065+0928414, corrected for redshift. Top: He I region. Bottom-left: Hα+[N II] region. Bottom-right: Hβ+[O III] region. The narrow, intermediate and broad components are shown with green-dashed, blue and red lines, respectively. The magenta-dashed line shows the total fitting model.
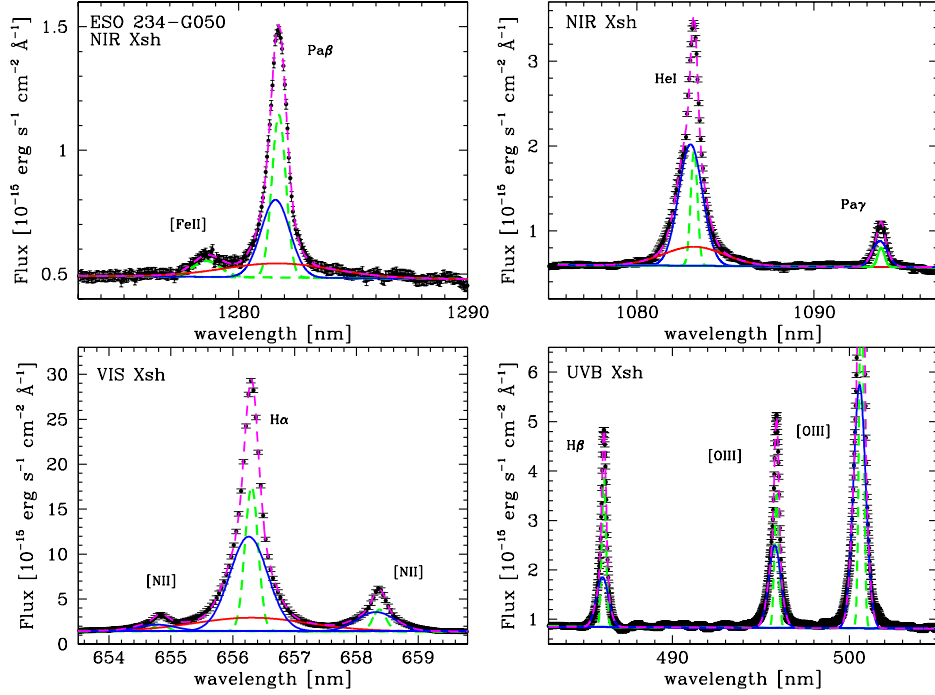
Figure 17. Near infrared and optical spectra of ESO 234−G050, corrected for redshift. Top-left: Pa β+[Fe II] region. Top-right: He I+Pa γ region. Bottom-left: Hα+[N II] region. Bottom-right: Hβ+[O III] region. The narrow, intermediate and broad components are shown with green-dashed, blue and red lines, respectively. The magenta-dashed line shows the total fitting model.
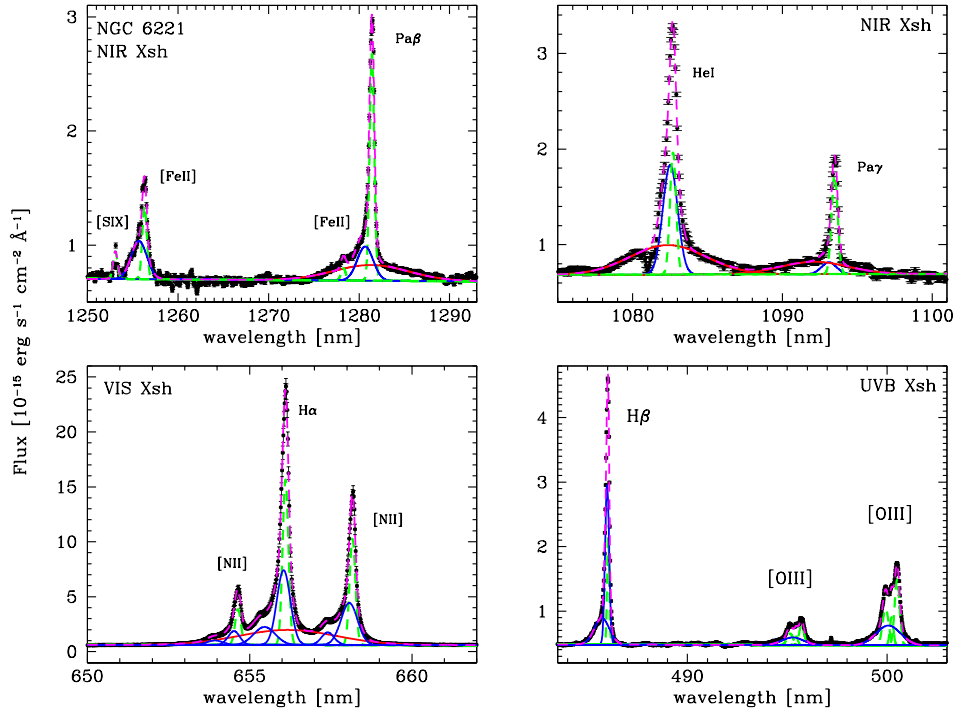
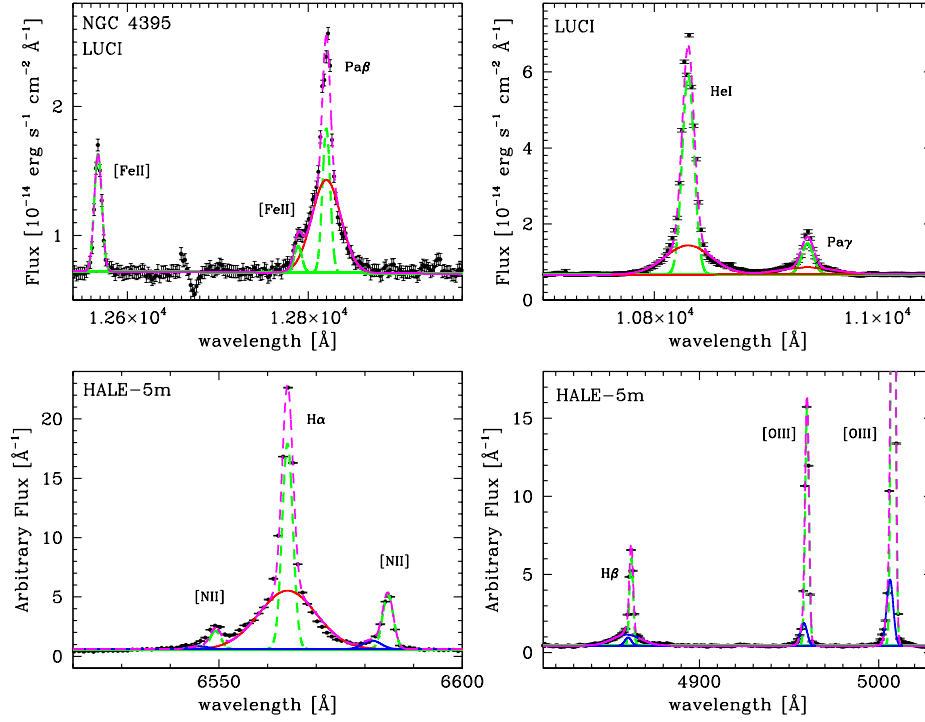**Figure 18.** Near infrared and optical spectra of NGC 6221, corrected for redshift (see also La Franca et al. 2016). Top-left: Pa β+[Fe II] region. Top-right: He I+Pa γ region. Bottom-left: Hα+[N II] region. Bottom-right: Hβ+[O III] region. The narrow, intermediate and broad components are shown with green-dashed, blue and red lines, respectively. The magenta-dashed line shows the total fitting model.
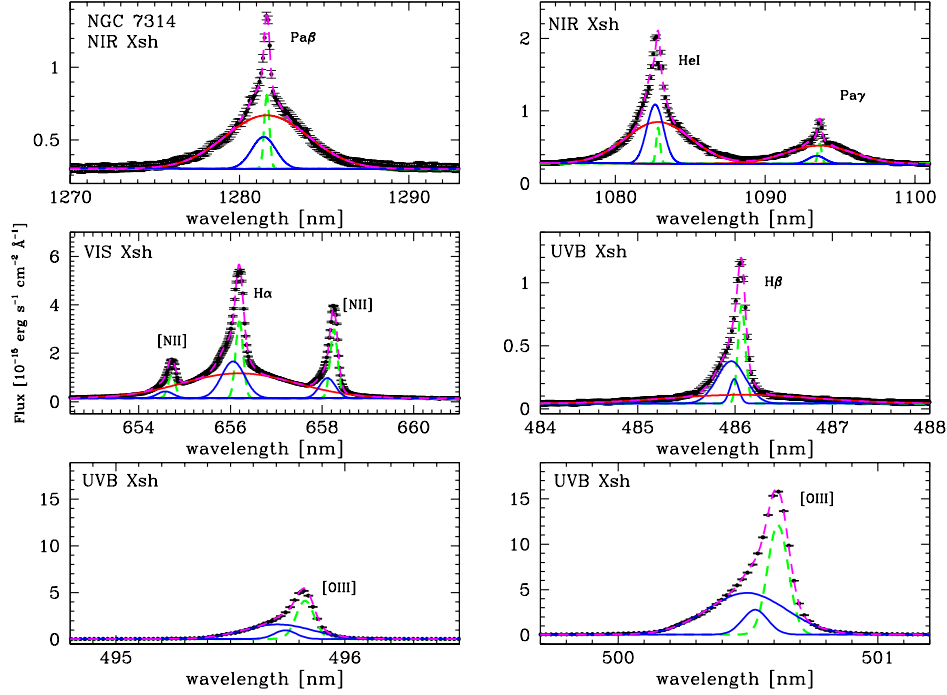
Figure 19. Near infrared and optical spectra of NGC 7314, corrected for redshift. Top-left: Pa β+[Fe II] region. Top-right: He I+Pa γ region. Center-left: Hα+[N II] region. Center-right: Hβ+[O III] region. Bottom-left: [O III]λ4959 region. Bottom-right: [O III]λ5007 region. The narrow, intermediate and broad components are shown with green-dashed, blue and red lines, respectively. The magenta-dashed line shows the total fitting model.

Table 4. Line measurements of the optical emission lines of the 'broad' AGN2.

Comp	Hβ			[O III]4959Å			[O III]5007Å			[N II]6548 Å			Hα			[N II]6583Å		
	FWHM	Δv	EW	FWHM	Δv	EW	FWHM	Δv	EW	FWHM	Δv	EW	FWHM	Δv	EW	FWHM	Δv	EW
(1)	(2)	(3)	(4)	(5)	(6)	(7)	(8)	(9)	(10)	(11)	(12)	(13)	(14)	(15)	(16)	(17)	(18)	(19)
	2MASX J05054575−2351139 (Jones et al. 2009); $R = 1000$ ($\sigma_v \sim 300\,\mathrm{km\,s^{-1}}$)																	
N	466^{+4}_{-4}	–	13.9	466^{+4}_{-4}	–	23.9	466^{+4}_{-4}	–	70.2	413^{+6}_{-6}	–	6.8	413^{+6}_{-6}	–	54.3	413^{+6}_{-6}	–	20.7
	2MASX J18305065+0928414 X-shooter (UVB;VIS); $R = 4350/7350$ ($\sigma_v \sim 70/40\,\mathrm{km\,s^{-1}}$)																	
N	176^{+7}_{-8}	–	0.8	176^{+7}_{-8}	–	4.4	176^{+7}_{-8}	–	13.3	216^{+12}_{-9}	–	2.6	216^{+12}_{-9}	–	3.3	216^{+12}_{-9}	–	7.8
I	–	–	–	663^{+74}_{-65}	134	2.3	663^{+74}_{-65}	134	7.0	–	–	–	–	–	–	–	–	–
B	–	–	–	–	–	–	–	–	–	–	–	–	2660^{+500}_{-460}	–	9.8	–	–	–
I	–	–	–	–	–	–	–	–	–	–	–	–	6194^{+160}_{-160}	1103	90.9	–	–	–
	ESO 234-G050 X-shooter (UVB;VIS); $R = 4350/7350$ ($\sigma_v \sim 70/40\,\mathrm{km\,s^{-1}}$)																	
N	172^{+2}_{-2}	–	10.7	172^{+2}_{-2}	–	8.9	172^{+2}_{-2}	–	26.8	113^{+3}_{-4}	–	1.5	113^{+3}_{-4}	–	29.7	113^{+3}_{-4}	–	4.5
I	481^{+2}_{-2}	50	10.0	481^{+2}_{-2}	62	15.4	481^{+2}_{-2}	62	46.3	327^{+7}_{-10}	25	3.8	327^{+7}_{-10}	25	56.2	327^{+7}_{-10}	25	11.5
B	–	–	–	–	–	–	–	–	–	–	–	–	972^{+124}_{-104}	–	20.7	–	–	–
	ESO 374-G044 (Jones et al. 2009); $R = 1000$ ($\sigma_v \sim 300\,\mathrm{km\,s^{-1}}$)																	
N	640^{+5}_{-10}	–	10.5	640^{+5}_{-10}	–	46.3	640^{+5}_{-10}	–	140.4	669^{+9}_{-9}	–	11.8	669^{+9}_{-9}	–	45.9	669^{+9}_{-9}	–	35.9
	MCG -01-24-012 (Jones et al. 2009); $R = 1000$ ($\sigma_v \sim 300\,\mathrm{km\,s^{-1}}$)																	
N	440^{+8}_{-10}	–	6.5	440^{+8}_{-10}	–	18.7	440^{+8}_{-10}	–	56.2	371^{+14}_{-13}	–	4.4	371^{+14}_{-13}	–	23.7	371^{+14}_{-13}	–	13.3
I	–	–	–	926^{+80}_{-70}	189	5.6	926^{+80}_{-70}	189	16.8	926^{+80}_{-70}	111	3.4	926^{+80}_{-70}	111	8.2	926^{+80}_{-70}	111	10.4
	MCG -05-23-016 X-shooter (UVB;VIS); $R = 4350/7350$ ($\sigma_v \sim 70/40\,\mathrm{km\,s^{-1}}$)																	
N	221^{+4}_{-3}	–	3.3	221^{+4}_{-3}	–	14.1	221^{+4}_{-3}	–	42.2	215^{+2}_{-2}	–	5.4	215^{+2}_{-2}	–	19.4	215^{+2}_{-2}	–	16.0
B	–	–	–	–	–	–	–	–	–	–	–	–	2232^{+36}_{-38}	–	34.2	–	–	–
	NGC 1052 (Torrealba et al. 2012); $R = 2800$ ($\sigma_v \sim 80\,\mathrm{km\,s^{-1}}$)																	
N	967^{+49}_{-40}	–	11.6	1091^{+16}_{-16}	–	12.2	1091^{+16}_{-16}	–	36.7	682^{+7}_{-7}	–	9.0	682^{+7}_{-7}	–	22.6	682^{+7}_{-7}	–	26.8
B	–	–	–	–	–	–	–	–	–	–	–	–	2193^{+51}_{-45}	–	69.6	–	–	–

Table 4 – *continued*

Comp	Hβ FWHM	Δv	EW	[O III]4959Å FWHM	Δv	EW	[O III]5007Å FWHM	Δv	EW	[N II]6548Å FWHM	Δv	EW	Hα FWHM	Δv	EW	[N II]6583Å FWHM	Δv	EW
(1)	(2)	(3)	(4)	(5)	(6)	(7)	(8)	(9)	(10)	(11)	(12)	(13)	(14)	(15)	(16)	(17)	(18)	(19)
							NGC 1365 (Jones et al. 2009); $R = 1000$ ($\sigma_v \sim 300\,\mathrm{km\,s^{-1}}$)											
N	389^{+7}_{-8}	–	9.1	389^{+7}_{-8}	–	6.1	389^{+7}_{-8}	–	18.3	371^{+3}_{-3}	–	5.2	371^{+3}_{-3}	–	34.8	371^{+3}_{-3}	–	15.8
B	1586^{+517}_{-413}	–	2.7		–		–	–	–	–	–	–	1701^{+31}_{-32}	–	53.4	–	–	–
							NGC 2992 (Jones et al. 2009); $R = 1000$ ($\sigma_v \sim 300\,\mathrm{km\,s^{-1}}$)											
N	375^{+10}_{-10}	–	4.1	375^{+10}_{-10}	–	10.1	375^{+10}_{-10}	–	30.4	358^{+13}_{-13}	–	5.1	358^{+13}_{-13}	–	18.2	358^{+13}_{-13}	–	15.2
I	–	–	–	766^{+35}_{-33}	230	5.6	766^{+35}_{-33}	230	17.9	766^{+35}_{-33}	174	4.7	766^{+35}_{-33}	174	13.8	766^{+35}_{-33}	174	12.7
B	–	–	–	–	–	–	–	–	–	–	–	–	3153^{+436}_{-354}	–	24.5	–	–	–
							NGC 4395 (Ho, Filippenko & Sargent 1995); $R = 2600$ ($\sigma_v \sim 115\,\mathrm{km\,s^{-1}}$)											
N	151^{+1}_{-1}	–	32.3	151^{+1}_{-1}	–	88.9	151^{+1}_{-1}	–	264.0	119^{+2}_{-2}	–	7.1	119^{+2}_{-2}	–	79.4	119^{+2}_{-2}	–	21.1
I	258^{+11}_{-12}	257	5.2	258^{+11}_{-12}	257	14.2	258^{+11}_{-12}	257	42.3	199^{+81}_{-98}	148	1.8	–	–	–	199^{+81}_{-98}	148	5.5
I	1145^{+87}_{-90}	381	30.7	–	–	–	–	–	–	–	–	–	–	–	–	–	–	–
B	–	–	–	–	–	–	–	–	–	–	–	–	633^{+20}_{-18}	–	120.0	–	–	–
							NGC 6221 X-shooter (UVB;VIS); $R = 4350/7350$ ($\sigma_v \sim 70/40\,\mathrm{km\,s^{-1}}$)											
N	79^{+2}_{-1}	–	4.7	177^{+4}_{-2}	–	2.1	177^{+4}_{-2}	–	6.5	90^{+4}_{-3}	–	9.9	90^{+4}_{-3}	–	48.0	90^{+4}_{-3}	–	29.9
I	146^{+2}_{-4}	31	12.9	125^{+5}_{-5}	166	0.6	125^{+5}_{-5}	166	2.0	192^{+8}_{-13}	21	8.8	192^{+8}_{-13}	21	50.9	192^{+8}_{-13}	21	26.6
I	541^{+13}_{-13}	195	7.8	212^{+3}_{-4}	346	1.4	212^{+3}_{-4}	346	4.3	500^{+12}_{-7}	172	11.3	500^{+12}_{-7}	172	45.7	500^{+12}_{-7}	172	33.9
I	–	–	–	851^{+16}_{-10}	261	3.0	851^{+16}_{-10}	261	9.5	77^{+16}_{-8}	375	0.4	77^{+16}_{-8}	375	1.1	77^{+16}_{-8}	375	1.1
B	–	–	–	–	–	–	–	–	–	–	–	–	1630^{+12}_{-11}	–	59.0	–	–	–
							NGC 7314 X-shooter (UVB;VIS); $R = 4350/7350$ ($\sigma_v \sim 70/40\,\mathrm{km\,s^{-1}}$)											
N	56^{+1}_{-1}	–	17.9	56^{+1}_{-1}	–	83.6	56^{+1}_{-1}	–	250.4	89^{+1}_{-1}	–	13.5	89^{+1}_{-1}	–	45.2	89^{+1}_{-1}	–	40.6
I	68^{+1}_{-1}	47	5.5	68^{+1}_{-1}	47	23.1	68^{+1}_{-1}	47	69.1	187^{+2}_{-2}	63	8.5	270^{+2}_{-2}	63	66.8	187^{+2}_{-2}	63	25.5
I	213^{+1}_{-1}	67	29.5	213^{+1}_{-1}	67	120.5	213^{+1}_{-1}	67	361.0	–	–	–	–	–	–	–	–	–
B	1097^{+57}_{-63}	–	31.2	–	–	–	–	–	–	–	–	–	1330^{+5}_{-4}	–	223.0	–	–	–

Notes. (1) Line components. B: BLR, N: NLR, I: intermediate (see Section 4 for the classification criteria); (2)–(19) FWHM [km s^{-1}] (not deconvolved for the instrumental resolution), wavelength shift of the component's centre relative to its narrow component [km s^{-1}], component's EW [Å]. The object name, the reference of the optical spectrum, the instrumental resolution and the corresponding velocity resolution σ_v [km s^{-1}] are also reported.

Table 5. Line measurements of the NIR emission lines of the 'broad' AGN2.

Comp	He I FWHM	Δv	EW	Pa γ FWHM	Δv	EW	[Fe II]12570Å FWHM	Δv	EW	Pa β FWHM	Δv	EW
(1)	(2)	(3)	(4)	(5)	(6)	(7)	(8)	(9)	(10)	(11)	(12)	(13)
				2MASX J05054575-2351139, ISAAC/VLT (MR/LR), $R = 4700/R = 730$ ($\sigma_v \sim 60/430\,\mathrm{km\,s^{-1}}$)								
N	507^{+49}_{-40}	–	20.5	507^{+49}_{-40}	–	5.1	–	–	–	145^{+30}_{-26}	–	2.0
I	–	–	–	–	–	–	413^{+40}_{-38}	–	4.8	405^{+67}_{-49}	–	4.8
B	1823^{+419}_{-318}	–	16.7	–	–	–	–	–	–	–	–	–
				2MASX J18305065+0928414, X-shooter/VLT, $R = 5300$ ($\sigma_v \sim 57\,\mathrm{km\,s^{-1}}$)								
N	216^{+12}_{-9}	–	1.3	–	–	–	–	–	–	–	–	–
B	3513^{+232}_{-213}	–	18.6	–	–	–	–	–	–	–	–	–
				ESO 234-G050, X-shooter/VLT, $R = 5300$ ($\sigma_v \sim 57\,\mathrm{km\,s^{-1}}$)								
N	122^{+12}_{-11}	–	10.9	122^{+12}_{-11}	–	1.9	122^{+12}_{-11}	–	3.9	167^{+11}_{-13}	–	10.4
I	434^{+7}_{-7}	55	40.9	272^{+26}_{-24}	19	5.7	490^{+26}_{-23}	9	14.8	343^{+63}_{-57}	35	10.2
B	1111^{+63}_{-59}	–	16.4	–	–	–	–	–	–	1305^{+381}_{-322}	–	7.1

Table 5 – *continued.*

Comp (1)	He I FWHM (2)	Δv (3)	EW (4)	Pa γ FWHM (5)	Δv (6)	EW (7)	[Fe II]12570Å FWHM (8)	Δv (9)	EW (10)	Pa β FWHM (11)	Δv (12)	EW (13)
				ESO 374-G044, ISAAC/VLT (MR/LR), $R = 4700/R = 730$ ($\sigma_v \sim 60/430\,\mathrm{km\,s^{-1}}$)								
N	632^{+29}_{-36}	–	48.9	632^{+29}_{-36}	–	7.0	–	–	–	450^{+27}_{-42}	–	12.2
I	–	–	–	–	–	–	652^{+74}_{-56}	–	10.2	–	–	–
B	1202^{+383}_{-221}	–	16.3	–	–	–	–	–	–	1413^{+318}_{-294}	–	4.2
				MCG -01-24-012, ISAAC/VLT (MR/LR), $R = 4700/R = 730$ ($\sigma_v \sim 60/430\,\mathrm{km\,s^{-1}}$)								
N	616^{+28}_{-27}	–	31.9	616^{+28}_{-27}	–	4.0	381^{+78}_{-117}	–	8.3	245^{+17}_{-16}	–	7.7
I	1325^{+347}_{-251}	806	7.9	1325^{+347}_{-251}	806	2.2	857^{+121}_{-273}	–	3.1	1325^{+347}_{-251}	806	1.5
B	–	–	–	–	–	–	–	–	–	2070^{+300}_{-280}	–	8.9
				MCG -05-23-016, ISAAC/VLT (MR/LR), $R = 4700/R = 730$ ($\sigma_v \sim 60/430\,\mathrm{km\,s^{-1}}$)								
N	–	–	–	–	–	–	–	–	–	247^{+19}_{-18}	–	3.1
B	1223^{+90}_{-80}	–	29.8	1451^{+134}_{-149}	–	19.5	–	–	–	1165^{+27}_{-18}	–	27.4
I	3855^{+172}_{-158}	–	84.7	–	–	–	–	–	–	3695^{+335}_{-196}	227	46.1
				MCG -05-23-016, X-shooter/VLT, $R = 5300$ ($\sigma_v \sim 57\,\mathrm{km\,s^{-1}}$)								
N	233^{+15}_{-15}	–	9.2	233^{+15}_{-15}	–	1.4	560^{+80}_{-77}	–	0.5	560^{+80}_{-77}	–	10.7
B	2474^{+67}_{-64}	–	87.4	1911^{+105}_{-79}	–	34.3	–	–	–	2134^{+93}_{-89}	–	55.7
				Mrk 1210, ISAAC/VLT (MR/LR), $R = 4700/R = 730$ ($\sigma_v \sim 60/430\,\mathrm{km\,s^{-1}}$)								
N	564^{+8}_{-8}	–	141.4	–	–	–	414^{+18}_{-18}	–	15.1	414^{+18}_{-18}	–	19.5
I	–	–	–	791^{+122}_{-116}	–	22.0	902^{+114}_{-61}	136	21.1	902^{+114}_{-61}	136	26.7
B	1374^{+73}_{-32}	–	258.0	–	–	–	–	–	–	1937^{+118}_{-225}	–	21.14
				NGC 1052, ISAAC/VLT (MR/LR), $R = 4700/R = 730$ ($\sigma_v \sim 60/430\,\mathrm{km\,s^{-1}}$)								
N	792^{+61}_{-51}	–	10.4	–	–	–	693^{+20}_{-20}	–	9.5	–	–	–
B	2455^{+143}_{-128}	–	40.9	–	–	–	–	–	–	–	–	–
				NGC 1365, ISAAC/VLT (MR/LR), $R = 4700/R = 730$ ($\sigma_v \sim 60/430\,\mathrm{km\,s^{-1}}$)								
N	–	–	–	–	–	–	–	–	–	787^{+8}_{-8}	–	15.7
B	1243^{+100}_{-92}	–	21.3	1363^{+67}_{-54}	–	19.3	–	–	–	1972^{+85}_{-75}	–	15.4
				NGC 2992, ISAAC/VLT (MR/LR), $R = 4700/R = 730$ ($\sigma_v \sim 60/430\,\mathrm{km\,s^{-1}}$)								
N	528^{+56}_{-58}	–	22.8	528^{+56}_{-58}	–	3.4	254^{+3}_{-8}	–	7.7	254^{+3}_{-8}	–	5.4
I	–	–	–	–	–	–	869^{+34}_{-56}	111	5.4	869^{+34}_{-56}	111	2.1
B	3186^{+586}_{-400}	–	50.9	2989^{+660}_{-488}	–	21.2	–	–	–	2056^{+29}_{-30}	–	22.2
				NGC 4395, LUCI/LBT; $R = 1360$ ($\sigma_v \sim 220\,\mathrm{km\,s^{-1}}$)								
N	348^{+5}_{-6}	–	104.1	348^{+5}_{-6}	–	16.1	235^{+7}_{-6}	–	13.2	235^{+7}_{-6}	–	16.9
I	–	–	–	–	–	–	–	–	–	–	–	
B	1350^{+93}_{-70}	–	58.7	1591^{+310}_{-245}	–	16.3	–	–	–	879^{+29}_{-34}	–	40.6
				NGC 6221, X-shooter/VLT, $R = 5300$ ($\sigma_v \sim 57\,\mathrm{km\,s^{-1}}$)								
N	141^{+1}_{-1}	–	10.7	141^{+1}_{-1}	–	8.6	141^{+1}_{-1}	–	5.9	141^{+1}_{-1}	–	18.6
I	343^{+9}_{-9}	52	21.7	343^{+9}_{-9}	213	2.0	483^{+12}_{-12}	176	10.3	483^{+12}_{-12}	176	9.5
B	2142^{+110}_{-141}	–	29.6	1433^{+70}_{-70}	–	9.2	–	–	–	2257^{+99}_{-93}	–	20.5
				NGC 7314, X-shooter/VLT, $R = 5300$ ($\sigma_v \sim 57\,\mathrm{km\,s^{-1}}$)								
N	84^{+2}_{-2}	–	11.7	84^{+2}_{-2}	–	3.3	84^{+2}_{-2}	–	1.4	84^{+2}_{-2}	–	6.4
I	361^{+10}_{-9}	55	41.0	361^{+10}_{-9}	55	5.6	392^{+13}_{-13}	42	1.4	392^{+13}_{-13}	42	13.0
B	1428^{+46}_{-38}	–	114.0	1430^{+78}_{-99}	–	50.9	–	–	–	1348^{+15}_{-15}	–	74.9

Notes. (1) Line components. B: BLR, N: NLR, I: intermediate (see Section 4 for the classification criteria); (2)–(13) FWHM [km s^{-1}] (not deconvolved for the instrumental resolution), wavelength shift of the component's centre relative to its narrow component [km s^{-1}], component's EW [Å]. The object name, the instrument used for the observations, the instrumental resolution and the corresponding velocity resolution σ_v [km s^{-1}] are also reported.
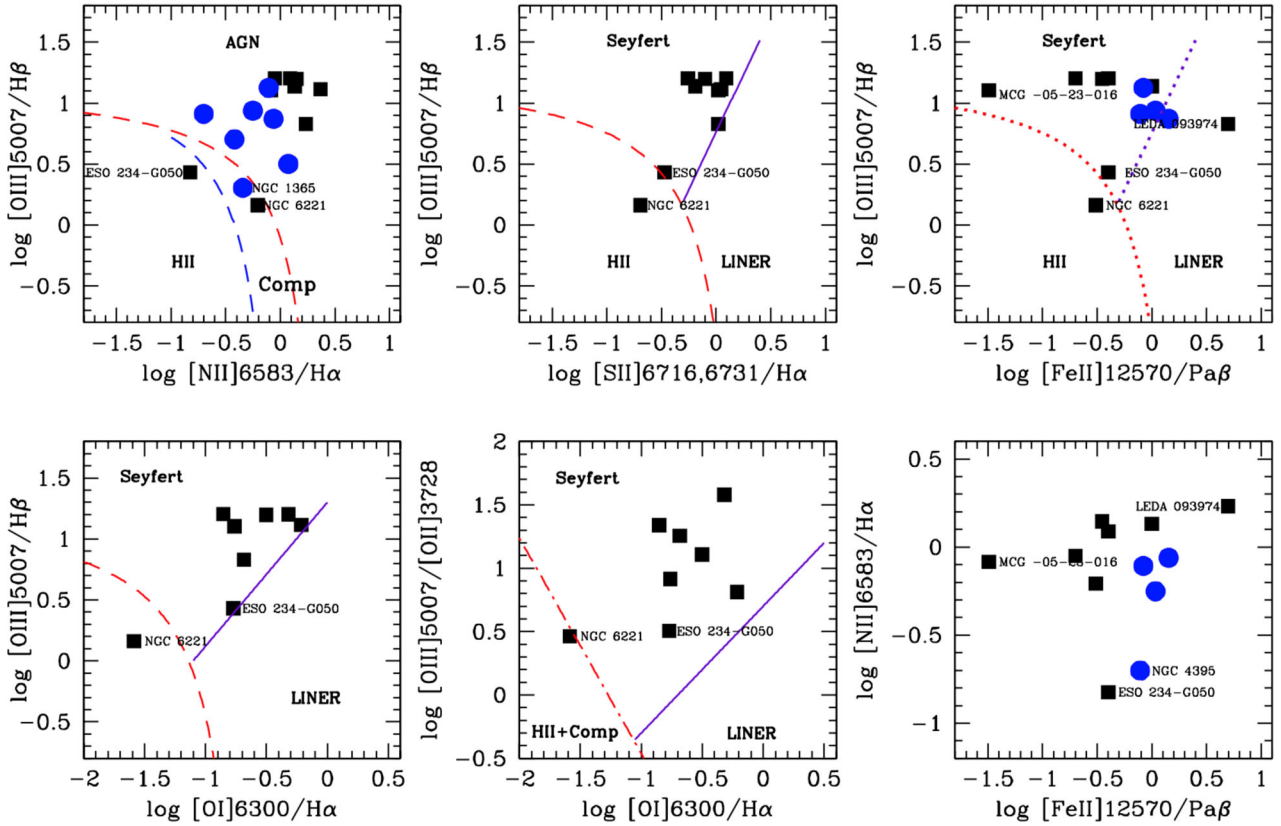
Figure 20. Line ratio diagnostic diagrams of the activity classification. The X-shooter objects are shown by black filled squares. For the ISAAC and LUCI targets (shown by blue filled circles), we show only the results for the broad AGN2 sample, which were derived using the optical spectra taken from literature. The lines used to define the activity regions are the following: extreme starbursts (red dashed; Kewley et al. 2001), pure star formation (blue dashed; Kauffmann et al. 2003), Seyfert-LINER (purple solid; Kewley et al. 2006), Seyfert-H II+Composite galaxies (red dot dashed; Kewley et al. 2006). In the [O III]5007/Hβ versus [Fe II]/Pa β diagram, as no activity region definition was available, we used as a reference those computed for the [O III]5007/Hβ versus [S II]6716,6731/Hα diagram.

Table 6. Activity classification and new spectroscopic redshifts.

Object	Redshift	*Swift*/BAT classification	Classification
(1)	(2)	(3)	(4)
2MASX J05054575−2351139	0.035	2	AGN2
2MASX J06411806+3249313	0.048	2	–
2MASX J09112999+4528060	0.0269	2	–
2MASX J11271632+1909198	0.1057	1.8	–
2MASX J18305065+0928414	0.0193	2	AGN2
3C 105	0.0884	2	–
3C 403	0.0589	2	–
CGCG 420−015	0.029	2	–
ESO 005−G004	0.006	2	–
ESO 157−G023	0.044	2	–
ESO 234−G050	0.0088	2	AGN2/Starburst
ESO 263−G013	0.0334	2	AGN2
ESO 297−G018	0.0253	2	–
ESO 374−G044	0.0284	2	AGN2
ESO 416−G002	0.059	1.9	–
ESO 417−G006	0.0163	2	–
Fairall 272	0.022	2	–
LEDA 093974	0.0239	2	AGN2
MCG−01−24−012	0.0197	2	AGN2
MCG−05−23−016	0.0084	2	AGN2
Mrk 417	0.0327	2	–
Mrk 1210	0.014	2	–

Table 6 – *continued*

Object	Redshift	*Swift*/BAT classification	Classification
(1)	(2)	(3)	(4)
NGC 612	–	2	–
NGC 788	0.0135	2	–
NGC 1052	0.0047	2	AGN2
NGC 1142	0.0294	2	–
NGC 1365	0.005	1.8	AGN2/Starburst
NGC 2992	0.0077	2	AGN2
NGC 3079	0.0036	2	–
NGC 3081	0.0077	2	–
NGC 3281	0.0113	2	–
NGC 4138	–	1.9	–
NGC 4388	0.0089	2	–
NGC 4395	0.0014	1.9	AGN2
NGC 4686	–	XBONG	–
NGC 4941	0.0038	2	AGN2
NGC 4945	0.0017	2	–
NGC 5643	0.0040	2	AGN2
NGC 6221	0.0045	2	AGN2/Starburst
NGC 7314	0.0047	1.9	AGN2
PKS 0326−288	0.1096	1.9	–

Notes. (1) Source name; (2) spectroscopic redshift (this work); (3) *Swift*/BAT classification (Baumgartner et al. 2013); (4) line ratio diagnostic classification (see Section 4.1).

Table 7. FWHM of the BLR components.

Object (Instr.) (1)	Redshift (2)	Cl (3)	Hα (4)	He I (5)	Pa β (6)
			FWHM (km s^{-1})		
2MASX J05054575−2351139 (I)	0.035	2	–	1772^{+419}_{-318}	–
2MASX J18305065+0928414 (X)	0.0193	2	2660^{+500}_{-460}	3513^{+232}_{-213}	–
ESO 234−G050 (X)	0.0088	2	971^{+124}_{-104}	1110^{+63}_{-59}	1304^{+381}_{-322}
ESO 374−G044 (I)	0.0284	2	–	1123^{+383}_{-221}	1412^{+318}_{-294}
MCG−01−24−012 (I)	0.0197	2	–	–	2069^{+300}_{-280}
MCG−05−23−016 (X)	0.0084	2	2232^{+36}_{-38}	2474^{+67}_{-64}	2133^{+93}_{-89}
Mrk 1210 (I)	0.014	2	NA	1305^{+73}_{-32}	1936^{+118}_{-225}
NGC 1052 (I)	0.0047	2	2192^{+51}_{-45}	2417^{+143}_{-128}	–
NGC 1365 (I)	0.005	1.8	1674^{+47}_{-46}	–	1971^{+85}_{-75}
NGC 2992 (I)	0.0077	2	3139^{+436}_{-354}	3157^{+586}_{-400}	2055^{+29}_{-30}
NGC 4395 (L)	0.0014	1.9	622^{+20}_{-18}	1332^{+93}_{-70}	851^{+29}_{-34}
NGC 6221 (X)	0.0045	2	1630^{+12}_{-11}	2141^{+110}_{-141}	2256^{+99}_{-82}
NGC 7314 (X)	0.0047	1.9	1328^{+4}_{-5}	1427^{+46}_{-38}	1347^{+46}_{-39}

Notes. (1) Object (Instrument used. X: X-shooter, I: ISAAC, L: LUCI); (2) Redshift as reported in Table 6; (3) AGN spectral classification according to Baumgartner et al. (2013); (4)–(6) FWHM of the BLR component deconvolved for the instrumental spectral resolution. The FWHM of the optical lines of the objects not observed with X-shooter have been obtained by analysis of spectra retrieved using the NED[a] data base.
[a]NASA/IPAC Extragalactic Database: https://ned.ipac.caltech.edu.
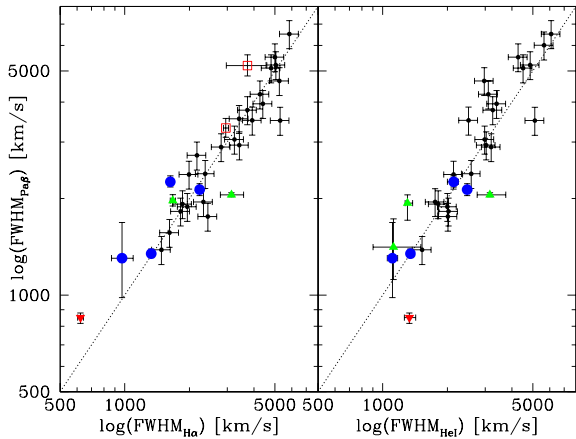
Figure 21. Left. Best-fitting FWHM of the broad components of the Pa β line as a function of the FWHM of the Hα line. The open red squares shows those two objects lacking a Pa β measurement and whose FWHM value has been replaced by the He I measurement (see the text). Right. Best-fitting FWHM of the broad components of the Pa β line as a function of the FWHM of the He I line. Blue circles: X-shooter; Green triangles: ISAAC; Red, upside down triangles: LUCI. In both panels, the black dotted line shows the 1:1 locus, while the black dots show the FWHM (corrected for instrumental broadening) distribution of a sample of AGN1 from Landt et al. (2008).

X-ray flux, X-ray luminosity, hydrogen column density N_H, and the orientation (a/b = major axis/minor axis) of the hosting galaxy (as reported in Hyperleda;[1] see Table 8; Makarov et al. 2014).

In Fig. 22, the 14–195 keV flux as a function of the 2MASS *J*-band magnitude for the 'broad' and 'non-broad' AGN2 samples is

[1] http://leda.univ-lyon1.fr/

shown: no significant difference between the two samples is found. The 'broad' AGN2 sample has an average *J*-band magnitude value (13.1±0.4) which is undistinguishable from that of the 'non-broad' AGN2 sample (13.1±0.2; see Table 8). Moreover, also the average X-ray flux ($\log F_X = 1.5±0.1 \ 10^{-12}$ erg cm^{-2} s^{-1}) is almost identical to that of the 'non-broad' AGN2 sample ($\log F_X = 1.6±0.1 \ 10^{-12}$ erg cm^{-2} s^{-1}).

In Figs 23 and 24, we show the dependence of the EW and FWHM of the BLR components as a function of the spectral S/N ratio. For each of the 13 'broad' AGN2 the values of the Pa β line, when found (10 sources), are shown, otherwise the values obtained for the He I line (three sources) are shown. Indeed, as shown in Fig. 21 and according to Landt et al. (2008), no significant difference is observed among the FWHM measurements of the Pa β and He I lines. No evidence is found of a dependence of the EW and FWHM measurements from the S/N ratio. More precisely, on the contrary of what it could be expected, it is not observed that the smallest EW were measured in the highest S/N spectra.

In Fig. 25, the S/N ratio as a function of the 14–195 keV luminosity, of the 'non-broad' and the 'broad' AGN2 samples, is shown. The 'broad' AGN2 sample has an average S/N ratio (35.8±3.5) which is undistinguishable from that of the 'non-broad' AGN2 sample (32.8 ± 2.5). None the less, it should be noticed that there is marginal (2σ) evidence for the 'broad' AGN2 sample having, on average, lower X-ray luminosities ($\log L_X = 42.7 ± 0.2$ erg s^{-1}) than the 'non-broad' AGN2 sample ($\log L_X = 43.5 ± 0.2$ erg s^{-1}). This difference could be ascribed to the intrinsic differences among the different observed samples. The 11 objects observed with X-shooter (the most efficient instrument for this project: five 'broad' AGN2 found) were chosen to be among the less luminous of the *Swift*/BAT sample.

In Fig. 26, the host galaxy axis ratio (a/b = majoraxis/minoraxis) as a function of the 14–195 keV luminosity is shown. The axis ratio has been evaluated at the isophote 25 mag arcsec^{-2} in the *B* band. No significant difference between the two samples was found. The

Table 8. Average diagnostic values of the samples.

Sample	J (mag)	$\log F_X$ (10^{-12} erg s^{-1} cm^{-2})	$\log N_H$ (cm^{-2})	$\log L_X$ erg s^{-1}	$\log(a/b)$	S/N
(1)	(2)	(3)	(4)	(5)	(6)	(7)
Non-broad AGN2	13.1 ± 0.2	1.6 ± 0.1	23.1 ± 0.2	43.5 ± 0.2	0.27 ± 0.05	32.8 ± 2.5
N. objects	29	29	29	29	26	29
Broad AGN2	13.1 ± 0.4	1.5 ± 0.1	22.8 ± 0.2	42.7 ± 0.2	0.26 ± 0.05	35.8 ± 3.5
N. objects	13	13	13	13	13	13
Broad AGN2[a]	13.6 ± 0.4	1.5 ± 0.2	22.8 ± 0.2	42.9 ± 0.3	0.30 ± 0.06	31.7 ± 3.4
N. objects	9	9	9	9	9	9

Notes. (1) Sample; (2) average J-band magnitude (from 2MASS); (3) average 14–195 keV flux (from SWIFT70M); (4) average hydrogen column density; (5) average 14–195 keV luminosity; (6) average axis ratio (a/b = majoraxis/minoraxis) at the B-band isophote 25 mag arcsec^{-2} (from Hyperleda; Makarov et al. 2014); (7) average spectral signal-to-noise ratio. The number of objects is also reported.
[a] Excluding those objects showing a substantial starburst component (NGC 1365, NGC 6221, ESO 234−G050) and the LINER galaxy NGC 1052 (see Section 4.1).
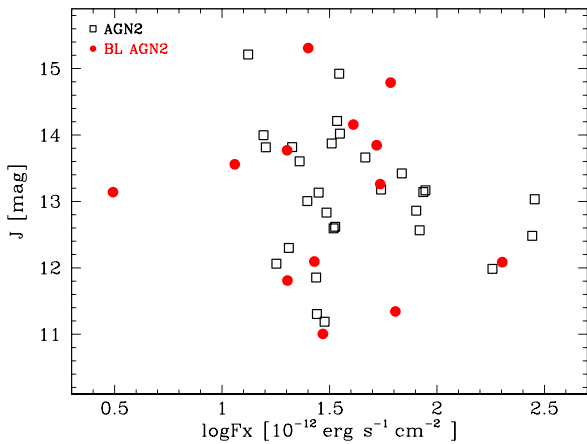
Figure 22. J-band magnitude as a function of the 14–195 keV flux of the 'non-broad' (black open squares) and the 'broad' (red filled circles) AGN2 samples.

Figure 24. FWHM of the broad components as a function of the spectral S/N ratio.

Figure 23. EWs of the broad components as a function of the spectral S/N ratio.
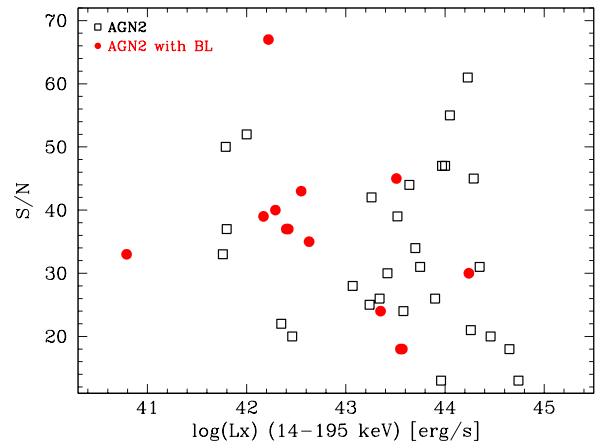
Figure 25. Spectral S/N ratio as a function of the 14–195 keV luminosity of the 'non-broad' (black open squares) and the 'broad' (red filled circles) AGN2 samples.

'broad' AGN2 sample shows an average axis ratio $\log(a/b) = 0.26 \pm 0.05$ while the 'non-broad' AGN2 sample has an average axis ratio $\log(a/b) = 0.27 \pm 0.05$.

In Fig. 27, the hydrogen column density, N_H, as a function of the 14–195 keV luminosity is shown. There is marginal (2σ) evidence that the 'broad' AGN2 have, on average, lower N_H ($\log N_H = 22.8$

± 0.2 cm^{-2}) than measured in the 'non-broad' AGN2 ($\log N_H = 23.1 \pm 0.2$ cm^{-2}). The largest column density measured in the 'broad' AGN2 sample is $\log N_H = 23.7$ cm^{-2}, while there are seven 'non-broad' AGN2 with $\log N_H > 23.7$ cm^{-2}.

Finally, Fig. 28 shows the FWHM as a function of their EW, of all line components (both broad and narrow) detected in the whole
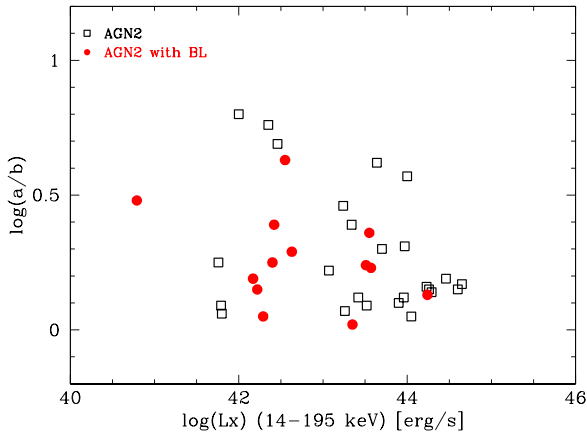
Figure 26. The axis ratio (a/b = major axis/minor axis) of the AGN2 host galaxies as a function of the 14–195 keV luminosity for the 'non-broad' AGN2 sample (black open squares) and for the 'broad' AGN2 sample (red filled circles). The axis ratio has been evaluated at the isophote 25 mag arcsec^{-2} in the *B* band (from Hyperleda; Makarov et al. 2014).
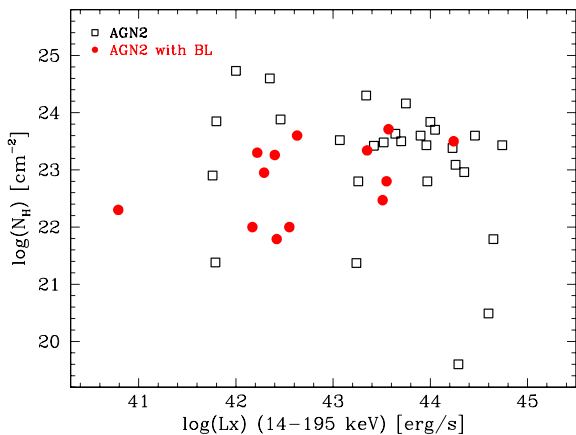
Figure 27. Hydrogen column density, N_H, as a function of the 14–195 keV luminosity of the 'non-broad' (black open squares) and the 'broad' (red filled circles) AGN2 samples.

sample of the 41 studied AGN2. For comparison, the Pa β emission line fitting values of a subsample of 24, LR, AGN1 (Landt et al. 2008), from the *Swift*/BAT 70-month catalogue, and our measurement of the AGN1 NGC 3783, are also shown. As is seen, AGN1 show, on average, larger FWHM and EW than the AGN2. In particular, AGN1 have an average FWHM = $3350 \pm 310 \, \text{km s}^{-1}$ and an average EW = 80 ± 7 Å, while AGN2 have an average FWHM = $1680 \pm 610 \, \text{km s}^{-1}$ and an average EW = 39 ± 8 Å. It should be noticed that, as expected from the AGN X-ray luminosity function (see introduction; the samples come from a hard X-ray flux limited survey), AGN1 are, on average, about one dex more luminous than AGN2: $\log L_X = 44.0 \pm 0.9 \, \text{erg s}^{-1}$ and $\log L_X = 42.9 \pm 1.0 \, \text{erg s}^{-1}$, respectively. The detection limits for our observations in the EW-FWHM plane (black solid line in Fig. 28) has been derived through simulations with our spectra on the detection of emission lines having different EWs and FWHMs. According to this analysis, the observed difference on the FWHM and EW measurements among the AGN1 and AGN2 samples is not due to selection biases, as FWHM and EW values as large as measured in the AGN1 population could have been easily detected also in the AGN2 sample, if present.

We have also tested whether the results of the above described analyses would change if those AGN2 having relevant starburst or

LINER component in their spectra (see Section 4.1) were excluded. As is shown in Table 8 no difference was found.

6 CONCLUSIONS

Thanks to NIR spectroscopy with LUCI/LBT, ISAAC/VLT and X-shooter/VLT, we have been able to detect faint BLR components in 13 out of 41 AGN2 drawn from the *Swift*/BAT 70-month catalogue.

The sample of AGN2 where the BLR components have been found does not show significant differences in spectral S/N ratio, X-ray fluxes and galaxy orientation, from the rest of the AGN2. The possibility can therefore be excluded that relevant selection effects affect the AGN2 sample where the BLR lines have been detected.

The only significant differences are instead physical: (a) no BLR was found in the most [heavily, $\log(N_H) > 23.7 \, \text{cm}^{-2}$] X-ray obscured sources and (b) AGN2 show smaller FWHMs and EWs if compared to AGN1. The first result most likely implies that, as expected by the AGN unification models, the absence of the BLR in the optical and NIR spectra is linked to the presence of strong obscuration of the central parts of the AGN, where the BLR is located. As far as the second result is concerned, according to the virial methods, where the BH mass depends on the square of the BLR FWHM (and on the square root of the luminosity), smaller broad line region FWHM (and luminosity) values of the AGN2, if compared to the AGN1 population, imply that AGN2 have smaller BH masses than AGN1. The study of the differences on the BH mass distributions, Eddington ratios, and host galaxy properties of the AGN1 and AGN2 populations is beyond the scope of this work and will be discussed in following papers (Onori et al., in preparation; Ricci et al., in preparation).

Figure 28. FWHM of the most relevant line components of all 42 AGN analyzed in this work as a function of their EW. The broad AGN2 components are shown by red filled circles, squares and triangles for the Pa β, He I and Pa γ lines, respectively. Broad Pa β measurements of a control subsample of AGN1 (Landt et al. 2008), from the *Swift*/BAT 70-month catalogue, are shown by filled blue circles. Other narrow components are in black as explained in the legend. The black solid line shows the lower detection limit for the Pa β emission line, according to the average S/N ratio and spectral resolution of the observations.

REFERENCES

Aguero E. L., 1993, The Observatory, 113, 301
Ajello M., Alexander D. M., Greiner J., Madejski G. M., Gehrels N., Burlon D., 2012, ApJ, 749, 21
Allevato V. et al., 2014, ApJ, 796, 4
Antonucci R., 1993, ARA&A, 31, 473
Arnaud K. A., 1996, in Jacoby G. H., Barnes J., eds, ASP Conf. Ser. Vol. 101, Astronomical Data Analysis Software and Systems V. Astron. Soc. Pac., San Francisco, p. 17
Baldwin J. A., Phillips M. M., Terlevich R., 1981, PASP, 93, 5
Barth A. J., Filippenko A. V., Moran E. C., 1999, ApJ, 515, L61
Baumgartner W. H., Tueller J., Markwardt C. B., Skinner G. K., Barthelmy S., Mushotzky R. F., Evans P. A., Gehrels N., 2013, ApJS, 207, 19
Beckmann V., Gehrels N., Shrader C. R., Soldi S., 2006, ApJ, 638, 642
Blandford R. D., McKee C. F., 1982, ApJ, 255, 419
Bongiorno A. et al., 2014, MNRAS, 443, 2077
Burlon D., Ajello M., Greiner J., Comastri A., Merloni A., Gehrels N., 2011, ApJ, 728, 58
Cai H.-B., Shu X.-W., Zheng Z.-Y., Wang J.-X., 2010, Res. Astron. Astrophys., 10, 427
Civano F. et al., 2007, A&A, 476, 1223
Claussen M. J., Diamond P. J., Braatz J. A., Wilson A. S., Henkel C., 1998, ApJ, 500, L129
Comastri A. et al., 2002, ApJ, 571, 771
de Vaucouleurs G., de Vaucouleurs A., Corwin H. G., Jr, Buta R. J., Paturel G., Fouqué P., 1991, Third Reference Catalogue of Bright Galaxies. Volume I: Explanations and references. Volume II: Data for galaxies between 0^h and 12^h. Volume III: Data for galaxies between 12^h and 24^h. Springer, New York, NY

Dewangan G. C., Griffiths R. E., 2005, ApJ, 625, L31
DiPompeo M. A., Hickox R. C., Myers A. D., 2016, MNRAS, 456, 924
Dopita M. A. et al., 2015, ApJS, 217, 12
Ebrero J., Costantini E., Kaastra J. S., de Marco B., Dadina M., 2011, A&A, 535, A62
Eguchi S., Ueda Y., Terashima Y., Mushotzky R., Tueller J., 2009, ApJ, 696, 1657
Elitzur M., 2012, ApJ, 747, L33
Filippenko A. V., Sargent W. L. W., 1989, ApJ, 342, L11
Freudling W., Romaniello M., Bramich D. M., Ballester P., Forchi V., García-Dabló C. E., Moehler S., Neeser M. J., 2013, A&A, 559, A96
Gilli R., Maiolino R., Marconi A., Risaliti G., Dadina M., Weaver K. A., Colbert E. J. M., 2000, A&A, 355, 485
Glass I. S., 1997, MNRAS, 292, L50
González-Martín O., Díaz-González D., Acosta-Pulido J. A., Masegosa J., Papadakis I. E., Rodríguez-Espinosa J. M., Márquez I., Hernández-García L., 2014, A&A, 567, A92
Goodrich R. W., Veilleux S., Hill G. J., 1994, ApJ, 422, 521
Graham A. W., 2008, ApJ, 680, 143
Greene J. E., Ho L. C., 2007, ApJ, 670, 92
Guainazzi M., Oosterbroek T., Antonelli L. A., Matt G., 2000, A&A, 364, L80
Guainazzi M., Matt G., Fiore F., Perola G. C., 2002, A&A, 388, 787
Guainazzi M., Rodriguez-Pascual P., Fabian A. C., Iwasawa K., Matt G., 2004, MNRAS, 355, 297
Heckman T. M., Kauffmann G., Brinchmann J., Charlot S., Tremonti C., White S. D. M., 2004, ApJ, 613, 109
Heisler C. A., De Robertis M. M., 1999, AJ, 118, 2038
Hernández-García L., González-Martín O., Márquez I., Masegosa J., 2013, A&A, 556, A47

Hernández-García L., Masegosa J., González-Martín O., Márquez I., 2015, A&A, 579, A90

Ho L. C., Kim M., 2015, ApJ, 809, 123

Ho L. C., Filippenko A. V., Sargent W. L., 1995, ApJS, 98, 477

Ho L. C., Filippenko A. V., Sargent W. L. W., 1997, ApJ, 487, 568

Horne K., 1986, PASP, 98, 609

Ichikawa K., Ueda Y., Terashima Y., Oyabu S., Gandhi P., Matsuta K., Nakagawa T., 2012, ApJ, 754, 45

Jiang N., Wang H., Mo H., Dong X., Wang T., Zhou H., 2016, preprint (arXiv:1602.08825)

Jones D. H. et al., 2009, MNRAS, 399, 683

Kauffmann G. et al., 2003, MNRAS, 346, 1055

Kellermann K. I., Vermeulen R. C., Zensus J. A., Cohen M. H., 1998, AJ, 115, 1295

Kelly B. C., Vestergaard M., Fan X., 2009, ApJ, 692, 1388

Kelly B. C., Vestergaard M., Fan X., Hopkins P., Hernquist L., Siemiginowska A., 2010, ApJ, 719, 1315

Kewley L. J., Heisler C. A., Dopita M. A., Lumsden S., 2001, ApJS, 132, 37

Kewley L. J., Groves B., Kauffmann G., Heckman T., 2006, MNRAS, 372, 961

Koribalski B., Dickey J. M., 2004, MNRAS, 348, 1255

Kormendy J., Bender R., Cornell M. E., 2011, Nature, 469, 374

La Franca F. et al., 2005, ApJ, 635, 864

La Franca F. et al., 2015, MNRAS, 449, 1526

La Franca F., Onori F., Ricci F., Bianchi S., Marconi A., Sani E., Vignali C., 2016, Frontiers in Astronomy and Space Sciences, 3, 12

Landt H., Bentz M. C., Ward M. J., Elvis M., Peterson B. M., Korista K. T., Karovska M., 2008, ApJS, 174, 282

Lawrence A., Elvis M., 1982, ApJ, 256, 410

Levenson N. A., Cid Fernandes R., Jr, Weaver K. A., Heckman T. M., Storchi-Bergmann T., 2001, ApJ, 557, 54

Lumsden S. L., Alexander D. M., Hough J. H., 2004, MNRAS, 348, 1451

Lusso E. et al., 2012, MNRAS, 425, 623

McLure R. J., Dunlop J. S., 2001, MNRAS, 327, 199

Maiolino R., Rieke G. H., Rieke M. J., 1996, AJ, 111, 537

Makarov D., Prugniel P., Terekhova N., Courtois H., Vauglin I., 2014, A&A, 570, A13

Malizia A., Malaguti G., Bassani L., Cappi M., Comastri A., Di Cocco G., Palazzi E., Vignali C., 2002, A&A, 394, 801

Marinucci A., Bianchi S., Nicastro F., Matt G., Goulding A. D., 2012, ApJ, 748, 130

Marshall F. E., Boldt E. A., Holt S. S., Mushotzky R. F., Rothschild R. E., Serlemitsos P. J., Pravdo S. H., 1979, ApJS, 40, 657

Masetti N. et al., 2010, A&A, 519, A96

Mazzalay X., Rodríguez-Ardila A., 2007, A&A, 463, 445

Merloni A. et al., 2010, ApJ, 708, 137

Molina M., Bassani L., Malizia A., Stephen J. B., Bird A. J., Bazzano A., Ubertini P., 2013, MNRAS, 433, 1687

Moorwood A. et al., 1998, The Messenger, 94, 7

Mould J. et al., 2012, ApJS, 203, 14

Osterbrock D. E., Ferland G. J., 2006, Astrophysics of Gaseous Nebulae and Active Galactic Nuclei. University Science Books, Mill Valley, CA

Parisi P. et al., 2009, A&A, 507, 1345

Parisi P. et al., 2012, A&A, 545, A101

Peterson B. M., 1993, PASP, 105, 247

Piccinotti G., Mushotzky R. F., Boldt E. A., Holt S. S., Marshall F. E., Serlemitsos P. J., Shafer R. A., 1982, ApJ, 253, 485

Reeves J. N. et al., 2007, PASJ, 59, 301

Ricci C., Ueda Y., Paltani S., Ichikawa K., Gandhi P., Awaki H., 2014, MNRAS, 441, 3622

Riffel R., Rodríguez-Ardila A., Pastoriza M. G., 2006, A&A, 457, 61

Risaliti G., Bianchi S., Matt G., Baldi A., Elvis M., Fabbiano G., Zezas A., 2005, ApJ, 630, L129

Risaliti G., Elvis M., Fabbiano G., Baldi A., Zezas A., Salvati M., 2007, ApJ, 659, L111

Risaliti G. et al., 2009, ApJ, 705, L1

Risaliti G. et al., 2013, Nature, 494, 449

Satyapal S., Dudik R. P., O'Halloran B., Gliozzi M., 2005, ApJ, 633, 86

Schmitt H. R., Donley J. L., Antonucci R. R. J., Hutchings J. B., Kinney A. L., 2003, ApJS, 148, 327

Schulz H., Komossa S., Schmitz C., Mücke A., 1999, A&A, 346, 764

Schulze A. et al., 2015, MNRAS, 447, 2085

Seifert W. et al., 2003, in Iye M., Moorwood A. F. M., eds, Proc. SPIE Conf. Ser. Vol. 4841, Instrument Design and Performance for Optical/Infrared Ground-Based Telescopes. SPIE, Bellingham, p. 962

Storchi-Bergmann T., Kinney A. L., Challis P., 1995, ApJS, 98, 103

Storchi-Bergmann T., Fernandes R. C., Schmitt H. R., 1998, ApJ, 501, 94

Tody D., 1986, in Crawford D.L., ed., Proc. SPIE Conf. Ser. Vol. 627, Instrumentation in Astronomy VI. SPIE, Bellingham, p. 733

Torrealba J., Chavushyan V., Cruz-González I., Arshakian T. G., Bertone E., Rosa-González D., 2012, Rev. Mex. Astron. Astrofis., 48, 9

Tran H. D., 1995, ApJ, 440, 565

Tran H. D., Miller J. S., Kay L. E., 1992, ApJ, 397, 452

Trippe M. L., Crenshaw D. M., Deo R., Dietrich M., 2008, AJ, 135, 2048

Trippe M. L., Crenshaw D. M., Deo R. P., Dietrich M., Kraemer S. B., Rafter S. E., Turner T. J., 2010, ApJ, 725, 1749

Tueller J., Mushotzky R. F., Barthelmy S., Cannizzo J. K., Gehrels N., Markwardt C. B., Skinner G. K., Winter L. M., 2008, ApJ, 681, 113

Ueda Y., Akiyama M., Ohta K., Miyaji T., 2003, ApJ, 598, 886

Ueda Y., Akiyama M., Hasinger G., Miyaji T., Watson M. G., 2014, ApJ, 786, 104

Vacca W. D., Cushing M. C., Rayner J. T., 2003, PASP, 115, 389

Vasudevan R. V., Fabian A. C., Mushotzky R. F., Meléndez M., Winter L. M., Trippe M. L., 2013a, MNRAS, 431, 3127

Vasudevan R. V., Brandt W. N., Mushotzky R. F., Winter L. M., Baumgartner W. H., Shimizu T. T., Schneider D. P., Nousek J., 2013b, ApJ, 763, 111

Veilleux S., Goodrich R. W., Hill G. J., 1997, ApJ, 477, 631

Vermeulen R. C., Ros E., Kellermann K. I., Cohen M. H., Zensus J. A., van Langevelde H. J., 2003, A&A, 401, 113

Vernet J. et al., 2011, A&A, 536, A105

Veron P., Lindblad P. O., Zuiderwijk E. J., Veron M. P., Adam G., 1980, A&A, 87, 245

Veron M. P., Veron P., Zuiderwijk E. J., 1981, A&A, 98, 34

Véron-Cetty M.-P., Véron P., 2006, A&A, 455, 773

Véron-Cetty M.-P., Véron P., 2010, A&A, 518, A10

Vestergaard M., 2002, ApJ, 571, 733

Ward M., Penston M. V., Blades J. C., Turtle A. J., 1980, MNRAS, 193, 563

Winter L. M., Lewis K. T., Koss M., Veilleux S., Keeney B., Mushotzky R. F., 2010, ApJ, 710, 503

Zoghbi A., Reynolds C., Cackett E. M., Miniutti G., Kara E., Fabian A. C., 2013, ApJ, 767, 121

SUPPORTING INFORMATION

Supplementary data are available at *MNRAS* online.

ascii format of the tables in appendix and the spectra in ascii format

Please note: Oxford University Press is not responsible for the content or functionality of any supporting materials supplied by the authors. Any queries (other than missing material) should be directed to the corresponding author for the article.

APPENDIX A: COMMENTS ON THE BLR BEST-FITTING MODELS

NGC 4395

NGC 4395 is a nearby, small bulgeless (Sd) galaxy, known to host one of the smallest super massive BH (10^4–10^5 $M_\odot$) ever found. Filippenko & Sargent (1989) classified the nucleus of NGC 4395 as a type 1.8 or type 1.9 Seyfert using the relative intensities of the narrow and broad components. On the basis of the appearance of the Balmer lines, Véron-Cetty & Véron (2006) classified it as a type 1.8 Seyfert.

Figure A1. Left: best fit of the He I and Pa γ lines of 2MASX J0505−2351 including the broad (FWHM = 1736 km s^{-1}) He I component. Right: same as before without including the broad He I component. Lower panels show the data to model ratio.

The best fit of the most relevant emission lines of NGC 4395 are shown in Fig. 7. In the optical spectrum, besides the narrow and broad components, evidence was found of intermediate components in the [O III] and [N II] lines which are blueshifted of 259 and 291 km s^{-1}, respectively. In the *J*-band spectrum, it was not necessary or possible to include a similar intermediate component due to the lower velocity resolution of LUCI ($\Delta v \sim 220$ km s^{-1}).

2MASX J05054575−2351139

2MASX J05054575−2351139 is a nearby galaxy hosting a Seyfert 2 nucleus. The optical spectrum analysed by Parisi et al. (2009) shows very narrow Hα and Hβ emission lines, confirming the Seyfert 2 classification. In the X-ray band, using *XMM* data, Vasudevan et al. (2013a) found a complex X-ray spectrum indicating a partially covered absorption. The authors also suggested only moderate variations in the intrinsic luminosity and in the column density. Moreover, Ricci et al. (2014) reported the detection of Fe K α emission in *Suzaku* data.

The best fit of the most relevant emission lines of 2MASX J05054575−2351139 are shown in Fig. 8. The ISAAC *J*-band LR spectrum shows an intense He I line, well separated from a faint Pa γ line. The Pa β and [Fe II] 12 570 Å lines have been also observed in MR mode. The Pa β line shows a narrow component with FWHM = 145^{+30}_{-26} km s^{-1} and a wider intermediate component with FWHM = 405^{+67}_{-49} km s^{-1}. In contrast, the [Fe II] 12 570 Å line can be modelled only by a single intermediate component with FWHM = 413^{+40}_{-38} km s^{-1} (compatible with the width of the intermediate component of the Pa β line). A narrow component of FWHM = 337 km s^{-1}was also added to take into account for the [Fe II] 12 791 Å blending to the Pa β. The He I line shows a narrow component having FWHM = 507^{+49}_{-40} km s^{-1}(FWHM $\sim$ 269 km s^{-1}if the instrumental resolution is deconvolved) and a broad component having FWHM = 1823^{+419}_{-318} km s^{-1}(FWHM $\sim$ 1772 km s^{-1} if the instrumental reso-

lution is deconvolved). The need of adding a broad He I component can be seen in Fig. A1 where the fits with residuals, with or without the broad He I component, are shown. The Pa γ line shows only a single narrow component. We have also analysed the 6dF optical spectrum of 2MASX J05054575−2351139, having a spectral resolution $R = 1000$ (Jones et al. 2009). All the lines show only a narrow component (<400 km s^{-1} if the instrumental resolution is subtracted).

In summary, we found a broad component only in the LR He I line, having FWHM $\sim$ 1820 km s^{-1}, while, although the Pa β line has been observed with a higher resolution (in the MR mode), it shows no signs of a broad component. Nevertheless both the Hα+[N II] and Hβ+[O III] are well represented only by single components, all having FWHM in the range 413–466 km s^{-1}, in agreement with what was found in the optical by Parisi et al. (2009). As the broad He I component is significantly larger than the other components, it can be attributed to the BLR.

ESO 374−G044

ESO 374−G044 is a nearby SBa galaxy in the Antlia galaxy cluster hosting a Seyfert 2 nucleus (Véron-Cetty & Véron 2010).

The best fit of the most relevant emission lines of ESO 374−G044 are shown in Fig. 9. The MR spectrum in the region of the Pa β line has been fitted by three components: the narrow (FWHM = 450 km s^{-1}) Pa β, the broad (1413 km s^{-1}) Pa β and an intermediate (FWHM = 652 km s^{-1}) [Fe II] 12570 Å. The LR spectrum of the He I region has been fitted by three components: the narrow (FWHM = 632 km s^{-1}; 463 km s^{-1}if deconvolved for the instrumental resolution) and broad (1202 km s^{-1}; 1122 km s^{-1} if deconvolved for the instrumental resolution) He I and the narrow Pa γ. The optical spectrum does not show evidence of broad (or intermediate) line components, confirming the Seyfert 2 optical classification of Véron-Cetty & Véron (2010). The need for the broad Pa β component can be seen in Fig. A2, where the fits with residuals, including
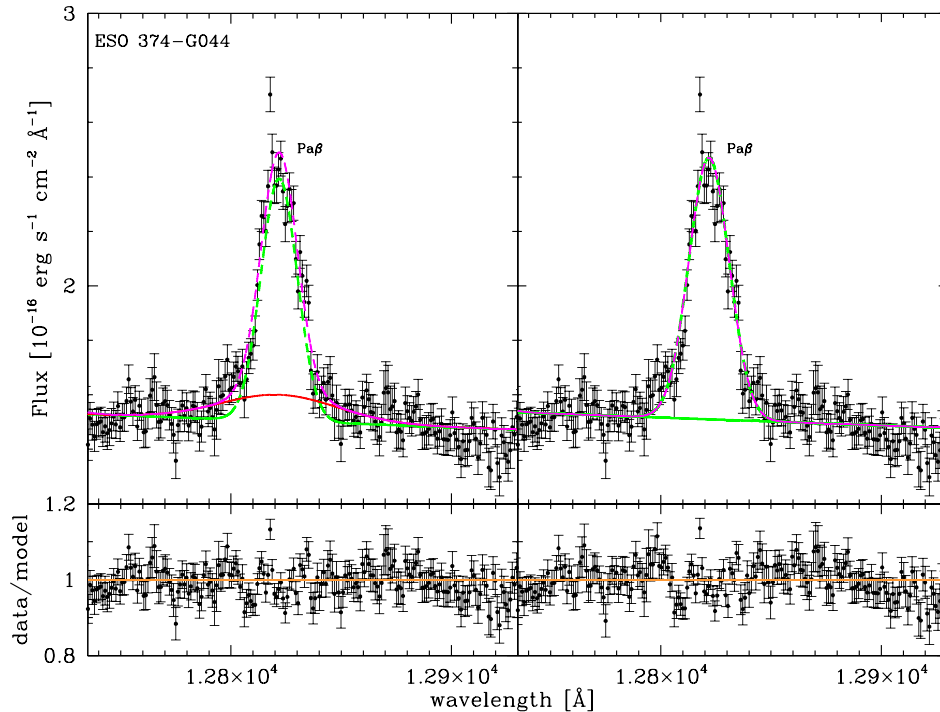
Figure A2. Left: best fit of the Pa β lines of ESO 374−G044 including a broad (FWHM = 1413 km s^{-1}) Pa β component. Right: same as before without including the broad Pa β component. Lower panels show the data to model ratio.

or not the broad Pa β component, are shown. The F test gives a probability of 0.06/0.01 that the improvement obtained with the inclusion of a broad Pa β component is due to statistical fluctuations. We therefore conclude that the presence of these faint broad components in both He I and Pa β lines should not be ignored.

MCG−01 − 24 −012

MCG−01−24−012 is a nearby spiral galaxy hosting a Compton-thin ($N_H \sim 7 \times 10^{22}$ cm^{-2}) Seyfert 2 nucleus (Véron-Cetty & Véron 2006). It was detected in the hard X-rays by Malizia et al. (2002) with *Beppo* SAX/PDS observations, and it was identified as the counterpart of the X-ray source H0917−074, detected by Piccinotti et al. (1982). Interestingly, the X-ray spectrum shows the presence of a Fe K α emission line and an absorption feature at ∼8.7 keV which cannot be explained with the presence of a warm absorber. From *HST* images, Schmitt et al. (2003) found a resolved emission in the [O III] which was explained as an extended (1.15 arcsec × 2.3 arcsec; 460 pc × 910 pc) NLR with the major axis along PA = 75°. From WiFeS observation, Dopita et al. (2015) traced further the extended NLR out to 3.7 × 2.5 kpc and found a faint ring of H II regions of about 3 kpc in radius surrounding the NLR.

The best fit of the most relevant emission lines of MCG−01−24−012 is shown in Fig. 10. The 6dF optical spectrum ($R = 1000$; Jones et al. 2009) shows evidence of intermediate components having a blueshift of $\Delta v = 189$ km s^{-1} in the [O III] lines and of $\Delta v = 111$ km s^{-1} in the [N II]+Hα lines with respect to the NLR components. Similarly, in the NIR spectrum an intermediate component having a blueshift of $\Delta v = 806$ km s^{-1} is present in the LR He I and Pa γ lines and in the MR Pa β line. Moreover the inclusion of a broad (FWHM = 2070 km s^{-1}) Pa β component is necessary. In Fig. A3, the fit with and without the inclusion of this broad Pa β component is shown. The F test gives

a probability of 2×10^{-15} that the improvement of the fit obtained with the inclusion of a broad Pa β component is due to statistical fluctuations.

MCG−05−23−016

MCG−05−23−016 is a nearby X-ray bright S0 galaxy, optically classified as a Seyfert 1.9 (Veron et al. 1980). Moreover, clear evidence was found for a broad Hα in the polarized flux (Lumsden, Alexander & Hough 2004). Its X-ray spectrum resembles a classical Compton-thin Seyfert 2 galaxy and it shows both narrow and broad components in the iron K α line (Reeves et al. 2007).

The best fit of the most relevant emission lines of MCG−05−23−016 is shown in Fig. 11. In the X-shooter optical spectrum, beside the narrow component, a clear evidence was found for an Hα BLR component with FWHM = 2232 km s^{-1}, while no evidence for a BLR component in Hβ was found. Furthermore, both the ISAAC and X-shooter NIR spectra show clear evidence for a BLR component in the Pa β and in the He I (FWHM = 2134 km s^{-1} and FWHM = 2474 km s^{-1}, respectively).

Mrk 1210

Mrk 1210 is a nearby Sa galaxy, hosting a Seyfert 2 nucleus (Véron-Cetty & Véron 2010). The spectral energy distribution peaking near 60 μm made it a member of the sample of the so-called 60 μm peakers galaxies (60PKs; Heisler & De Robertis 1999). In the optical, Storchi-Bergmann, Fernandes & Schmitt (1998) found Wolf–Rayet features in the central 200 pc of the galaxy, indicating the presence of a circumnuclear starburst. Moreover, broad Hα and Hβ components (FWHM ∼ 2400 km s^{-1}) were detected in the polarized light (Tran, Miller & Kay 1992; Tran 1995). Near-infrared spectra reported by Veilleux et al. (1997) show a Pa β profile characterized by a strong narrow component on top of a
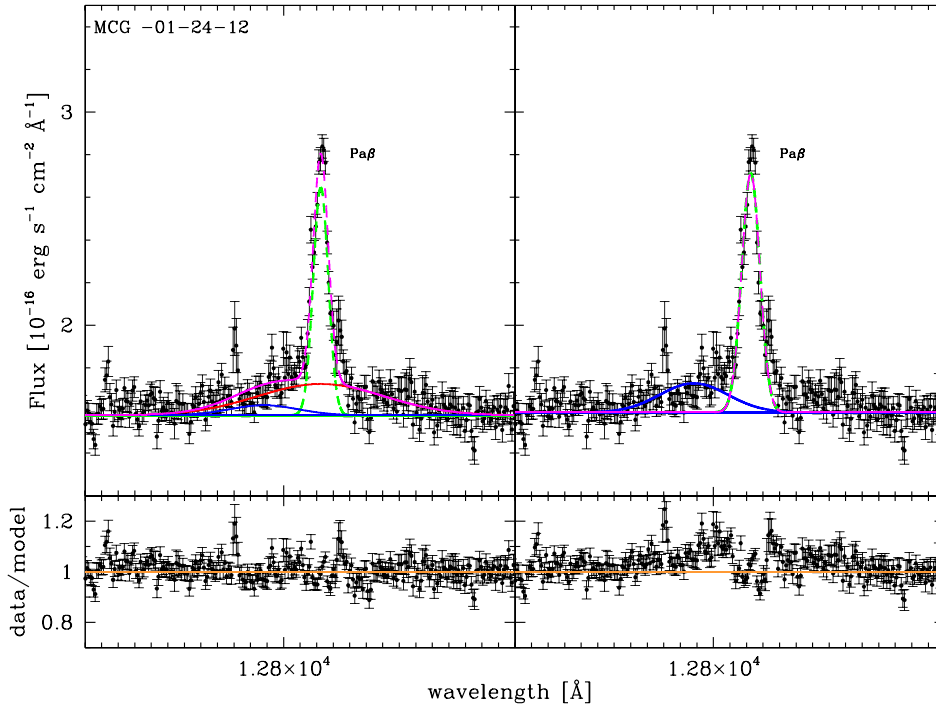
Figure A3. Left: best fit of the Pa β lines of MCG$-01-24-012$ including a broad (FWHM $= 2070$ km s^{-1}) Pa β component. Right: same as before without including the broad Pa β component. Lower panels show the data to model ratio.

broad base with FWHM ~ 1600 km s^{-1}, suggesting the presence of a hidden broad line region. However, Mazzalay & Rodríguez-Ardila (2007) found broad components of similar shape both in permitted (Hβ and Pa β) and in forbidden ([O III] and [Fe II]) emission lines, suggesting that the broad permitted component is not produced in a genuine high-density BLR. In the X-ray band, Mrk 1210 is one of the very few cases of an AGN in transition between a Compton-thick, reflection dominated state, and a Compton-thin state. This transition could be attributed to a clumpy structure in the torus (Guainazzi et al. 2002).

The ISAAC LR spectrum of Mrk 1210 shows an intense He I line, well separated from the Pa γ line. The region of the Pa β+[Fe II] 12 570 Å lines has been observed in MR mode. In this region, we have found six components: the Pa β narrow, broad and intermediate components, the [Fe II] 12 570 Å narrow and intermediate components and the [Fe II] 12 791 Å narrow component in blend with the Pa β line. The narrow components have an FWHM $= 414^{+18}_{-18}$ km s^{-1}, while the intermediate components have an FWHM $= 902^{+114}_{-61}$ km s^{-1} and show a blueshift of 136 km s^{-1} with respect to its narrow line components. The broad Pa β line has an FWHM $= 1937^{+118}_{-225}$ km s^{-1}. In Fig. A4, the fits with and without the inclusion of the broad Pa β component are shown. The F test gives a probability of 1×10^{-24} that the improvement of the fit is due to statistical fluctuations.

In summary, we found evidence for a broad component in the Pa β, having FWHM ~ 1900 km s^{-1}, that can be attributed to the BLR emission. This finding is also supported by the detection of broad Hα and Hβ in polarized light, indicating the presence of a hidden broad line region. Furthermore, the detection of a blueshifted intermediate component both in the [Fe II] and in the Pa β could be attributed to the presence of outflows in the NLR which are compatible to the observations of the [O III] and [Fe II] line profiles by Mazzalay & Rodríguez-Ardila (2007).

NGC 1052

NGC1052 is morphologically classified as an elliptical (E4) galaxy and it is the brightest member of the Cetus I cluster. It has long been considered one of the prototypical LINERs and, after the detection of a faint broad component in the Hα, it was classified as a LINER1.9 by Ho, Filippenko & Sargent (1997). Moreover, a broad component in the Hα emission line (FWHM ~ 2100 km s^{-1}) was detected also in polarization by Barth, Filippenko & Moran (1999). Furthermore, Mould et al. (2012) presented an NIR spectrum of NGC 1052, with prominent Pa β and [Fe II] emission lines. NGC 1052 shows H$_2$O megamaser emission (Claussen et al. 1998) and variability in radio and X-rays (Vermeulen et al. 2003; Hernández-García et al. 2013). Radio observations of NGC 1052 revealed a double sided jet emerging from the nucleus (Kellermann et al. 1998). The X-ray spectrum is flat with a high absorbing column density (Guainazzi et al. 2000) and there is a clear indication for the presence of an unresolved nuclear source in the hard bands (Satyapal et al. 2005). González-Martín et al. (2014) suggested that this object might be more similar to a Seyfert than to a LINER galaxy, from the X-ray point of view.

The optical spectrum of NGC 1052 was taken with The Faint Object Spectrograph/*HST*, and has a spectral resolution $R = 2800$, corresponding to a $\sigma_v \sim 80$ km s^{-1} (Torrealba et al. 2012). All the typical narrow [O III] and [N II] lines are fairly well modelled by single components having an FWHM of 1091 km s^{-1} and 682 km s^{-1}, respectively. These FWHM values are larger than observed in the typical narrow lines (see Section 3), possibly due to the presence of unresolved outflow components. The Hα shows a broad component of FWHM $= 2193$ km s^{-1}, in agreement with previous observations. The ISAAC LR spectrum shows an intense He I with evidence of a broad component having an FWHM of 2455 km s^{-1} (FWHM $= 2417$ km s^{-1} if the instrumental resolution is subtracted). We attributed this detection to the BLR emission. Finally we
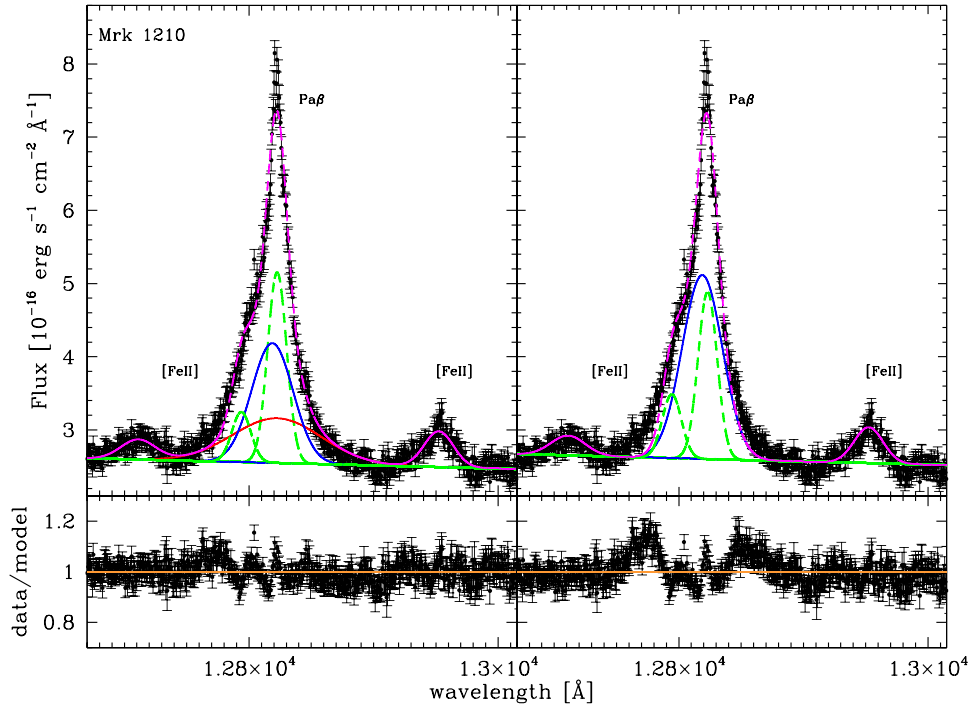
Figure A4. Left: best fit of the Pa β lines of Mrk 1210 including a broad (FWHM = 2019 km s^{-1}) Pa β component. Right: same as before without including a broad Pa β component. Lower panels show the data to model ratio.
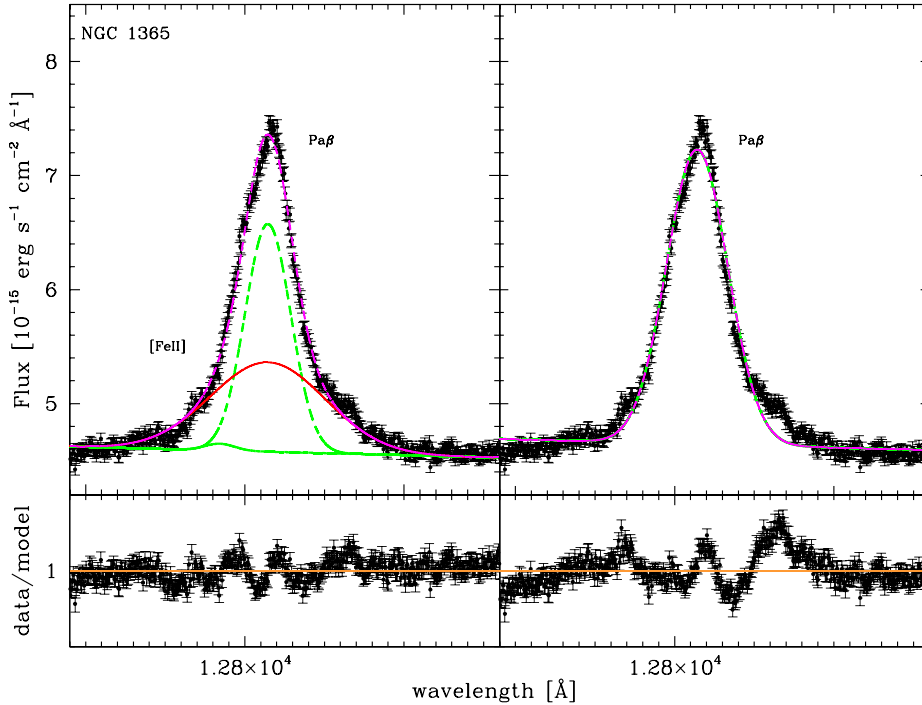
Figure A5. Left: Best fit of the Pa β lines of NGC 1365 including a broad (FWHM = 1791 km s^{-1}) Pa β component. Right: same as before without including a broad Pa β component. Lower panels show the data to model ratio.

notice that, although the [Fe II] 12 570 Å is quite intense, there is no evidence for the Pa γ and Pa β emission lines (even in the MR observations), in contrast with what was found by Mould et al. (2012).

NGC 1365

NGC 1365 is a SB galaxy hosting a Seyfert 1.9 nucleus (Trippe et al. 2010). It displays strong X-ray variability (on time-scales of hours to years) and evidence for a relativistically broadened iron
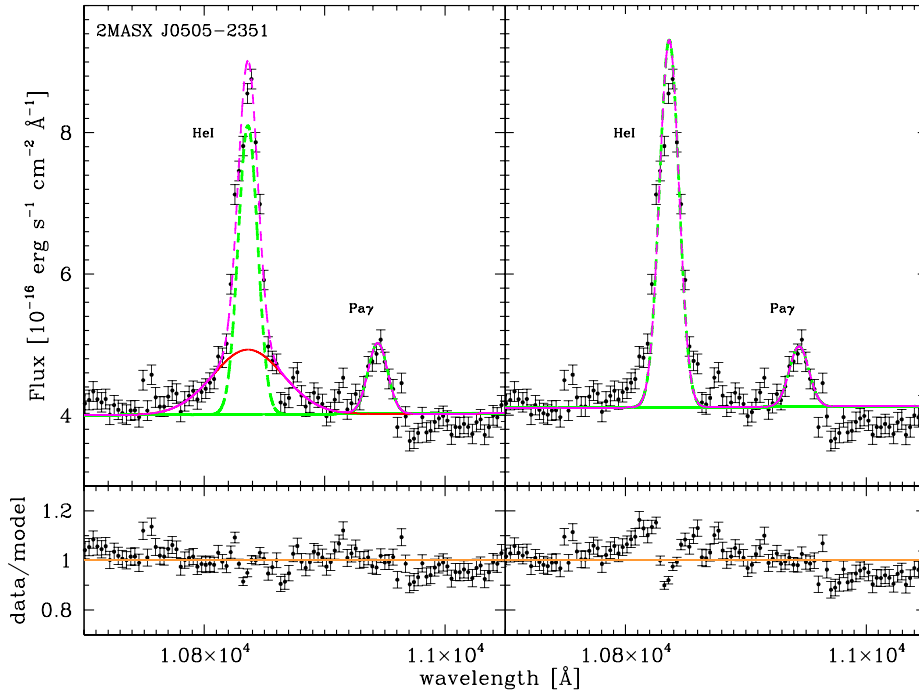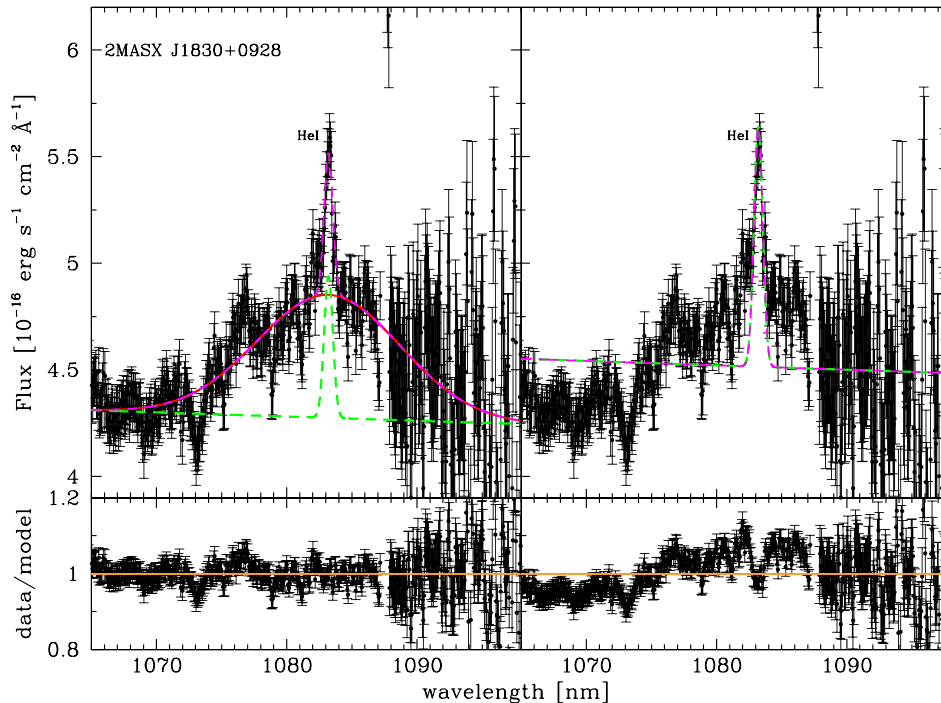
Figure A6. Left: best fit of the He I line of 2MASX J18305065+0928414 including a broad (FWHM = 3513 km s^{-1}) He I component. Right: same as before without including a broad He I component. Lower panels show the data to model ratio.

line, indicative of a rapidly rotating BH (Risaliti et al. 2009; Risaliti et al. 2013). Furthermore, it displayed a complex and variable absorption, with rapid variations in column density, attributed to an occultation event originating in the BLR clouds (Risaliti et al. 2005, 2007). In the optical spectra of NGC 1365 there is some evidence of variability. Veron et al. (1980) classified it as a Seyfert 1.5 on the basis of a strong Hα detected in the nucleus. Moreover, Schulz et al. (1999) detected a broad component in Hβ with an FWHM ∼ 1900 km s^{-1}. However, Trippe et al. (2010) found an extremely faint component in Hα and a purely narrow Hβ that appears to be enhanced with respect to the [O III] lines, indicating a very strong starburst emission component.

In the optical spectrum of Jones et al. (2009), we have found clear indication of a BLR component both in Hβ and in Hα (FWHM ∼1586 km s^{-1} and FWHM ∼1700 km s^{-1}, respectively), in agreement with the results of Schulz et al. (1999). The ISAAC MR NIR spectrum of NGC 1365 shows evidence of a broad Pa β component having an FWHM = 1972 km s^{-1}. In Fig. A5, the fit with and without the inclusion of this broad Pa β component is shown. The F test gives a probability of 1 × 10^{-89} that the improvement of the fit is due to statistical fluctuations. We attribute this component to the BLR emission. The He I line was observed with ISAAC in LR mode and has been fitted by a single large component having an FWHM = 1243 km s^{-1} (1166 km s^{-1} if the instrumental resolution is subtracted). However, as the line is placed at the lower wavelength limit of the spectrum and it is not fully covered, we preferred not to include its best-fitting measurements in the data set of the (secure) BLR detections (see Table 7). Finally, using line ratio diagnostic diagrams (see Section 4.1), we found some indication of a starburst component beside the AGN emission, in agreement with Trippe et al. (2010).

NGC 2992

NGC 2992 is a nearby Sa galaxy, highly inclined to our line of sight (about 70°), showing a broad disturbed lane of dust in the equatorial plane. It is an interacting system, linked to NGC 2993 by a tidal tail with a projected length of 2.9 arcmin. Such an interaction could have induced a starburst activity (Glass 1997). It is optically classified as Seyfert 1.9 (Veron et al. 1980), but its classification type has been observed to vary conspicuously in the past, leading to classifications ranging from Seyfert 2 to Seyfert 1.9 on the basis of a broad Hα with no corresponding Hβ component in its nuclear spectrum (Ward et al. 1980), suggesting the existence of an obscured BLR. This was also confirmed later in the infrared by the detection of a broad component (FWHM ∼ 2900 km s^{-1}) in the Pa β (Goodrich, Veilleux & Hill 1994; Veilleux et al. 1997). Gilli et al. (2000) correlated the presence (or the absence) of the broad component of Hα with the nuclear X-ray flux, suggesting that the observed optical variations were due to different phases of rebuilding of the central accretion disc (see also Trippe et al. 2008). The X-ray flux and spectrum were observed to vary along 16 yr of observations. These spectral variations were interpreted as evidence for radiation reprocessed by the molecular, obscuring torus and as an indication of a re-emergence of the AGN nuclear emission. (Gilli et al. 2000).

The optical spectrum of Jones et al. (2009) shows a broad component in Hα, having FWHM = 3153 km s^{-1}, and a purely narrow Hβ. The ISAAC MR spectrum of NGC 2992 shows intense [Fe II] 12 570 Å and Pa β lines with evidence of a strong broad Pa β component having FWHM = 2056 km s^{-1}. We therefore attribute it to the BLR emission. In order to properly reproduce the line profiles, it was necessary to include (likewise observed for the [O III] and [N II] optical lines) two intermediate [Fe II] components, tied together both in velocity and FWHM,
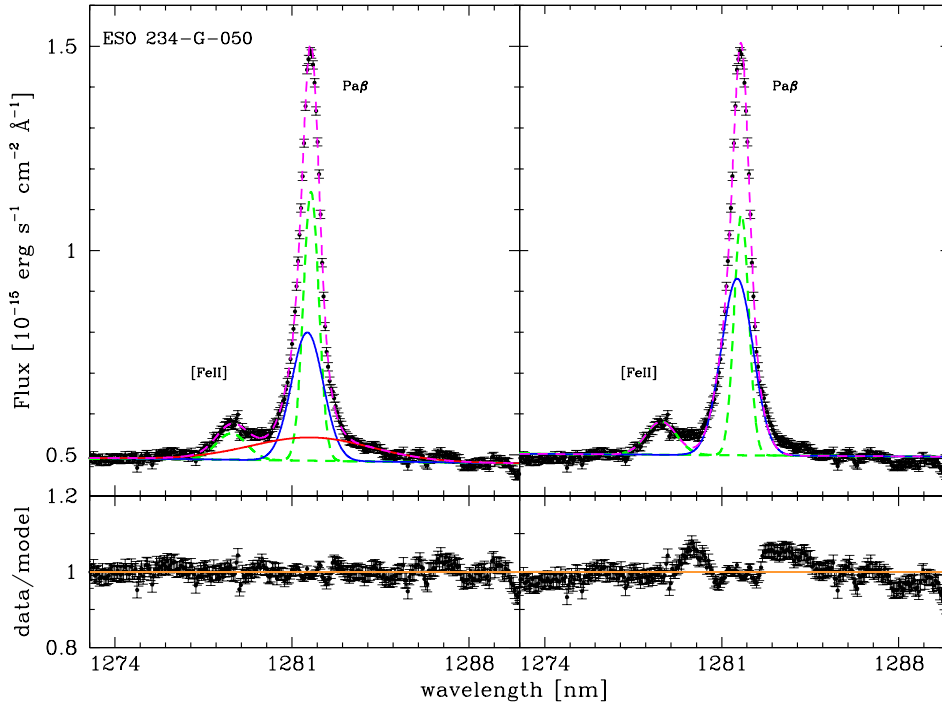
Figure A7. Left: best fit of the Pa β line of ESO 234−G050 including a broad (FWHM = 1305 km s^{-1}) Pa β component. Right: same as before without including the broad Pa β component. Lower panels show the data to model ratio.

having a velocity offset of 111 km s^{-1} with respect to the narrow component. Some other [Fe II] lines were also included (see Fig. 15).

2MASX J18305065+0928414

2MASX J18305065+0928414 is a nearby galaxy, classified as a Seyfert 2 on the basis of the detection of pure narrow Hα and Hβ in the optical spectra by Masetti et al. (2010).

The X-shooter NIR spectrum of 2MASX J18305065+0928414 shows a faint He I with the signature of a broad component which falls near a telluric absorption band (see Fig. 16). Moreover there is no evidence of the [Fe II] 12 570 Å and Pa β emission lines. The He I broad component has an FWHM of 3513 km s^{-1} while the narrow component is associated with the FWHM = 216 km s^{-1} component found in the optical [N II] lines. In Fig. A6, the fit with and without the inclusion of this broad He I component is shown. The F test gives a probability of 1×10^{-121} that the improvement of the fit is due to statistical fluctuations. In the Hα region of the optical spectrum, beside the standard NLR components, there is a very broad component having an FWHM of 6194 km s^{-1} and blueshifted by 1103 km s^{-1} with respect to the narrow component. However, in order to properly fit the spectrum, it is necessary to include also a broad Hα component having FWHM = 2660 km s^{-1}, with the same centre of the NLR component, which we attribute to the BLR. The F test gives a probability of 6×10^{-8} that the improvement of the fit obtained including this last BLR Hα line is due to statistical fluctuations.

ESO 234−G050

ESO 234−G050 is a blue compact dwarf (BCD) elliptical galaxy hosting a Seyfert 2 nucleus (Aguero 1993). No detection of broad components in the permitted lines was reported so far. In our optical X-shooter spectra we have found no evidence for broad components

in the Hβ, while a faint broad Hα having FWHM $\sim$ 970 km s^{-1} has been detected.

The Pa β has been fitted by three components: the NLR component having FHWM = 167 km s^{-1}, an intermediate component having FWHM = 343 km s^{-1} and blueshifted by 35 km s^{-1} with respect to the NLR (similarly as observed in the optical band) and a BLR component having FWHM = 1305 km s^{-1}, with the same centre of the NLR component. In Fig. A7, the fit with and without the inclusion of the broad Pa β component is shown. The F test gives a probability of 1×10^{-60} that the improvement of the fit is due to statistical fluctuations. We therefore attribute it to the BLR emission. Finally, using line ratio diagnostic diagrams (see Section 4.1), we found some indication of a starburst component beside the AGN emission.

NGC 6221

NGC 6221 is a nearby, spiral galaxy classified as SBc(s) by de Vaucouleurs et al. (1991). The bar is clearly visible in the optical and in the infrared and lies at a PA of 118° with a length of $\sim$6 kpc. NGC 6221 forms an apparent physical pair with the spiral galaxy NGC 6215, which is $\sim$110 kpc distant, and is also possibly interacting with two nearby galaxies (Koribalski & Dickey 2004). While its optical spectrum resembles that of a typical reddened ($A_v = 3$) starburst galaxy (Storchi-Bergmann, Kinney & Challis 1995), in the X-ray band NGC 6221 shows a typical type 2 AGN spectrum, variable on time-scales of days and years, with a 2–10 keV intrinsic luminosity of $L_{2-10} = 6.6 \times 10^{41}$ erg s^{-1} (Levenson et al. 2001, Bianchi et al. in preparation). The presence of a sign of non-stellar activity in the optical band (the [O III] shows a component broader and blueshifted with respect to the Hβ) and the early detection of NGC 6221 as an X-ray source (Marshall et al. 1979), motivated Veron, Veron & Zuiderwijk (1981) to propose a composite Seyfert 2/starburst classification for this object.
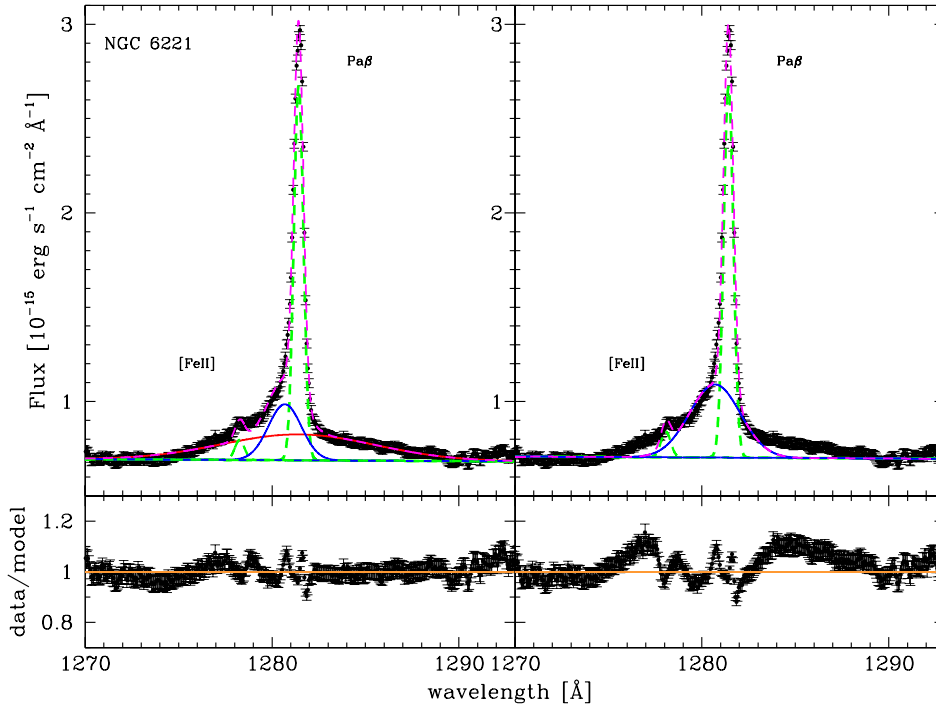
Figure A8. Left: best fit of the Pa β line of NGC 6221 including a broad (FWHM = 2257 km s^{-1}) component. Right: same as before without including a broad Pa β component. Lower panels show the data to model ratio.

No indications of broad (FWHM > 1000 km s^{-1}) permitted emission lines were found both in the optical and in the NIR (see Levenson et al. 2001 and reference within). The optical X-shooter spectrum of NGC 6221 is quite complex. Beside the NLR components both in the Hβ and Hα regions, three intermediate components having a blueshift in the range 20–380 km s^{-1} have been fitted (see Fig. 18). It was also necessary to add a BLR Hα component having FWHM = 1630 km s^{-1}. The F test gives a probability of 1×10^{-256} that the improvement of the fit is due to statistical fluctuations. Beside the presence of the NLR and one intermediate component (FWHM = 483 km s^{-1}) blueshifted by 176 km s^{-1}, the Pa β line has been fitted with a BLR component having FWHM = 2257 km s^{-1}. In Fig. A8, the fit with and without the inclusion of the broad Pa β component is shown. The F test gives a probability of 1×10^{-118} that the improvement of the fit is due to statistical fluctuations (see La Franca et al. 2016, for a more detailed discussion). Moreover, using line ratio diagnostic diagrams (see Section 4.1), we confirm the presence of a starburst component beside the AGN emission.

NGC 7314

NGC 7314 is a barred spiral galaxy (SABb) hosting a Seyfert 1.9 active nucleus (Zoghbi et al. 2013), confirmed by the detection of

a broad Hα in the *HST* spectrum. Moreover, a clear evidence was found for a broad Hα in the polarized flux (Lumsden et al. 2004). The X-ray behaviour of the source is extreme, with a strong variability on all observed time-scales and it is thought to be a type 2 counterpart to the NLS1 class (Dewangan & Griffiths 2005). Furthermore, X-ray observations (from *ASCA*, *Chandra* and *XMM*) revealed a broad component in the Fe K α at 6.4 keV. Interestingly, the line response to the rapid variations of the continuum is different for the narrow and the broad components, suggesting different origins of the corresponding gas (Ebrero et al. 2011).

The best fit of the most relevant emission lines of NGC 7314 are shown in Fig. 19. In the X-shooter optical spectrum, beside the narrow and broad components of Hβ and Hα (FWHM = 1097 km s^{-1} and FWHM = 1330 km s^{-1}, respectively) evidence was found of intermediate components. In particular, in the Hβ+[O III] region two intermediate components with a blueshift of 47 and 67 km s^{-1}, respectively, were found. In the Hα+[N II] region, one intermediate component with a blueshift of 63 km s^{-1} was found. In the NIR spectrum, beside the presence of the narrow component and one intermediate component having a blueshift of 42 km s^{-1}, the Pa β line clearly shows a BLR component having FWHM = 1348 km s^{-1}.

APPENDIX B: BEST FITS FIGURES OF THE AGN2 WITHOUT SECURE EVIDENCE OF BLR COMPONENTS
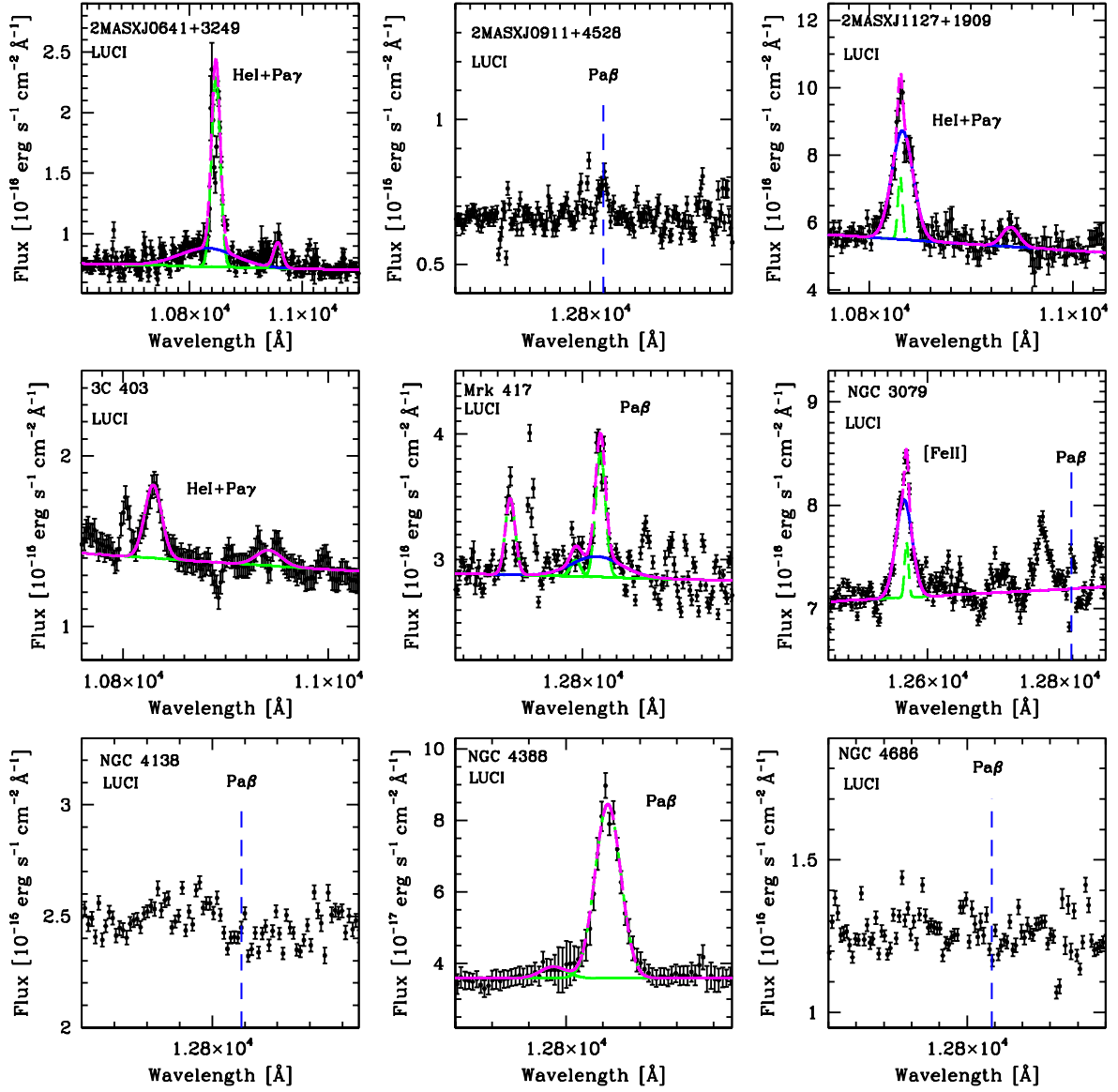
Figure B1. Lines fit of LUCI 'non-broad' AGN2.
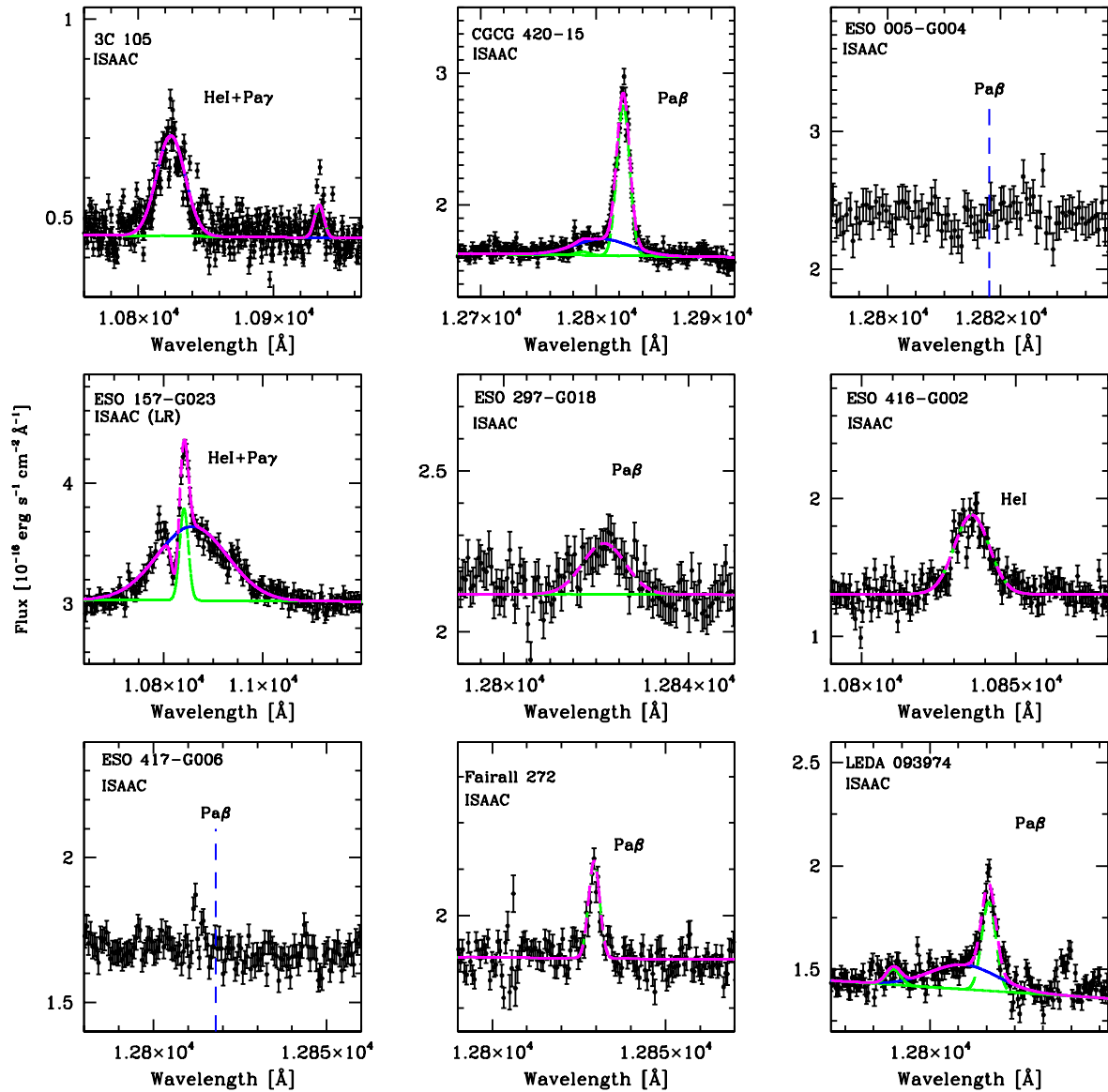
Figure B2. Lines fit of ISAAC 'non-broad' AGN2.
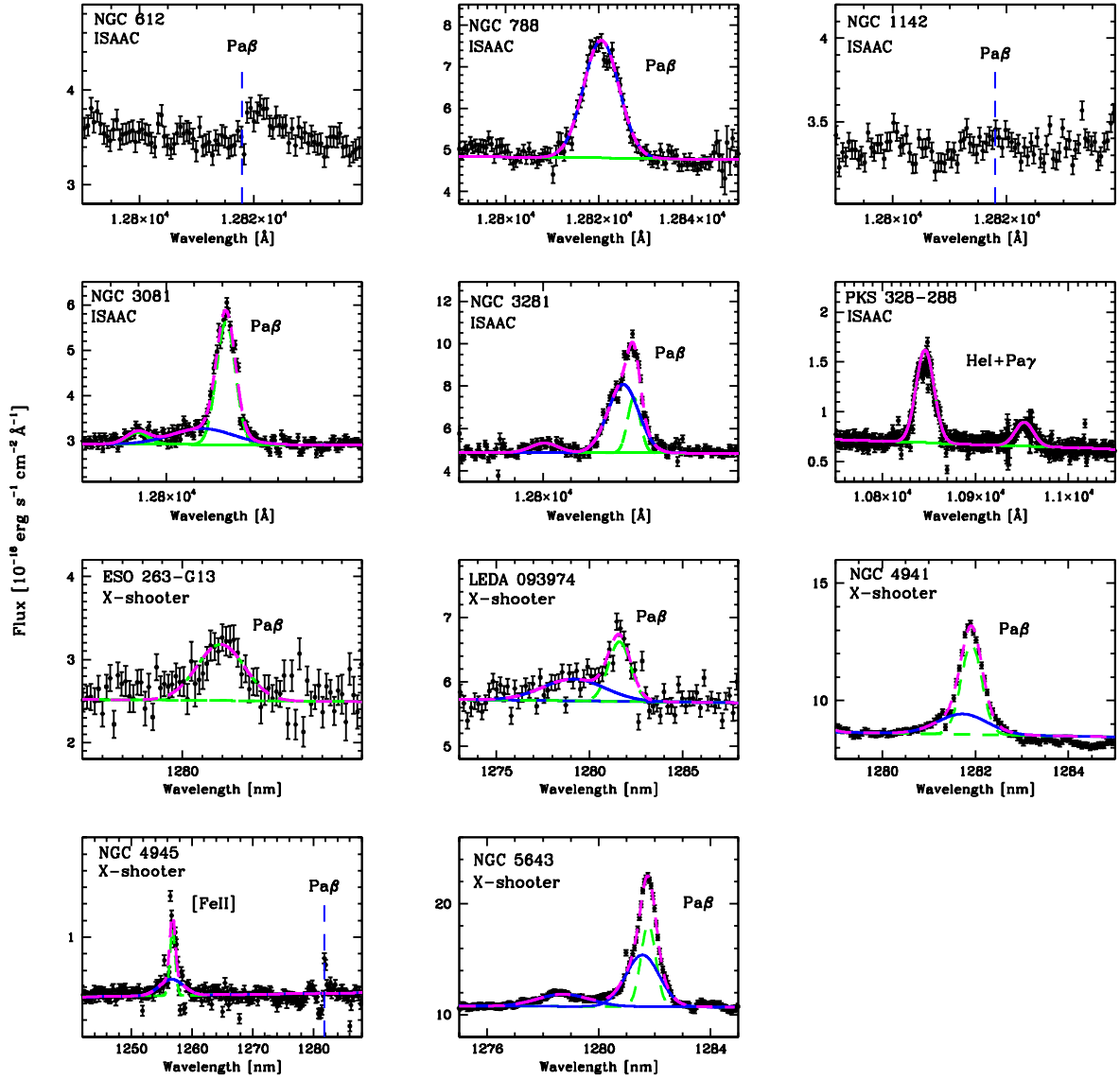
Figure B3. Lines fit of ISAAC and X-shooter 'non-broad' AGN2.

APPENDIX C: BEST FITS VALUES OF THE OPTICAL AND NIR EMISSION LINES OF THE WHOLE SAMPLE

Table C1. FWHM measurements of the emission lines in LUCI spectra.

Object (1)	Redshift (2)	Cl (3)	S/N (4)	Comp. (5)	[S III] λ9069 Å (6)	[S III] λ9531 Å (7)	Pa ε (8)	[C I] λ9853 Å (9)	[S VIII] λ9911 Å (10)	Pa δ (11)	He II λ10 122 Å (12)	He I λ10 830 Å (13)	Pa γ (14)	[P II] λ11 886 Å (15)	[S IX] λ12 523 Å (16)	[Fe II] λ12 570 Å (17)	Pa β (18)
2MASX J06411806+3249313[a]	0.048	2	21	N	475^{+86}_{-52}	475^{+86}_{-52}	475^{+86}_{-52}	–	–	–	–	475^{+86}_{-52}	475^{+86}_{-52}	–	–	–	–
				I								3080^{+695}_{-414}					
2MASX J09112999+4528060	0.0269	2	30	N	–	271^{+16}_{-15}	181^{+65}_{-48}	–	–	–	–	–	–	–	–	–	–
2MASX J11271632+1909198	0.1057	1.8	18	N	511^{+15}_{-27}	511^{+15}_{-27}	–	–	–	–	–	511^{+15}_{-27}	511^{+15}_{-27}	–	–	–	–
3C 403	0.0589	2	20	N	–	510^{+57}_{-51}	–	–	–	–	–	510^{+57}_{-51}	–	–	–	–	–
				I									732^{+362}_{-277}				
Mrk 417	0.0327	2	26	N	–	370^{+8}_{-15}	370^{+8}_{-15}	–	399^{+150}_{-114}	399^{+109}_{-84}	–	370^{+8}_{-15}	370^{+8}_{-15}	–	370^{+8}_{-15}	370^{+8}_{-15}	370^{+8}_{-15}
				B								921^{+270}_{-174}[b]					
NGC 3079	0.0036	2	52	N	–	554^{+50}_{-44}	–	467^{+44}_{-42}	–	–	–	–	–	–	–	167^{-26}_{+30}	–
				I		–		1434^{+82}_{-60}	–	–	–	–	–	–	–	690^{+30}_{-30}	–
NGC 4138	–	1.9	33	N	–	–	–	–	–	–	–	–	–	–	–	–	–
NGC 4388	0.0089	2	44	N	–	487^{+6}_{-6}	487^{+6}_{-6}	–	318^{+58}_{-48}	363^{+17}_{-16}	363^{+17}_{-16}	363^{+17}_{-16}	363^{+17}_{-16}	464^{+102}_{-77}	363^{+17}_{-16}	363^{+17}_{-16}	363^{+17}_{-16}
				I					–			956^{+69}_{-61}[c]	568^{+152}_{-131}	–			
NGC 4395	0.0014	2	33	N	–	389^{+7}_{-6}	389^{+7}_{-6}	251^{+130}_{-78}	363^{+138}_{-88}	211^{+6}_{-6}	211^{+6}_{-6}	348^{+5}_{-6}	348^{+5}_{-6}	172^{+87}_{-60}	–	235^{+7}_{-6}	235^{+7}_{-6}
				B		–		–	–	975^{+76}_{-72}	589^{+263}_{-140}	1350^{+93}_{-70}	1591^{+310}_{-245}	–	–	–	879^{+29}_{-34}
NGC 4686	–	XB	25	N	–	–	–	–	–	–	–	–	–	–	–	–	–

Notes. (1) Source name; (2) Redshift as reported in Table 6; (3) SWIFT70M optical spectral classification; (4) S/N near the Pa β; (5) line components; N: NLR, B: BLR, I: intermediate (see Section 4 for the classification criteria); (6) to (18) FWHM (km s⁻¹) not deconvolved for instrumental resolution.
[a] The intermediate component shows a $\Delta v = 423$ km s⁻¹
[b] This component is centred on its narrow component, but it is on the edge of telluric absorption, thus we did not include it in the 'broad' AGN2 sample.
[c] This broad component, although well centred with the systemic redshift frame, was not included among the BLR detections as the Pa β emission line is not detected.

Table C2. EW measurements of the emission lines in LUCI spectra.

Object	Redshift	Cl	S/N	Comp.	[S III] λ9069 Å	[S III] λ9531 Å	Paε	[C I] λ9853 Å	[S VIII] λ9911 Å	Paδ	He II λ10122 Å	He I λ10830 Å	Pa γ	[P II] λ11886 Å	[S IX] λ12523 Å	[Fe II] λ12570 Å	Pa β
(1)	(2)	(3)	(4)	(5)	(6)	(7)	(8)	(9)	(10)	(11)	(12)	(13)	(14)	(15)	(16)	(17)	(18)
2MASX J06411806+3249313	0.048	2	21	N	11.0	34.5	9.5	–	–	–	–	40.0	5.6	–	–	–	–
				I	–	–	–	–	–	–	–	25.1	–	–	–	–	–
2MASX J09112999+4528060	0.0269	2	30	N	–	9.6	1.4	–	–	–	–	–	–	–	–	–	–
2MASX J11271632+1909198	0.1057	1.8	18	N	7.3	24.6	–	–	–	–	–	18.0	2.5	–	–	–	–
3C 403	0.0589	2	20	N	–	11.0	–	–	–	–	–	6.4	–	–	–	–	–
				I	–	–	–	–	–	–	–	–	2.0	–	–	–	–
Mrk 417	0.0327	2	26	N	–	22.5	5.2	–	1.7	1.6	–	4.4	3.7	–	2.7	1.3	6.1
				B	–	–	–	–	–	–	–	27.2	–	–	–	–	–
NGC 3079	0.0036	2	52	N	–	2.4	–	1.1	–	–	–	F	–	–	–	0.56	–
				I	–	–	–	3.5	–	–	–	–	–	–	–	4.1	–
NGC 4138	–	1.9	33	N	–	–	–	–	–	–	–	–	–	–	–	–	–
NGC 4388	0.0089	2	44	N	–	127.2	20.8	F	2.4	4.9	8.8	19.04	8.11	5.6	4.1	10.5	23.3
				I	–	–	–	–	–	–	–	62.08	3.05	–	–	–	–
NGC 4395	0.0014	2	33	N	–	79.0	10.9	1.0	1.9	3.8	3.7	104.1	16.1	2.0	–	13.2	16.9
				B	–	–	–	–	–	12.9	4.8	58.7	16.3	–	–	–	40.9
NGC 4686	–	XB	25	N	–	–	–	–	–	–	–	–	–	–	–	–	–

Notes. (1) Source name; (2) Redshift as reported in Table 6; (3) SWIFT70M optical spectral classification; (4) S/N near the Pa β; (5) line components; N: NLR, B: BLR, I: intermediate (see Section 4 for the classification criteria); (6)–(18) EW in Å.

Table C3. Flux measurements of the emission lines in LUCI spectra.

Object	Redshift	Cl	S/N	Comp.	[S III] λ9069 Å	[S III] λ9531 Å	Paε	[C I] λ9853 Å	[S VIII] λ9911 Å	Paδ	He II λ10122 Å	He I λ10830 Å	Pa γ	[P II] λ11886 Å	[S IX] λ12523 Å	[Fe II] λ12570 Å	Pa β
(1)	(2)	(3)	(4)	(5)	(6)	(7)	(8)	(9)	(10)	(11)	(12)	(13)	(14)	(15)	(16)	(17)	(18)
2MASX J06411806+3249313	0.048	2	21	N	0.9E-15	2.5E-15	0.7E-15	–	–	–	–	2.8E-15	0.4E-15	–	–	–	–
				I	–	–	–	–	–	–	–	1.7E-15	–	–	–	–	–
2MASX J09112999+4528060	0.0269	2	30	N	–	5.6E-15	0.8E-15	–	–	–	–	–	–	–	–	–	–
2MASX J11271632+1909198	0.1057	1.8	18	N	3.6E-15	11.7E-15	–	–	–	–	–	8.9E-15	1.2E-15	–	–	–	–
3C 403	0.0589	2	20	N	–	13.2E-15	–	–	–	–	–	8.5E-15	–	–	–	–	–
				I	–	–	–	–	–	–	–	–	2.6E-15	–	–	–	–
Mrk 417	0.0327	2	26	N	–	6.8E-15	1.6E-15	–	0.6E-15	0.5E-15	–	13.8E-15	1.1E-15	–	0.8E-15	0.4E-15	1.2E-15
				B	–	–	–	–	–	–	–	8.5E-15	–	–	–	–	–
NGC 3079	0.0036	2	52	N	–	1.2E-15	–	0.6E-15	–	–	–	F	–	–	–	0.4E-15	–
				I	–	–	–	1.2E-15	–	–	–	–	–	–	–	2.9E-15	–
NGC 4138	–	1.9	33	N	–	–	–	–	–	–	–	–	–	–	–	–	–
NGC 4388	0.0089	2	44	N	–	3.3E-15	0.5E-15	–	0.07E-15	0.1E-15	0.3E-15	0.6E-15	0.3E-15	0.2E-15	0.1E-15	0.4E-15	0.8E-15
				I	–	–	–	–	–	–	–	2.0E-15	0.1E-15	–	–	–	–
NGC 4395	0.0014	2	33	N	–	4.5E-13	6.1E-14	6.0E-15	1.2E-14	23.8E-15	23.4E-15	70.2E-14	10.9E-14	13.8E-15	–	95.1E-15	12.0E-14
				B	–	–	–	–	–	80.7E-15	30.4E-15	39.6E-14	11.0E-14	–	–	–	29.0E-14
NGC 4686	–	XB	25	N	–	–	–	–	–	–	–	–	–	–	–	–	–

Notes. (1) Source name; (2) Redshift as reported in Table 6; (3) SWIFT70M optical spectral classification; (4) S/N near the Pa β; (5) line components; N: NLR, B: BLR, I: intermediate (see Section 4 for the classification criteria); (6)–(18) emission line flux in erg s^{-1} cm^{-2}.

Table C4. FWHM measurements of the emission lines in ISAAC spectra.

Object	Redshift	Cl	S/N LR/MR	Comp.	He I λ10 830 Å	Pa γ	O II λ11 287 Å	[P II] λ11 886 Å	[S IX] λ12 523 Å	[Fe II] λ12 570 Å	Pa β
(1)	(2)	(3)	(4)	(5)	(6)	(7)	(8)	(9)	(10)	(11)	(12)
2MASX J05054575−2351139	0.035	2	30/24	N	507^{+49}_{-40}	507^{+49}_{-40}	–	–	–	–	145^{+30}_{-26}
				I	–	–	–	–	–	413^{+40}_{-38}	405^{+67}_{-49}
				B	1823^{+419}_{-318}	–	–	–	–	–	–
3C 105	0.0884	2	27/13	N	–	200^{+112}_{-72}	–	–	–	–	–
				I	627^{+55}_{-54}	–	–	–	–	–	–
CGCG 420−015[a]	0.029	2	64/ 31	N	456^{+14}_{-12}	–	–	–	634^{+350}_{-284}	296^{+10}_{-10}	296^{+10}_{-10}
				I	1331^{+272}_{-134}	–	–	–	–	–	1317^{+177}_{-186}
ESO 005−G004	0.006	2	48/20	N	–	–	–	–	225^{+39}_{-49}	–	–
ESO 157−G023[b]	0.044	2	47/37	N	545^{+85}_{-75}	–	–	–	–	–	–
				I	4043^{+293}_{-273}	–	–	–	–	–	–
ESO 297−G018	0.0253	2	47/38	N	–	–	–	–	–	249^{+43}_{-39}	249^{+43}_{-39}
				I	929^{+77}_{-78} [c]	–	–	–	–	–	–
ESO 374−G044	0.0284	2	45/18	N	632^{+29}_{-36}	632^{+29}_{-36}	–	763^{+474}_{-347}	429^{+153}_{-64}	–	450^{+27}_{-42}
				I	–	–	–	–	–	652^{+74}_{-56}	–
				B	1202^{+383}_{-221}	–	–	–	–	–	1413^{+318}_{-294}
ESO 416−G002	0.059	1.9	45/17	N	347^{+34}_{-30}	–	–	–	–	–	–
ESO 417−G006	0.0163	2	60/42	N	–	–	–	–	–	376^{+45}_{-40}	–
				B	–	–	–	–	–	–	–
Fairall 272	0.022	2	60/34	N	793^{+52}_{-101}	–	–	–	–	422^{+15}_{-30}	86^{+15}_{-10}
LEDA 093974	0.0239	2	59/35	N	555^{+45}_{-42}	–	–	–	555^{+45}_{-42}	453^{+12}_{-12}	134^{+20}_{-21}
				I	1058^{+135}_{-124}	–	–	1153^{+492}_{-375}	–	–	639^{+104}_{-90}
MCG−01−24−012	0.0197	2	50/18	N	616^{+28}_{-27}	616^{+28}_{-27}	–	–	–	381^{+78}_{-117}	245^{+17}_{-16}
				I	1325^{+347}_{-251}	1325^{+347}_{-251}	–	–	–	857^{+121}_{-273}	1325^{+347}_{-251}
MCG−05−23−016	0.0084	2	123/45	N	–	–	–	–	409^{+134}_{-110}	–	247^{+19}_{-18}
				B	1223^{+90}_{-80}	1451^{+134}_{-149}	–	–	–	–	1165^{+27}_{-18}
				I	3855^{+172}_{-158}	–	–	–	–	–	3695^{+335}_{-196}
Mrk 1210	0.014	2	90/ 24	N	564^{+8}_{-8}	–	–	–	–	414^{+18}_{-18}	414^{+18}_{-18}
				I	–	791^{+122}_{-116}	–	670^{+382}_{-237}	760^{+71}_{-56}	902^{+114}_{-61}	902^{+114}_{-61}
				B	1374^{+73}_{-32}	–	–	–	–	–	1937^{+118}_{-225}
NGC 612	–	2	55/29	N	–	–	–	–	–	–	–
NGC 788	0.0135	2	69/ 39	N	556^{+16}_{-15}	467^{+153}_{-61}	–	–	–	213^{+8}_{-7}	213^{+8}_{-7}
NGC 1052	0.0047	2	67/48	N	792^{+61}_{-51}	–	–	–	–	693^{+20}_{-20}	–
				B	2455^{+143}_{-128}	–	–	–	–	–	–
NGC 1142	0.0294	2	61/57	N	–	–	–	–	–	553^{+49}_{-43}	–
				I	934^{+159}_{-119}	–	–	–	–	–	–
NGC 1365	0.005	1.8	88/35	N	–	–	–	–	–	–	787^{+8}_{-8}
				B	1243^{+100}_{-92}	1363^{+67}_{-54}	945^{+38}_{-75}	–	–	–	1972^{+85}_{-75}
NGC 2992	0.0077	2	63/43	N	528^{+56}_{-58}	528^{+56}_{-58}	–	–	–	254^{+3}_{-8}	254^{+3}_{-8}
				I	–	–	–	–	–	869^{+34}_{-56}	869^{+34}_{-56}
				B	3186^{+586}_{-400}	2989^{+660}_{-488}	–	–	–	–	2056^{+29}_{-30}
NGC 3081	0.0077	2	39/28	N	546^{+19}_{-18}	472^{+212}_{-138}	–	–	507^{+295}_{-177}	268^{+17}_{-16}	183^{+7}_{-7}
				I	–	–	–	–	–	–	598^{+70}_{-62}
NGC 3281	0.0113	2	39/26	N	538^{+33}_{-31}	534^{+349}_{-180}	–	–	118^{+23}_{-21}	217^{+24}_{-23}	123^{+10}_{-8}
				I	–	–	–	–	271^{+78}_{-90}	–	300^{+5}_{-5}
PKS 0326−288	0.1096	1.9	18/17	N	565^{+53}_{-34}	568^{+59}_{-51}	–	–	–	–	–

Notes. (1) Source name; (2) Redshift as reported in Table 6; (3) SWIFT70M optical spectral classification; (4) S/N near the Pa β; (5) line components; N: NLR, B: BLR, I: intermediate (see Section 4 for the classification criteria); (6)–(12) FWHM (km s^{-1}) not deconvolved for instrumental resolution.
[a]Intermediate components of FWHM ~ 1100 km s^{-1} were found also in the [O III] lines in the 6dF optical spectra.
[b]Since we have found no signs of Pa β and no optical spectra to validate our measurement of this He I wide component, we decided to not include it in the broad lines AGN2 sample.
[c]This broad component was not conservatively included among the BLR detections as its narrow component was not resolved and no other broad components are observed in the NIR spectrum.

Table C5. EW measurements of the emission lines in ISAAC spectra.

Object	Redshift	Cl	S/N LR/MR	Comp.	He I λ10 830 Å	Pa γ	O II λ11 287 Å	[P II] λ11 886 Å	[S IX] λ12 523 Å	[Fe II] λ12 570 Å	Pa β
(1)	(2)	(3)	(4)	(5)	(6)	(7)	(8)	(9)	(10)	(11)	(12)
2MASX J05054575−2351139	0.035	2	30/24	N	20.5	5.1	–	–	–	–	2.0
				I	–	–	–	–	–	4.8	4.8
				B	16.7	–	–	–	–	–	–
3C 105	0.0884	2	27/13	N	–	1.6	–	–	–	–	–
				I	14.7	–	–	–	–	–	–
CGCG 420−015	0.029	2	64/ 31	N	75.1	–	–	–	5.4	3.1	9.4
				I	18.6	–	–	–	–	–	2.28
ESO 005−G004	0.006	2	48/20	N	–	–	–	–	–	1.5	–
ESO 157−G023	0.044	2	47/37	N	5.5	–	–	–	–	–	–
				I	35.7	–	–	–	–	–	–
ESO 297−G018	0.0253	2	47/38	N	–	–	–	–	–	0.78	0.87
				I	8.1	–	–	–	–	–	–
ESO 374−G044	0.0284	2	45/18	N	48.9	7.0	–	1.9	3.2	–	12.2
				I	–	–	–	–	–	10.2	–
ESO 416−G002	0.059	1.9	45/17	N	6.2	–	–	–	–	–	–
ESO 417−G006	0.0163	2	60/42	N	–	–	–	–	–	6.2	–
Fairall 272	0.022	2	60/34	N	8.2	–	–	–	2.6	3.5	0.9
				B	–	–	–	3.3	–	–	–
MCG−01−24−012	0.0197	2	50/18	N	31.9	4.0	–	–	–	8.3	7.7
				I	7.9	2.2	–	–	–	3.1	1.5
				B	–	–	–	–	–	–	8.9
MCG−05−23−016	0.0084	2	123/45	N	–	–	–	–	1.3	–	3.1
				B	29.8	19.5	–	–	–	–	27.4
				I	84.7	–	–	–	–	–	46.1
Mrk 1210	0.014	2	90/ 24	N	141.4	–	–	–	–	15.1	19.5
				I	–	22.0	–	6.5	11.1	21.1	26.7
				B	258.0	–	–	–	–	–	21.1
NGC 612	–	2	55/29	N	–	–	–	–	–	–	–
NGC 788	0.0135	2	69/ 39	N	26.3	2.6	–	–	–	1.7	5.7
NGC 1052	0.0047	2	67/48	N	10.4	–	–	–	–	9.5	–
				B	40.9	–	–	–	–	–	–
NGC 1142	0.0294	2	61/57	N	–	–	–	–	–	1.6	–
				I	6.1	–	–	–	–	–	–
NGC 1365	0.005	1.8	88/35	N	–	–	–	–	–	–	15.7
				B	21.3	19.3	12.4	–	–	–	15.4
NGC 2992	0.0077	2	63/43	N	22.8	3.4	–	–	–	7.7	5.4
				I	–	–	–	–	–	5.4	2.1
				B	50.9	21.2	–	–	–	–	22.2
NGC 3081	0.0077	2	39/28	N	44.7	5.1	–	–	4.3	3.4	7.8
				I	–	–	–	–	–	–	3.3
NGC 3281	0.0113	2	39/26	N	24.4	4.8	–	–	1.1	2.0	3.0
				I	–	–	–	–	1.2	–	9.2
PKS 0326−288	0.1096	1.9	18/17	N	32.6	9.0	–	–	–	–	–

Notes. (1) Source name; (2) Redshift as reported in Table 6; (3) SWIFT70M optical spectral classification; (4) S/N near the Pa β; (5) line components; N: NLR, B: BLR, I: intermediate (see Section 4 for the classification criteria); (6)–(12) EW (Å).

Table C6. Flux measurements of the emission lines in ISAAC spectra.

Object (1)	Redshift (2)	Cl (3)	S/N LR/MR (4)	Comp. (5)	He I λ10 830 Å (6)	Pa γ (7)	O II λ11 287 Å (8)	[P II] λ11 886 Å (9)	[S IX] λ12 523 Å (10)	[Fe II] λ12 570 Å (11)	Pa β (12)
2MASX J05054575−2351139	0.035	2	30/24	N	7.9E-15	1.2E-15	–	–	–	–	0.2E-15
				I	–	–	–	–	–	0.5E-15	0.4E-15
				B	6.5E-15	–	–	–	–	–	–
3C 105	0.0884	2	27/13	N	–	0.7E-16	–	–	–	–	–
				I	0.6E-15	–	–	–	–	–	–
CGCG 420−015	0.029	2	64/ 31	N	21.0E-15	–	–	–	1.4E-15	0.5E-15	1.5E-15
				I	5.2E-15	–	–	–	–	–	0.4E-15
ESO 005−G004	0.006	2	48/20	N	–	–	–	–	–	0.4E-15	–
ESO 157−G023	0.044	2	47/37	N	1.6E-15	–	–	–	–	–	–
				I	10.3E-15	–	–	–	–	–	–
ESO 297−G018	0.0253	2	47/38	N	–	–	–	–	–	0.2E-15	0.2E-15
				I	1.6E-15	–	–	–	–	–	–
ESO 374−G044	0.0284	2	45/18	N	11.9E-15	7.0	–	0.4E-15	0.6E-15	–	1.8E-15
				I	–	–	–	–	–	1.6E-15	–
				B	4.0E-15	–	–	–	–	–	0.6E-15
ESO 416−G002	0.059	1.9	45/17	N	7.7E-15	–	–	–	–	–	–
ESO 417−G006	0.0163	2	60/42	N	–	–	–	–	–	10.1E-15	–
Fairall 272	0.022	2	60/34	N	2.1E-15	–	–	–	0.7E-15	0.6E-15	0.2E-15
				B	–	–	–	0.9E-15	–	–	–
MCG−01−24−012	0.0197	2	50/18	N	10.5E-15	1.3E-15	–	–	–	1.3E-15	1.2E-15
				I	2.6E-15	0.7E-15	–	–	–	0.5E-15	0.2E-15
				B	–	–	–	–	–	–	1.4E-15
MCG−05−23−016	0.0084	2	123/45	N	–	–	–	–	2.5E-15	–	5.5E-15
				B	59.1E-15	38.2E-15	–	–	–	–	48.8E-15
				I	168.0E-15	–	–	–	–	–	82.2E-15
Mrk 1210	0.014	2	90/ 24	N	78.2E-15	–	–	–	–	4.0E-15	49.0E-15
				I	–	11.4E-15	–	2.9E-15	5.2E-15	5.5E-15	6.7E-15
				B	142.8E-15	–	–	–	–	–	5.3E-15
NGC 612	–	2	55/29	N	–	–	–	–	–	–	–
NGC 788	0.0135	2	69/ 39	N	14.2E-15	1.3E-15	–	–	–	0.9E-15	2.7E-15
NGC 1052	0.0047	2	67/48	N	16.6E-15	–	–	–	–	8.5E-15	–
				B	65.1E-15	–	–	–	–	–	–
NGC 1142	0.0294	2	61/57	N	–	–	–	–	–	0.5E-15	–
				I	2.0E-15	–	–	–	–	–	–
NGC 1365	0.005	1.8	88/35	N	–	–	–	–	–	–	71.5E-15
				B	99.6E-15	90.3E-15	59.4E-15	–	–	–	70.1E-15
NGC 2992	0.0077	2	63/43	N	23.8E-15	3.4E-15	–	–	–	8.6E-15	6.4E-15
				I	–	–	–	–	–	6.0E-15	2.5E-15
				B	53.2E-15	21.5E-15	–	–	–	–	26.3E-15
NGC 3081	0.0077	2	39/28	N	18.1E-15	2.0E-15	–	–	2.8E-15	0.9E-15	2.3E-15
				I	–	–	–	–	–	–	0.9E-15
NGC 3281	0.0113	2	39/26	N	9.2E-15	1.7E-15	–	–	0.6E-15	1.0E-15	1.4E-15
				I	–	–	–	–	0.6E-15	–	4.4E-15
PKS 0326−288	0.1096	1.9	18/17	N	2.0E-15	0.5E-15	–	–	–	–	–

Notes. (1) Source name; (2) Redshift as reported in Table 6; (3) SWIFT70M optical spectral classification; (4) S/N near the Pa β; (5) line components; N: NLR, B: BLR, I: intermediate (see Section 4 for the classification criteria); (6)–(12) emission line flux in erg s^{-1} cm^{-2}.

Table C7. FWHM measurements of the emission lines in X-shooter NIR spectra.

Object (1)	Redshift (2)	CI (3)	S/N (4)	Comp. (5)	[CI] λ9853 Å (6)	[SVIII] λ9911 Å (7)	Paδ (8)	HeII λ10122 Å (9)	HeI λ10830 Å (10)	Paγ (11)	OII λ11287 Å (12)	[PII] λ11886 Å (13)	[SIX] λ12523 Å (14)	[FeII] λ12570 Å (15)	Paβ (16)	[FeII] λ16436 Å (17)
ESO 263−G013	0.0334	2	14	N	–	–	–	511^{+288}_{-154}	–	–	–	–	636^{+77}_{-68}	636^{+77}_{-68}	636^{+77}_{-68}	543^{+41}_{-34}
				I	–	–	–	–	–	–	–	1161^{+463}_{-498}	–	–	–	–
LEDA 093974	0.0239	2	57	N	500^{+100}_{-56}	–	–	356^{+128}_{-111}	319^{+17}_{-20}	–	–	–	319^{+17}_{-20}	319^{+17}_{-20}	319^{+17}_{-20}	319^{+17}_{-20}
				I	–	–	–	1478^{+400}_{-379}	1107^{+114}_{-121}	–	–	–	–	840^{+90}_{-84}	900^{+250}_{-286}	727^{+55}_{-51}
MCG−05−23−016	0.0084	2	26	N	–	–	264^{+55}_{-43}	264^{+55}_{-43}	233^{+15}_{-15}	233^{+15}_{-15}	–	–	560^{+80}_{-77}	560^{+80}_{-77}	560^{+80}_{-77}	–
				B	–	–	3468^{+580}_{-470}	–	2474^{+67}_{-64}	1911^{+105}_{-79}	–	–	–	–	2134^{+93}_{-89}	–
2MASX J18305065+0928414	0.0193	2	37	N	–	–	–	–	216^{+12}_{-9}	–	–	–	–	–	–	–
				B	–	–	–	–	3513^{+232}_{-213}	–	–	–	–	–	–	–
ESO 234−G050	0.0088	2	40	N	–	–	124^{+12}_{-11}	–	122^{+12}_{-11}	122^{+12}_{-11}	–	–	–	122^{+12}_{-11}	167^{+11}_{-13}	124^{+12}_{-11}
				I	–	–	267^{+36}_{-31}	–	434^{+9}_{-9}	272^{+26}_{-24}	–	–	–	490^{+26}_{-23}	343^{+63}_{-57}	498^{+26}_{-23}
				B	–	–	–	–	1111^{+63}_{-59}	–	–	–	–	–	1305^{+381}_{-322}	–
NGC 4941	0.0038	2	50	N	–	–	123^{+20}_{-14}	123^{+20}_{-14}	123^{+20}_{-14}	123^{+20}_{-14}	–	123^{+20}_{-14}	123^{+20}_{-14}	123^{+20}_{-14}	123^{+20}_{-14}	–
				I	–	–	–	–	308^{+8}_{-8}	246^{+32}_{-30}	–	–	–	–	292^{+24}_{-18}	–
				I	–	–	–	571^{+40}_{-46}	664^{+33}_{-31}	–	–	430^{+142}_{-103}	–	479^{+38}_{-26}	–	–
NGC 4945	0.0017	2	22	N	–	–	–	–	249^{+30}_{-40}	–	–	–	–	249^{+30}_{-40}	–	249^{+30}_{-40}
				I	–	–	–	–	998^{+216}_{-172}	–	–	1268^{+280}_{-272}	–	1098^{+243}_{-146}	–	1098^{+243}_{-146}
NGC 5643	0.0040	2	37	N	–	–	146^{+21}_{-24}	146^{+21}_{-24}	146^{+21}_{-24}	146^{+21}_{-24}	–	251^{+31}_{-27}	146^{+21}_{-24}	146^{+21}_{-24}	146^{+21}_{-24}	146^{+21}_{-24}
				I	–	–	330^{+10}_{-10}	560^{+65}_{-59}	289^{+2}_{-5}	330^{+10}_{-10}	–	–	–	376^{+42}_{-36}	330^{+10}_{-10}	376^{+42}_{-36}
				I	–	–	–	–	884^{+80}_{-84}	–	–	–	–	–	–	–
NGC 6221	0.0045	2	39	N	–	–	141^{+1}_{-1}	–	141^{+1}_{-1}	141^{+1}_{-1}	–	239^{+31}_{-27}	138^{+16}_{-18}	141^{+1}_{-1}	141^{+1}_{-1}	141^{+1}_{-1}
				I	–	–	238^{+80}_{-28}	–	343^{+9}_{-9}	343^{+9}_{-9}	–	–	–	483^{+12}_{-12}	483^{+12}_{-12}	481^{+12}_{-8}
				B	–	–	–	–	2142^{+110}_{-141}	–	–	–	–	–	2257^{+99}_{-93}	–
NGC 7314	0.0047	1.9	37	N	–	–	84^{+2}_{-2}	84^{+2}_{-2}	84^{+2}_{-2}	84^{+2}_{-2}	–	132^{+23}_{-18}	78^{+10}_{-10}	84^{+2}_{-2}	84^{+2}_{-2}	143^{+16}_{-14}
				I	–	–	–	289^{+60}_{-44}	361^{+10}_{-9}	361^{+10}_{-9}	–	–	262^{+74}_{-40}	392^{+13}_{-13}	361^{+10}_{-9}	–
				B	–	–	1137^{+94}_{-82}	–	1428^{+46}_{-38}	1430^{+78}_{-99}	–	–	–	–	1348^{+15}_{-15}	–
NGC 3783	0.0097	1	24	N	–	307^{+53}_{-43}	307^{+53}_{-43}	307^{+53}_{-43}	307^{+53}_{-43}	307^{+53}_{-43}	–	–	696^{+203}_{-150}	307^{+53}_{-43}	307^{+53}_{-43}	–
				I	–	–	–	–	1446^{+98}_{-88}	–	–	–	–	–	–	–
				B	–	–	3268^{+318}_{-373}	2212^{+617}_{-490}	5114^{+205}_{-182}	3927^{+252}_{-223}	–	–	–	–	3500^{+99}_{-103}	–

Notes. (1) Source name; (2) Redshift as reported in Table 6; (3) SWIFT70M optical spectral classification; (4) S/N near the Pa β; (5) line components; N: NLR, B: BLR, I: intermediate (see Section 4 for the classification criteria); (6)–(17) FWHM (km s^{-1}) not deconvolved for instrumental resolution.

Table C8. EW measurements of the emission lines in X-shooter NIR spectra.

Object	Redshift	Cl	S/N	Comp.	[C I] λ9853 Å	[S VIII] λ9911 Å	Pa δ	He II λ10122 Å	He I λ10830 Å	Pa γ	O II λ11287 Å	[P II] λ11886 Å	[S IX] λ12523 Å	[Fe II] λ12570 Å	Pa β	[Fe II] λ16436 Å
(1)	(2)	(3)	(4)	(5)	(6)	(7)	(8)	(9)	(10)	(11)	(12)	(13)	(14)	(15)	(16)	(17)
ESO 263−G013	0.0334	2	14	N	–	–	–	3.3	–	–	–	–	2.9	10.5	8.1	10.7
				B	–	–	–	–	–	–	–	–	–	–	–	–
LEDA 093974	0.0239	2	57	N	3.7	–	–	1.1	7.5	–	–	5.0	2.7	8.6	2.4	9.3
				I	–	–	–	2.9	12.7	–	–	–	–	9.1	2.3	5.9
MCG−05−23−016	0.0084	2	26	N	–	–	1.4	1.6	8.2	1.2	–	–	1.7	0.4	10.3	–
				B	–	–	25.0	–	84.8	31.3	–	–	–	–	54.9	–
2MASX J18305065+0928414	0.0193	2	37	N	–	–	–	–	1.3	–	–	–	–	–	–	–
				B	–	–	–	–	18.6	–	–	–	–	–	–	–
ESO 234−G050	0.0088	2	40	N	–	–	0.8	–	14.8	3.8	–	–	–	–	10.4	–
				I	–	–	2.4	1.3	36.6	13.9	–	–	–	3.9	10.2	3.5
				B	–	–	–	–	13.9	–	–	–	–	14.8	7.1	19.7
NGC 4941	0.0038	2	50	N	–	–	0.7	0.9	4.6	0.8	–	0.6	1.0	0.9	2.5	–
				I	–	–	–	–	13.6	0.9	–	–	–	6.0	1.4	–
				I	–	–	–	3.1	0.9	–	–	0.7	–	–	–	–
NGC 4945	0.0017	2	22	N	–	–	–	–	4.7	–	–	–	–	6.7	F	6.3
				I	–	–	–	–	8.0	–	–	6.1	–	7.4	–	3.7
NGC 5643	0.0040	2	37	N	–	–	–	0.4	8.4	–	–	–	–	–	–	–
				I	–	–	0.9	3.2	24.7	1.9	–	1.8	–	1.9	4.6	2.8
				I	–	–	1.0	–	7.1	1.8	–	–	–	5.7	6.6	6.4
				I	–	–	–	–	–	–	–	–	–	–	–	–
NGC 6221	0.0045	2	39	N	–	–	4.0	–	10.7	8.6	–	2.8	1.4	5.9	18.6	6.1
				I	–	–	1.1	–	21.7	2.0	–	–	–	10.3	9.5	12.6
				B	–	–	–	–	29.6	9.2	–	–	–	–	20.5	–
NGC 7314	0.0047	1.9	37	N	–	–	1.9	–	11.7	3.3	–	1.5	1.4	1.4	6.4	2.6
				I	–	–	–	2.3	41.0	5.6	–	–	2.2	1.4	13.0	–
				B	–	–	24.1	5.0	114.0	50.9	–	–	–	–	74.9	–
NGC 3783	0.0097	1	24	N	–	3.1	2.1	1.5	38.7	1.9	–	–	4.4	2.9	4.2	–
				I	–	–	–	–	39.1	–	–	–	–	–	–	–
				B	–	–	28.3	9.7	143.4	45.5	–	–	–	–	113.8	–

Notes. (1) Source name; (2) Redshift as reported in Table 6; (3) SWIFT70M optical spectral classification; (4) S/N near the Pa β; (5) line components; N: NLR, B: BLR, I: intermediate (see Section 4 for the classification criteria); (6)–(17) EW (Å).

Table C9. Flux measurements of the emission lines in X-shooter NIR spectra.

Object	Redshift	CI	S/N	Comp.	[C I] λ9853 Å	[S VIII] λ9911 Å	Paδ	He II λ10122 Å	He I λ10830 Å	Pa γ	O II λ11287 Å	[P II] λ11886 Å	[S IX] λ12523 Å	[Fe II] λ12570 Å	Pa β	[Fe II] λ16436 Å
(1)	(2)	(3)	(4)	(5)	(6)	(7)	(8)	(9)	(10)	(11)	(12)	(13)	(14)	(15)	(16)	(17)
ESO 263−G013	0.0334	2	14	N	–	–	–	0.95E-16	–	–	–	–	0.72E-16	0.3E-15	0.3E-15	0.2E-15
				B	–	–	–	–	–	–	–	1.3E-15	–	–	–	–
LEDA 093974	0.0239	2	57	N	0.2E-15	–	–	0.6E-16	0.4E-15	–	–	–	0.2E-15	0.5E-15	0.1E-15	0.5E-15
				I	–	–	–	0.2E-15	0.7E-15	–	–	–	–	0.5E-15	0.1E-15	0.3E-15
MCG−05−23−016	0.0084	2	26	N	–	–	0.4E-15	0.4E-15	2.4E-15	0.3E-15	–	–	0.5E-15	0.1E-15	3.1E-15	–
				B	–	–	6.9E-15	–	24.7E-14	9.1E-15	–	–	–	–	16.7E-15	–
2MASX J18305065+0928414	0.0193	2	37	N	–	–	–	–	0.5E-16	–	–	–	–	–	–	–
				B	–	–	–	–	0.8E-15	–	–	–	–	–	–	–
ESO 234−G050	0.0088	2	40	N	–	–	0.5E-16	–	0.9E-15	0.2E-15	–	–	–	0.2E-15	0.5E-15	0.1E-15
				I	–	–	0.2E-15	0.8E-16	2.1E-15	0.8E-15	–	–	–	0.7E-15	0.5E-15	0.7E-15
				B	–	–	–	–	0.8E-15	–	–	–	–	–	0.4E-15	–
NGC 4941	0.0038	2	50	N	–	–	0.6E-16	0.8E-16	0.4E-15	0.7E-16	–	0.5E-16	0.8E-16	0.7E-16	0.2E-15	–
				I	–	–	–	–	1.2E-15	0.8E-16	–	–	–	–	0.1E-15	–
NGC 4945	0.0017	2	22	N	–	–	–	–	0.8E-16	–	–	0.6E-16	–	0.5E-15	–	0.3E-16
				I	–	–	–	–	0.3E-16	–	–	–	–	0.4E-16	–	0.2E-16
				I	–	–	–	0.3E-15	0.5E-16	–	–	0.4E-16	–	0.5E-16	–	0.3E-15
NGC 5643	0.0040	2	37	N	–	–	0.9E-16	0.5E-16	0.9E-15	0.2E-15	–	0.2E-15	–	0.2E-15	0.5E-15	0.3E-15
				I	–	–	1.0E-16	0.3E-15	2.6E-15	0.2E-15	–	–	–	0.6E-15	0.7E-15	0.6E-15
				I	–	–	–	–	0.7E-15	–	–	–	–	–	–	–
NGC 6221	0.0045	2	39	N	–	–	0.3E-15	–	0.7E-15	0.6E-15	–	0.2E-15	0.1E-16	0.4E-15	1.3E-15	0.4E-15
				I	–	–	0.8E-16	–	1.5E-15	0.1E-15	–	–	–	0.7E-15	0.7E-15	0.8E-16
				B	–	–	–	–	2.0E-15	0.6E-15	–	–	–	–	1.4E-15	–
NGC 7314	0.0047	1.9	37	N	–	–	0.5E-16	0.6E-16	0.3E-15	0.9E-16	–	0.4E-16	0.4E-16	0.4E-16	0.2E-15	0.9E-16
				I	–	–	–	0.1E-15	1.1E-15	0.2E-15	–	–	0.7E-16	0.4E-16	0.4E-15	–
				B	–	–	0.7E-15	–	3.1E-15	1.4E-15	–	–	–	–	2.3E-15	–
NGC 3783	0.0097	1	24	N	–	0.7E-15	0.5E-15	0.3E-15	8.0E-15	0.4E-15	–	–	1.0E-15	0.6E-15	1.0E-15	–
				I	–	–	–	–	8.1E-15	–	–	–	–	–	–	–
				B	–	–	6.2E-15	2.1E-15	29.8E-15	9.6E-15	–	–	–	–	26.0E-15	–

Notes. (1) Source name; (2) Redshift as reported in Table 6; (3) SWIFT70M optical spectral classification; (4) S/N near the Pa β; (5) line components; N: NLR, B: BLR, I: intermediate (see Section 4 for the classification criteria); (6)–(17) emission line flux in erg s⁻¹ cm⁻².

Table C10. FWHM measurements of the emission lines in X-shooter VIS spectra.

Object	Redshift	CI	S/N	Comp.	[Fe VII] λ5722 Å	He I λ5877 Å	[Fe VII] λ6088 Å	[O I] λ6302 Å	[O I] λ6366 Å	[N II] λ6550 Å	Hα	[N II] λ6585 Å	[S II] λ6718 Å	[S II] λ6732 Å	[O II] λ7322 Å	[Fe XI] λ7894 Å	[S III] λ9069 Å	[S III] λ9531 Å
(1)	(2)	(3)	(4)	(5)	(6)	(7)	(8)	(9)	(10)	(11)	(12)	(13)	(13)	(14)	(15)	(16)	(17)	(18)
ESO 263−G013	0.0334	2	13	N	—	—	—	—	—	56^{+14}_{-6}	56^{+14}_{-6}	56^{+14}_{-6}	56^{+14}_{-6}	56^{+14}_{-6}	—	—	241^{+103}_{-120}	83^{+9}_{-10}
				I	—	—	—	393^{+38}_{-30}	393^{+38}_{-30}	463^{+8}_{-6}	463^{+8}_{-6}	463^{+8}_{-6}	454^{+29}_{-22}	454^{+29}_{-22}	—	—	—	546^{+54}_{-44}
LEDA 093974	0.0239	2	31	N	—	—	—	190^{+18}_{-9}	190^{+18}_{-9}	190^{+18}_{-9}	190^{+2}_{-2}	190^{+2}_{-2}	197^{+5}_{-3}	197^{+5}_{-3}	208^{+77}_{-57}	—	223^{+5}_{-5}	223^{+5}_{-5}
				I	—	—	—	809^{+45}_{-38}	—	706^{+4}_{-4}	706^{+4}_{-4}	706^{+4}_{-4}	635^{+8}_{-15}	635^{+8}_{-15}	1418^{+59}_{-80}	—	928^{+17}_{-20}	928^{+17}_{-20}
MCG−05−23−016	0.0084	2	30	N	384^{+53}_{-48}	383^{+71}_{-55}	216^{+34}_{-30}	195^{+6}_{-6}	167^{+15}_{-15}	215^{+2}_{-2}	215^{+2}_{-2}	215^{+2}_{-2}	206^{+3}_{-5}	206^{+3}_{-5}	—	—	215^{+9}_{-9}	209^{+4}_{-4}
				B	—	—	—	—	—	—	2232^{+36}_{-38}	—	—	—	—	—	—	—
2MASX J18305065+0928414	0.0193	2	37	N	—	—	—	—	—	216^{+12}_{-9}	216^{+12}_{-9}	216^{+12}_{-9}	216^{+12}_{-9}	216^{+12}_{-9}	—	—	226^{+73}_{-33}	196^{+17}_{-13}
				B	—	—	332^{+43}_{-31}	415^{+118}_{-112}	—	—	2660^{+500}_{-460}	—	—	—	—	—	—	—
				I	—	—	—	—	—	—	6194^{+160}_{-160}	—	—	—	—	—	—	—
ESO 234−G050	0.0088	2	44	N	—	124^{+33}_{-20}	—	175^{+14}_{-19}	175^{+14}_{-19}	117^{+3}_{-4}	113^{+3}_{-4}	113^{+3}_{-4}	117^{+3}_{-2}	117^{+3}_{-2}	288^{+18}_{-14}	—	137^{+16}_{-26}	137^{+16}_{-26}
				I	—	486^{+79}_{-67}	—	498^{+17}_{-44}	498^{+17}_{-44}	327^{+7}_{-10}	327^{+7}_{-10}	327^{+7}_{-10}	366^{+3}_{-6}	366^{+3}_{-6}	—	—	391^{+52}_{-26}	391^{+52}_{-26}
				B	—	—	—	—	—	—	972^{+124}_{-104}	—	—	—	—	—	—	—
NGC 4941	0.0038	2	24	N	—	288^{+51}_{-36}	201^{+68}_{-42}	107^{+11}_{-10}	186^{+29}_{-19}	103^{+2}_{-1}	103^{+2}_{-1}	103^{+2}_{-1}	103^{+2}_{-1}	103^{+2}_{-1}	231^{+29}_{-22}	—	106^{+10}_{-9}	122^{+5}_{-5}
				I	—	—	—	373^{+23}_{-34}	—	370^{+4}_{-2}	370^{+4}_{-2}	370^{+4}_{-2}	373^{+3}_{-4}	373^{+3}_{-4}	—	—	359^{+17}_{-14}	372^{+5}_{-9}
NGC 4945	0.002	2	9	N	—	—	—	126^{+23}_{-20}	—	230^{+5}_{-6}	230^{+5}_{-6}	230^{+5}_{-6}	165^{+22}_{-12}	165^{+22}_{-12}	—	—	279^{+31}_{-29}	234^{+11}_{-12}
				I	—	442^{+34}_{-22}	558^{+66}_{-114}	583^{+70}_{-56}	—	794^{+18}_{-14}	794^{+18}_{-14}	794^{+18}_{-14}	527^{+27}_{-23}	527^{+27}_{-23}	—	—	—	—
NGC 5643	0.0040	2	25	N	—	—	—	147^{+13}_{-8}	147^{+13}_{-8}	98^{+2}_{-2}	98^{+2}_{-2}	98^{+2}_{-2}	126^{+3}_{-6}	126^{+3}_{-6}	—	—	204^{+5}_{-4}	109^{+1}_{-1}
				I	402^{+48}_{-42}	342^{+19}_{-17}	—	402^{+11}_{-11}	402^{+11}_{-11}	273^{+2}_{-2}	273^{+2}_{-2}	273^{+2}_{-2}	472^{+34}_{-60}	472^{+34}_{-60}	310^{+14}_{-12}	—	600^{+5}_{-4}	346^{+1}_{-1}
				I	—	—	—	—	—	401^{+3}_{-3}	401^{+3}_{-3}	401^{+2}_{-3}	306^{+8}_{-10}	306^{+8}_{-10}	—	—	—	—
				I	—	—	—	—	—	249^{+23}_{-11}	—	249^{+23}_{-11}	—	—	—	—	—	—
NGC 6221	0.0045	2	44	N	386^{+61}_{-54}	142^{+13}_{-9}	200^{+55}_{-28}	134^{+13}_{-10}	147^{+40}_{-25}	90^{+4}_{-3}	90^{+4}_{-3}	90^{+4}_{-3}	90^{+4}_{-3}	90^{+4}_{-3}	125^{+31}_{-13}	—	241^{+103}_{-120}	83^{+9}_{-10}
				I	—	—	—	456^{+17}_{-23}	519^{+102}_{-108}	192^{+8}_{-16}	192^{+8}_{-16}	192^{+8}_{-16}	192^{+8}_{-16}	192^{+8}_{-16}	—	—	—	—
				I	—	—	—	—	—	500^{+12}_{-7}	500^{+12}_{-7}	500^{+12}_{-7}	500^{+12}_{-7}	500^{+12}_{-7}	765^{+90}_{-50}	—	—	546^{+54}_{-44}
				I	—	—	—	—	—	77^{+16}_{-8}	77^{+16}_{-8}	77^{+16}_{-8}	77^{+16}_{-8}	77^{+16}_{-8}	—	—	—	—
				B	—	—	—	—	—	—	1630^{+12}_{-11}	—	—	—	—	—	—	—
NGC 7314	0.0047	1.9	45	N	191^{+11}_{-10}	130^{+8}_{-8}	246^{+8}_{-8}	70^{+2}_{-4}	62^{+2}_{-4}	89^{+1}_{-1}	89^{+1}_{-1}	89^{+1}_{-1}	87^{+1}_{-1}	87^{+1}_{-1}	94^{+8}_{-11}	—	86^{+1}_{-2}	90^{+1}_{-1}
				I	—	—	—	180^{+5}_{-5}	180^{+5}_{-5}	187^{+2}_{-2}	270^{+2}_{-2}	187^{+2}_{-2}	179^{+4}_{-4}	190^{+3}_{-3}	236^{+19}_{-16}	—	219^{+2}_{-2}	207^{+2}_{-2}
				B	—	1561^{+50}_{-59}	—	—	—	—	1330^{+5}_{-4}	—	—	—	—	—	—	—
NGC 3783	0.0097	1	53	N	—	524^{+45}_{-30}	575^{+17}_{-17}	153^{+7}_{-7}	158^{+22}_{-13}	212^{+2}_{-2}	212^{+2}_{-2}	212^{+2}_{-2}	212^{+4}_{-2}	212^{+4}_{-2}	316^{+17}_{-13}	—	128^{+23}_{-18}	164^{+6}_{-4}
				I	830^{+28}_{-23}	—	1796^{+146}_{-125}	566^{+40}_{-43}	757^{+44}_{-54}	1167^{+9}_{-11}	1167^{+9}_{-11}	1167^{+9}_{-11}	—	—	—	746^{+56}_{-52}	369^{+8}_{-17}	456^{+14}_{-12}
				B	—	8533^{+124}_{-115}	—	—	—	—	5290^{+24}_{-23}	—	—	—	—	—	—	—

Notes. (1) Source name; (2) Redshift as reported in Table 6; (3) SWIFT70M optical spectral classification; (4) S/N near the Hα; (5) line components; N: NLR, B: BLR, I: intermediate (see Section 4 for the classification criteria); (6)–(18) FWHM (km s^{-1}) not deconvolved for instrumental resolution.

Table C11. EW measurements of the emission lines in X-shooter VIS spectra.

Object	Redshift	Cl	S/N	Comp.	[Fe VII] λ5721 Å	He I λ5876 Å	[Fe VII] λ6087 Å	[O I] λ6300 Å	[O I] λ6363 Å	[N II] λ6548 Å	Hα	[N II] λ6583 Å	[S II] λ6716 Å	[S II] λ6731 Å	[O II] λ7323.0 Å	[Fe XI] λ7892 Å	[S III] λ9069 Å	[S III] λ9531 Å
(1)	(2)	(3)	(4)	(5)	(6)	(7)	(8)	(9)	(10)	(11)	(12)	(13)	(13)	(14)	(15)	(16)	(17)	(18)
ESO 263−G013	0.0334	2	14	N	–	–	–	–	–	2.1	4.7	6.4	2.0	1.6	–	–	13.0	12.1
				I	–	–	–	12.6	4.9	23.3	52.5	70.1	19.7	21.4	–	–	–	34.6
LEDA 093974	0.0239	2	57	N	–	–	–	2.0	0.8	5.0	8.9	15.4	5.5	4.1	0.3	–	3.3	9.6
				I	–	–	–	4.3	–	11.2	14.5	34.1	8.9	10.7	3.5	–	9.5	13.6
MCG−05−23−016	0.0084	2	26	N	1.3	1.3	1.1	3.7	0.9	5.4	19.4	16.0	4.3	4.6	–	–	3.2	7.5
				B	–	–	–	–	–	–	34.2	–	–	–	–	–	–	–
2MASX J18305065+0928414	0.0193	2	37	N	–	–	–	2.3	–	2.6	3.3	7.8	1.6	2.0	–	–	1.7	4.0
				B	–	–	–	–	–	–	9.8	–	–	–	–	–	–	–
				I	–	–	–	–	–	–	90.9	–	–	–	–	–	–	–
ESO 234−G050	0.0088	2	40	N	–	1.2	–	5.3	1.7	1.5	29.7	4.5	5.4	4.9	4.7	–	5.5	13.9
				I	–	2.4	–	9.9	3.6	3.8	56.2	11.5	15.3	15.4	–	–	5.7	18.3
				B	–	–	–	–	–	–	20.7	–	–	–	–	–	–	–
NGC 4941	0.0038	2	50	N	–	2.6	1.0	4.2	3.3	4.8	10.4	14.3	4.5	5.3	2.6	–	5.3	16.7
				I	–	–	–	8.6	–	19.4	32.5	57.9	14.9	19.1	–	–	17.1	37.6
NGC 4945	0.0017	2	22	N	–	–	–	2.0	–	11.7	8.8	36.4	4.0	3.1	–	–	1.9	3.5
				I	–	–	–	7.5	–	25.7	21.9	80.1	13.0	12.2	–	–	–	–
NGC 5643	0.0040	2	37	N	–	–	–	3.6	1.1	2.6	6.5	7.7	3.8	4.2	–	–	15.7	11.3
				I	1.4	2.9	1.6	7.6	2.4	14.8	45.6	44.1	5.8	4.1	2.8	–	10.9	48.9
				I	–	–	–	–	–	6.2	15.6	18.6	9.9	1.4	–	–	–	–
				I	–	–	–	–	–	0.6	–	1.9	–	–	–	–	–	–
NGC 6221	0.0045	2	44	N	0.7	2.0	0.5	1.3	0.5	9.9	48.0	29.9	4.4	5.3	2.6	–	13.0	12.0
				I	–	–	–	–	–	8.8	50.9	26.6	5.5	5.3	–	–	–	–
				I	–	1.9	0.6	3.3	1.1	11.3	45.7	33.9	9.1	10.6	4.7	–	–	34.6
				I	–	–	–	–	–	0.4	1.1	1.1	0.3	0.3	–	–	–	–
				B	–	2.3	–	–	–	–	59.0	–	–	–	–	–	–	–
NGC 7314	0.0047	1.9	45	N	4.0	5.3	7.7	9.5	2.5	13.5	45.2	40.6	15.4	13.6	1.3	–	16.0	50.0
				I	–	–	–	6.2	3.8	8.5	66.8	25.5	8.2	11.6	1.6	–	19.4	56.9
				B	–	–	–	–	–	–	223.0	–	–	–	–	–	–	–
NGC 3783	0.0097	1	53	N	–	2.7	7.2	2.7	1.0	5.3	22.0	19.5	5.7	6.2	1.9	–	2.7	11.0
				I	7.5	–	5.1	3.6	4.1	40.1	147.4	78.5	–	–	–	3.4	8.5	19.0
				B	–	57.2	–	–	–	–	446.0	–	–	–	–	–	–	–

Notes. (1) Source name; (2) Redshift as reported in Table 6; (3) SWIFT70M optical spectral classification; (4) S/N near the Hα; (5) line components; N: NLR, B: BLR, I: intermediate (see Section 4 for the classification criteria); (6)−(18) EW (Å).

Table C12. Line flux measurements of the emission lines in X-shooter VIS spectra.

Object (1)	Redshift (2)	Cl (3)	S/N (4)	Comp. (5)	[Fe VII] λ5721 Å (6)	He I λ5876 Å (7)	[Fe VII] λ6087 Å (8)	[O I] λ6300 Å (9)	[O I] λ6363 Å (10)	[N II] λ6548 Å (11)	Hα (12)	[N II] λ6583 Å (13)	[S II] λ6716 Å (13)	[S II] λ6731 Å (14)	[O II] λ7323.0 Å (15)	[Fe XI] λ7892 Å (16)	[S III] λ9069 Å (17)	[S III] λ9531 Å (18)
ESO 263−G013	0.0334	2	14	N	—	—	—	—	—	0.6E-16	1.4E-16	1.9E-16	0.5E-16	0.4E-16	—	—	2.2E-16	2.2E-16
				I	—	—	—	3.7E-16	1.4E-16	7.0E-16	1.5E-15	2.1E-15	5.2E-16	5.7E-16	—	—	—	6.4E-16
LEDA 093974	0.0239	2	57	N	—	—	—	1.2E-16	0.5E-16	3.3E-16	5.8E-16	9.9E-16	3.5E-16	2.6E-16	0.2E-16	—	2.2E-16	6.3E-16
				I	—	—	—	2.7E-16	—	7.3E-16	9.4E-16	2.2E-15	5.7E-16	6.9E-16	2.3E-16	—	6.4E-16	8.9E-16
MCG−05−23−016	0.0084	2	26	N	2.3E-16	2.4E-16	2.0E-16	6.9E-16	1.7E-16	1.1E-15	4.0E-15	3.3E-15	3.3E-15	0.9E-15	0.9E-15	—	7.1E-16	1.7E-15
				B	—	—	—	—	—	—	7.1E-15	—	—	—	—	—	—	—
2MASX J18305065+0928414	0.0193	2	37	N	—	—	—	1.1E-16	—	1.4E-16	1.8E-16	4.2E-16	0.9E-16	1.1E-16	—	—	1.2E-16	2.5E-16
				B	—	—	—	—	—	—	5.3E-16	—	—	—	—	—	—	—
				I	—	—	—	—	—	—	4.9E-15	—	—	—	—	—	—	—
ESO 234−G050	0.0088	2	40	N	—	1.6E-16	—	7.1E-16	2.3E-16	2.1E-16	3.4E-15	6.3E-16	7.4E-16	6.8E-16	6.1E-16	—	5.9E-16	1.3E-15
				I	—	3.2E-16	—	1.3E-15	4.8E-16	5.4E-16	4.2E-15	1.6E-15	2.1E-15	2.1E-15	—	—	6.0E-16	1.7E-15
				B	—	—	—	—	—	—	7.8E-15	—	—	—	—	—	—	—
NGC 4941	0.0038	2	50	N	—	3.5E-16	1.5E-16	6.3E-16	4.9E-16	9.3E-16	2.0E-15	2.8E-15	7.3E-16	8.5E-16	4.4E-16	—	9.3E-16	3.0E-15
				I	—	—	—	1.3E-15	—	3.8E-15	6.3E-15	1.1E-14	2.4E-15	3.1E-15	—	—	3.0E-15	6.8E-15
NGC 4945	0.0017	2	22	N	—	—	—	5.5E-18	—	4.2E-17	3.1E-17	1.3E-16	1.8E-17	1.4E-17	F	—	2.1E-17	4.2E-17
				I	—	—	—	2.1E-17	—	9.2E-17	7.7E-17	2.8E-16	5.7E-17	5.3E-17	—	—	—	—
NGC 5643	0.0040	2	37	N	1.6E-16	3.3E-16	2.1E-16	4.7E-16	1.5E-16	3.9E-16	9.8E-16	1.2E-15	5.8E-16	6.3E-16	4.5E-16	—	2.6E-15	2.0E-15
				I	—	—	—	9.9E-16	3.2E-16	2.2E-15	6.9E-15	6.6E-15	8.7E-16	6.2E-16	—	—	1.9E-15	8.7E-15
				I	—	—	—	—	—	9.4E-16	2.4E-15	2.8E-15	1.5E-15	2.1E-15	—	—	—	—
				I	—	—	—	—	—	9.3E-17	—	2.8E-16	—	—	—	—	—	—
NGC 6221	0.0045	2	44	N	4.0E-17	1.1E-16	2.8E-17	7.5E-17	2.6E-17	6.1E-16	2.9E-15	1.8E-15	2.7E-16	3.2E-16	2.8E-17	—	2.2E-16	2.2E-16
				I	—	—	—	1.9E-16	6.3E-17	5.2E-16	3.1E-15	1.6E-15	3.3E-16	4.0E-16	—	—	—	—
				I	—	1.1E-16	3.4E-17	—	—	7.0E-16	2.8E-15	2.1E-15	5.5E-16	6.5E-16	1.6E-16	—	—	6.4E-16
				I	—	—	—	—	—	2.8E-17	6.9E-17	8.3E-17	1.6E-17	1.8E-17	—	—	—	—
				B	—	—	—	—	—	—	3.6E-15	—	—	—	—	—	—	—
NGC 7314	0.0047	1.9	45	N	2.5E-17	3.4E-17	5.8E-17	9.1E-17	2.4E-17	1.9E-16	6.5E-16	5.8E-16	1.7E-16	1.9E-16	2.0E-17	—	3.3E-16	9.0E-16
				I	—	—	—	5.9E-17	3.6E-17	1.2E-16	9.5E-16	3.6E-16	1.4E-16	1.0E-16	2.4E-17	—	4.0E-16	1.0E-15
				B	—	1.5E-16	—	—	—	—	3.2E-15	—	—	—	—	—	—	—
NGC 3783	0.0097	1	53	N	—	8.9E-16	2.4E-15	9.3E-16	3.4E-16	1.8E-15	7.8E-15	6.8E-15	2.0E-15	2.2E-15	6.1E-16	—	7.1E-16	2.8E-15
				I	2.4E-15	—	1.7E-15	1.2E-15	1.4E-15	1.4E-14	5.2E-14	2.7E-14	—	—	—	1.0E-15	2.2E-15	4.8E-15
				B	—	1.9E-14	—	—	—	—	1.6E-13	—	—	—	—	—	—	—

Notes. (1) Source name; (2) Redshift as reported in Table 6; (3) SWIFT70M optical spectral classification; (4) S/N near the Hα; (5) line components; N: NLR, B: BLR, I: intermediate (see Section 4 for the classification criteria); (6)–(18) emission line flux in erg s^{-1} cm^{-2}.

Table C13. FWHM measurements of the emission lines in X-shooter UVB spectra.

Object (1)	Redshift (2)	CI (3)	S/N (4)	Comp. (5)	[Ne V] λ3346 Å (6)	[Ne V] λ3426 Å (7)	[O II] λ3728 Å (8)	[O II] λ3730 Å (9)	[Fe VII] λ3760 Å (10)	[Ne III] λ3869 Å (11)	[Fe V] λ3893 Å (12)	[Ne III] λ3968 Å (13)	Hγ (13)	He II λ4686 Å (14)	Hβ (15)	[O III] λ4959 Å (16)	[O III] λ5007 Å (17)
ESO 263−G013	0.0334	2	14	N	293^{+61}_{-73}	293^{+61}_{-73}	–	–	–	390^{+25}_{-29}	390^{+25}_{-29}	349^{+53}_{-62}	330^{+117}_{-78}	384^{+203}_{-110}	98^{+2}_{-2}	98^{+2}_{-2}	98^{+2}_{-2}
				I	–	–	508^{+20}_{-17}	–	–	–	–	–	–	–	560^{+274}_{-137}	440^{+19}_{-14}	440^{+19}_{-14}
LEDA 093974	0.0239	2	57	N	–	–	99^{+11}_{-6}	99^{+11}_{-6}	–	149^{+10}_{-10}	–	–	–	–	157^{+2}_{-2}	157^{+2}_{-2}	157^{+2}_{-2}
				I	–	–	596^{+15}_{-18}	596^{+15}_{-18}	–	673^{+59}_{-59}	–	–	–	–	–	732^{+8}_{-8}	732^{+8}_{-8}
MCG−05−23−016	0.0084	2	26	N	255^{+56}_{-48}	246^{+16}_{-4}	210^{+8}_{-12}	210^{+8}_{-12}	–	207^{+7}_{-10}	310^{+97}_{-94}	185^{+28}_{-33}	190^{+28}_{-27}	262^{+47}_{-39}	221^{+4}_{-3}	221^{+4}_{-3}	221^{+4}_{-3}
				I	–	–	–	–	–	–	–	–	–	–	–	–	–
2MASX J18305065+0928414	0.0193	2	37	N	–	–	415^{+124}_{-96}	–	449^{+281}_{-209}	–	–	–	–	–	176^{+7}_{-8}	176^{+7}_{-8}	176^{+7}_{-8}
				I	–	–	–	–	–	–	–	–	–	–	–	663^{+74}_{-75}	663^{+74}_{-75}
ESO 234−G050	0.0088	2	40	N	–	–	132^{+4}_{-2}	132^{+4}_{-2}	–	166^{+12}_{-12}	166^{+12}_{-12}	308^{+35}_{-25}	161^{+12}_{-14}	–	172^{+2}_{-2}	172^{+2}_{-2}	172^{+2}_{-2}
				I	–	–	425^{+13}_{-6}	425^{+13}_{-6}	–	481^{+2}_{-2}	–	–	371^{+59}_{-44}	–	481^{+2}_{-2}	481^{+2}_{-2}	481^{+2}_{-2}
NGC 4941	0.0038	2	50	N	133^{+4}_{-6}	133^{+4}_{-6}	138^{+4}_{-4}	138^{+4}_{-4}	–	129^{+6}_{-6}	129^{+6}_{-6}	169^{+9}_{-15}	195^{+13}_{-6}	241^{+14}_{-9}	109^{+2}_{-2}	109^{+2}_{-2}	109^{+2}_{-2}
				I	549^{+68}_{-56}	549^{+68}_{-56}	386^{+9}_{-6}	386^{+9}_{-6}	–	422^{+16}_{-20}	422^{+16}_{-20}	–	–	–	359^{+10}_{-11}	299^{+7}_{-8}	299^{+7}_{-8}
				I	–	–	–	–	–	–	–	–	–	–	–	691^{+28}_{-62}	691^{+28}_{-62}
NGC 4945	0.0017	2	22	N	–	–	–	–	–	–	–	–	–	–	–	–	–
NGC 5643	0.0040	2	37	N	284^{17}_{-10}	284^{17}_{-10}	187^{+4}_{-7}	187^{+4}_{-7}	158^{+18}_{-18}	245^{+8}_{-4}	–	–	–	–	93^{+5}_{-5}	–	–
				I	–	–	428^{+32}_{-19}	–	–	603^{+24}_{-10}	–	319^{+18}_{-18}	202^{+5}_{-7}	290^{+10}_{-12}	251^{+2}_{-2}	251^{+2}_{-2}	251^{+2}_{-2}
				I	–	1023^{+960}_{-498}	750^{+96}_{-76}	–	–	–	–	–	473^{+46}_{-32}	568^{+81}_{-72}	398^{+41}_{-26}	291^{+5}_{-4}	291^{+5}_{-4}
				I	–	–	–	–	–	–	–	–	–	–	880^{+130}_{-116}	697^{+11}_{-12}	697^{+11}_{-12}
NGC 6221	0.0045	2	50	N	–	–	126^{+2}_{-4}	126^{+2}_{-4}	–	–	125^{+2}_{-6}	–	77^{+2}_{-2}	–	79^{+1}_{-2}	177^{+4}_{-2}	177^{+4}_{-2}
				I	–	–	569^{+10}_{-8}	–	–	–	–	–	144^{+1}_{-2}	–	146^{+1}_{-4}	125^{+5}_{-5}	125^{+5}_{-5}
				I	–	–	551^{+60}_{-53}	–	–	636^{+28}_{-38}	–	–	518^{+19}_{-19}	–	541^{+13}_{-13}	212^{+3}_{-4}	212^{+3}_{-4}
				I	–	–	–	–	–	–	–	–	–	–	–	851^{+16}_{-10}	851^{+16}_{-10}
NGC 7314	0.0047	1.9	11	N	68^{+1}_{-1}	68^{+1}_{-1}	56^{+6}_{-4}	56^{+6}_{-4}	–	56^{+1}_{-1}	75^{+9}_{-4}	91^{+5}_{-6}	67^{+2}_{-2}	78^{+2}_{-7}	56^{+1}_{-1}	56^{+1}_{-1}	56^{+1}_{-1}
				I	178^{+4}_{-3}	178^{+4}_{-3}	121^{+6}_{-5}	121^{+6}_{-5}	–	171^{+4}_{-3}	224^{+28}_{-27}	–	222^{+8}_{-8}	203^{+8}_{-5}	68^{+1}_{-1}	68^{+1}_{-1}	68^{+1}_{-1}
				I	–	–	135^{+6}_{-4}	135^{+6}_{-4}	–	–	–	–	–	–	213^{+1}_{-1}	213^{+1}_{-1}	213^{+1}_{-1}
				B	–	–	–	–	–	–	–	–	–	–	1097^{+57}_{-63}	–	–
NGC 3783	0.0097	1	21	N	133^{+5}_{-6}	133^{+5}_{-6}	146^{+3}_{-2}	146^{+3}_{-2}	–	234^{+7}_{-4}	–	114^{+21}_{-20}	241^{+10}_{-11}	226^{+60}_{-52}	322^{+1}_{-1}	114.0^{+2}_{-2}	114.0^{+2}_{-2}
				I	529^{+7}_{-5}	529^{+7}_{-5}	548^{+17}_{-10}	548^{+17}_{-10}	566^{+30}_{-37}	668^{+7}_{-10}	473^{+20}_{-10}	437^{+17}_{-27}	–	–	–	322^{+1}_{-1}	322^{+1}_{-1}
				I	495^{+82}_{-78}	1556^{+38}_{-38}	–	–	918^{+168}_{-170}	–	–	1216^{+158}_{-107}	1012^{+14}_{-22}	705^{+59}_{-77}	2102^{+14}_{-13}	685^{+2}_{-2}	685^{+2}_{-2}
				B	–	–	–	–	–	–	–	–	5186^{+37}_{-44}	–	5549^{+37}_{-18}	–	–

Notes. (1) Source name; (2) Redshift as reported in Table 6; (3) SWIFT70M optical spectral classification; (4) S/N near the Hβ; (5) line components; N: NLR, B: BLR, I: intermediate (see Section 4 for the classification criteria); (6)–(17) FWHM (km s⁻¹) not deconvolved for instrumental resolution.

Table C14. EW measurements of the emission lines in X-shooter UVB spectra.

Object (1)	Redshift (2)	CI (3)	S/N (4)	Comp. (5)	[Ne V] λ3346 Å (6)	[Ne V] λ3426 Å (7)	[O II] λ3728 Å (8)	[O II] λ3730 Å (9)	[Fe VII] λ3760 Å (10)	[Ne III] λ3869 Å (11)	[Fe V] λ3893 Å (12)	[Ne III] λ3968 Å (13)	Hγ (13)	He II λ4686 Å (14)	Hβ (15)	[O III] λ4959 Å (16)	[O III] λ5007 Å (17)
ESO 263−G013	0.0088	2	14	N	26.6	39.8	–	–	–	51.6	19.7	17.2	9.9	5.3	5.2	22.7	69.0
				I	–	–	111.2	–	–	–	–	–	–	–	9.2	37.9	108.0
LEDA 093974	0.0239	2	57	N	–	–	1.8	2.8	–	3.0	–	–	–	–	1.6	3.9	11.7
				I	–	–	5.9	26.5	–	5.1	–	–	–	–	–	5.7	16.9
MCG−05−23−016	0.0084	2	26	N	6.3	–	13.1	12.9	–	18.1	3.1	2.9	2.0	2.0	3.3	14.1	42.2
				I	–	22.3	–	–	–	–	–	–	–	–	–	–	–
2MASX J18305065+0928414	0.0193	2	37	N	–	–	10.7	–	9.0	–	–	–	–	–	0.8	4.4	13.3
				I	–	–	–	–	–	–	–	–	–	–	–	2.3	7.0
ESO 234−G050	0.0088	2	40	N	–	–	11.5	12.9	–	2.5	2.0	2.0	4.0	–	10.7	8.9	26.8
				I	–	–	29.2	23.1	–	5.5	–	–	3.0	–	10.0	15.4	46.3
NGC 4941	0.0038	2	50	N	3.9	13.2	9.7	6.1	–	14.7	1.4	5.4	3.1	3.6	2.3	11.7	35.3
				I	2.7	10.6	12.1	34.8	–	24.7	5.4	–	–	–	9.0	29.9	90.2
				I	–	–	–	–	–	–	–	–	–	–	–	12.7	38.3
NGC 4945	0.0017	2	22	N	–	–	–	–	–	–	–	–	–	–	1.5	–	–
NGC 5643	0.0040	2	37	N	4.5	15.0	19.9	16.1	1.0	12.5	–	–	4.1	3.7	12.0	47.0	144.6
				I	–	–	27.4	–	–	10.0	–	5.2	2.0	1.3	4.5	7.1	22.3
				I	–	12.7	12.6	–	–	–	–	–	–	–	2.7	12.1	33.7
				I	–	–	–	–	–	–	–	–	–	–	–	–	–
NGC 6221	0.0045	2	50	N	–	–	4.2	3.6	–	–	1.3	–	1.4	–	4.7	2.1	6.4
				I	–	–	10.8	–	–	–	–	–	5.2	–	12.9	0.6	2.0
				I	–	–	1.1	–	–	2.0	–	–	2.5	–	7.8	1.4	4.3
				I	–	–	–	–	–	–	–	–	–	–	–	3.0	9.7
NGC 7314	0.0047	1.9	11	N	6.3	20.0	16.2	23.5	25.4	3.6	–	5.7	8.5	8.2	17.9	83.6	250.4
				I	9.1	29.4	2.4	10.5	31.2	4.7	–	–	13.8	14.7	5.5	23.1	69.1
				I	–	–	1.9	13.4	–	–	–	–	–	–	29.5	120.5	361.0
				B	–	–	–	–	–	–	–	–	–	–	31.2	–	–
NGC 3783	0.0097	1	21	N	0.2	0.5	1.0	1.0	–	3.4	–	0.3	1.8	1.0	7.1	3.4	10.1
				I	1.2	5.0	0.8	1.2	1.7	5.2	1.7	2.7	–	–	–	20.8	63.7
				I	0.3	3.5	–	–	0.9	–	–	11.7	5.8	2.7	27.4	14.9	43.2
				B	–	–	–	–	–	–	–	–	43.6	–	88.9	–	–

Notes. (1) Source name; (2) Redshift as reported in Table 6; (3) SWIFT70M optical spectral classification; (4) S/N near the Hβ; (5) line components; N: NLR, B: BLR, I: intermediate (see Section 4 for the classification criteria); (6)–(17) EW (Å).

Table C15. Line flux measurements of the emission lines in X-shooter UVB spectra.

Object	Redshift	CI	S/N	Comp.	[Ne V] λ3346 Å	[Ne V] λ3426 Å	[O II] λ3728 Å	[O II] λ3730 Å	[Fe VII] λ3760 Å	[Ne III] λ3869 Å	[Fe V] λ3893 Å	[Ne III] λ3968 Å	Hγ	He II λ4686 Å	Hβ	[O III] λ4959 Å	[O III] λ5007 Å
(1)	(2)	(3)	(4)	(5)	(6)	(7)	(8)	(9)	(10)	(11)	(12)	(13)	(13)	(14)	(15)	(16)	(17)
ESO 263−G013	0.0334	2	14	N	0.2E-15	0.3E-15	–	–	–	0.5E-15	0.2E-15	0.2E-15	1.5E-16	0.1E-16	0.8E-16	3.7E-16	1.1E-15
LEDA 093974	0.0239	2	57	N	–	–	–	0.5E-16	–	0.6E-16	–	–	–	–	1.4E-16	6.2E-16	1.7E-15
				I	–	–	1.2E-15	4.7E-16	–	1.0E-16	–	–	–	–	0.8E-16	1.8E-16	5.4E-16
MCG−05−23−016	0.0084	2	26	N	2.5E-16	9.4E-16	6.8E-16	6.6E-16	–	9.6E-16	1.6E-16	1.9E-16	2.2E-16	2.5E-16	4.4E-16	1.9E-15	5.6E-15
				I	–	–	–	–	–	–	–	–	–	–	–	–	–
2MASX J18305065+0928414	0.0193	2	37	N	–	–	0.4E-16	–	–	–	–	–	–	–	–	0.9E-16	2.6E-16
				I	–	–	–	–	0.4E-16	–	–	–	–	–	0.2E-16	0.5E-16	1.4E-16
ESO 234−G050	0.0088	2	40	N	–	–	7.5E-16	8.4E-16	–	1.8E-16	1.4E-16	1.4E-16	3.5E-16	–	8.9E-16	8.1E-16	2.4E-15
				I	–	–	1.9E-15	1.5E-15	–	4.0E-16	–	–	2.6E-16	–	8.4E-16	1.4E-16	4.2E-15
NGC 4941	0.0038	2	50	N	5.9E-17	2.1E-16	3.2E-16	2.0E-16	–	4.6E-16	4.3E-17	2.4E-16	3.1E-16	3.8E-16	2.6E-16	1.4E-16	4.1E-15
				I	4.1E-17	1.7E-16	4.0E-16	1.1E-15	–	7.7E-16	1.7E-16	–	–	–	1.0E-15	3.5E-15	1.0E-14
				I	–	–	–	–	–	–	–	–	–	–	–	1.5E-15	4.5E-15
NGC 4945	0.0017	2	22	N	–	–	–	–	–	–	–	–	–	–	–	–	–
NGC 5643	0.0040	2	37	N	3.5E-17	–	2.9E-16	2.3E-16	2.7E-17	3.6E-16	–	1.9E-16	2.0E-16	2.5E-16	8.5E-17	3.4E-15	1.1E-14
				I	–	9.6E-17	3.9E-16	–	–	2.9E-16	–	–	1.0E-16	8.8E-17	6.9E-16	5.2E-16	1.6E-15
				I	–	–	1.8E-16	–	–	–	–	–	–	–	2.6E-16	8.8E-16	2.5E-15
NGC 6221	0.0045	2	50	N	–	–	1.1E-16	9.5E-17	–	–	4.5E-17	–	5.9E-17	–	2.2E-16	1.1E-16	3.2E-16
				I	–	–	2.9E-16	–	–	–	–	–	2.2E-16	–	6.2E-16	3.2E-17	9.9E-17
				I	–	–	2.9E-17	–	–	7.0E-17	–	–	1.1E-16	–	3.8E-16	7.2E-17	2.1E-16
				I	–	–	–	–	–	–	–	–	–	–	–	1.4E-16	4.8E-16
NGC 7314	0.0047	1.9	11	N	1.7E-17	5.3E-17	5.5E-17	8.0E-17	6.7E-17	9.4E-18	–	1.5E-17	3.2E-17	3.5E-17	7.5E-17	4.0E-16	1.2E-15
				I	2.4E-17	7.8E-17	8.3E-18	3.6E-17	8.2E-17	1.2E-17	–	–	5.1E-17	6.2E-17	2.3E-17	1.1E-16	3.3E-16
				I	–	–	6.4E-18	4.6E-17	–	–	–	–	–	–	1.2E-16	5.8E-16	1.7E-15
				B	–	–	–	–	–	–	–	–	–	–	1.3E-16	–	–
NGC 3783	0.0097	1	21	N	2.0E-16	6.4E-16	8.9E-16	8.9E-16	–	2.6E-15	–	1.7E-16	8.9E-16	5.1E-16	3.4E-15	1.6E-15	4.9E-15
				I	2.2E-15	5.9E-15	7.4E-16	1.2E-15	1.5E-16	4.1E-15	1.3E-15	1.8E-15	–	–	–	1.0E-14	3.1E-14
				I	3.5E-16	4.1E-15	–	–	7.8E-=16	–	–	1.2E-15	2.8E-15	1.5E-15	1.3E-14	7.2E-15	2.1E-14
				B	–	–	–	–	–	–	–	–	2.1E-14	–	4.3E-14	–	–

This paper has been typeset from a TEX/LATEX file prepared by the author.